EXPERIMENTAL DETERMINATION AND THEORETICAL ANALYSIS OF THE ELASTIC SCATTERING OF PROTONS BY BERYLLIUM

Thesis by

Forrest S. Mozer

In Partial Fulfillment of the Requirements
for the Degree of
Doctor of Philosophy

California Institute of Technology
Pasadena, California
1956

ACKNOWLEDGMENTS

The author wishes to express his deepest gratitude to the faculty of the Kellogg Radiation Laboratory for their advice, guidance, and assistance throughout the course of this work. Without the experimental leadership and aid of Professors W. A. Fowler, T. Lauritsen, and C. C. Lauritsen, and without the theoretical discussions and advice of Professor R. F. Christy, this work could never have reached completion.

The author also wishes to acknowledge the aid of Dr. F. S. Buffington of the Metallurgy Department of the California Institute of Technology for his help in polishing targets.

To the Lockheed Aircraft Company who supplied him with a fellowship for the academic year 1955-1956, the author also wishes to record his gratitude.

ABSTRACT

Fifteen angular distributions and three excitation curves for the reaction $Be^9(p, p)$ have been run in the energy region between 200-3000 kev. Measurements of $Be^9(p, d)$ and $Be^9(p, \alpha)$ were made at 333 kev and near 470 kev. This data has been analyzed and fitted in terms of the following states in B^{10}; an s-wave $J = 1^-$ state near 330 kev; a p-wave $J = 2^+$ state near 980 kev; an s-wave $J = 2^-$ state near 998 kev; a p-wave $J = 0^+$ state near 1084 kev; and an s-wave $J = 2^-$ state near 1330 kev.

TABLE OF CONTENTS

PART TITLE PAGE

II EXPERIMENTAL APPARATUS

III EXPERIMENTAL TECHNIQUES

IV THEORETICAL ANALYSIS OF THE ELASTIC SCATTERING DATA

TABLE OF CONTENTS (Cont'd)

I. INTRODUCTION

As part of the general inquiry into the structure of nuclei and the nature of nuclear forces, a vast amount of experimental and theoretical data has been compiled on the energy levels of light nuclei.(1) By analogy to the historic development of modern quantum mechanics from a study of atomic energy levels, such a compilation and cataloging of the properties of nuclear levels might be hoped to yield some orderliness, whose discovery would be a step forward in the understanding of the nucleus. While experimental knowledge of the energy levels of light nuclei is far from complete, indications of certain types of orderliness already exist. Hence, before discussing the experimental and theoretical cataloging of those states in B^{10} with excitation energies between 6.78 and 8.21 mev, it might be worthwhile to review two types of orderliness discovered as a result of an inquiry into the energy levels of light nuclei.

Given an energy level in any light nucleus, it is found in regions where a sufficient amount of experimental data is available, that if corrections are made to the energy of the given level for the Coulomb potential and neutron-proton mass difference, there is a one-to-one correlation between the existence and properties of this given level and a corresponding state in any isobar of the particular nucleus under consideration, if the Pauli exclusion principle does not forbid the formation of the state in the isobar. The existence of such groups of isobaric spin levels (commonly called isotopic spin multiplets) argues strongly in favor of the charge independence of nuclear forces.

A second indication of orderliness in nuclear energy level schemes comes from the work of Lane, Elliott, and Flowers,(2) who are able to deduce theoretically the properties of even parity excited states of p-shell nuclei from the intermediate coupling extension of the single particle nuclear model, a model in which each nucleon moves in an average potential caused by the net effects of all neighboring nucleons.

What are the properties of an excited state that such a theory or a good experiment should disclose? The most obvious properties are the existence of the level and its excitation energy. Other properties are its total angular momentum, parity, total width or half life, partial widths or probabilities for various modes of decay, relative orbital angular momentum of the particles forming the state or into which the state decays, and isotopic spin. The analysis of the variation with energy and scattering angle of the cross-section for some particular reaction that forms the state of interest in the compound or final nucleus is expected to yield information about some or all of the properties listed above.

When Be^9 is bombarded by protons of energies between 200 and 1800 kev, the compound nucleus B^{10} is formed in a region of excitation from 6.78 to 8.21 mev. (See fig. 1, the energy level diagram of the states of B^{10}). From previous work, five energy levels, correponding to incident protons of energies 330, 490, 670, 995, and 1085 kev, have been postulated in this energy region.

A brief resume of the information available on the properties of these states at the time the present experiments were undertaken will serve to justify the further investigation reported in this paper.

In the energy region under discussion, the compound nucleus B^{10} can break up in any of the five following ways:

$$B^{10*} \longrightarrow Be^9 + p$$
$$B^{10*} \longrightarrow B^{10} + \gamma$$
$$B^{10*} \longrightarrow Li^6 + \alpha$$
$$B^{10*} \longrightarrow Li^{6*} + \alpha$$
$$B^{10*} \longrightarrow Be^8 + d$$

For incident protons near 330 kev, all of the above reaction products except the alpha groups leaving Li^6 in an excited state had been more or less studied, and anomalies in the cross-sections corresponding to the 6.89 mev state in B^{10} had been reported. The existence of alpha and deuteron groups labeled this level as an isotopic spin zero state, since Be^8, d, α, and Li^6 all have isotopic spins zero. Because of the relatively great width of the state, ($\Gamma = 175$ kev which makes $\gamma^2 > 30\%$ of the single particle limit) and because the angular distribution of the capture gamma rays was found to be isotropic, the formation of the state was attributed to s-wave protons. Since the ground state of Be^9 has spin 3/2, odd parity, and the proton has spin $\frac{1}{2}$, even parity, s-wave protons can form states in B^{10} of odd parity with total angular momentum of 1 or 2. The relative intensities of capture gamma rays to the ground, 0.72, 1.74, and 2.15 mev states of B^{10} were more consistent with a spin 1 assignment. However, this assignment was not without difficulties, the primary one being that the gamma ray transitions to the 0.72 and 2.15 mev states were then electric dipole between two isotopic spin zero states. Such a transition is highly forbidden by isotopic spin selection rules.(3) The extent of its presence in this particular case indicated an isotopic spin impurity of 0.4, the largest impurity of any known state in light nuclei.

The total cross-section for $Be^9(p,d)$ was found to exhibit a peak near 470 kev, indicating the possibility of a resonance level in B^{10} at 7.01 mev. A corresponding peak in $Be^9(p,\gamma)$ had been both confirmed and denied by various investigators. Since the $Be^9(p,p)$ and $Be^9(p,\alpha)$ reactions showed little or no anomaly in this region, the question of the existence of a level near 490 kev was unanswered.

The status of the 667 kev level was very similar to that of the 490 kev state. Small anomalies were reported at this energy in the reactions $Be^9(p,\alpha)$, $Be^9(p,d)$, and $Be^9(p,\gamma)$. No analysis of this data had been attempted.

The resonance at 997 kev showed itself in the production of elastic protons, deuterons, gamma rays, and alpha particles to the ground state of Li^6. The near isotropy of the gamma radiation along with the large width of the state (γ^2 = 3 percent of the single particle limit) suggested dominant s-wave formation with some d-wave contribution. Analysis of elastic scattering excitation data at two angles led to a spin assignment of 2. However, this analysis is now known to be quite poor in view of a broad resonance near 1330 kev discovered in the course of the present experiment. The tail from this resonance extends into the 1 mev region and most certainly affects the shape of the anomaly near 997 kev, a fact not accounted for in the previous work.

Difficulties also existed in the isotopic spin assignment of the 997 kev state. Studies of the angular correlation of internal conversion pairs from the ground state capture radiation indicated large and nearly equal contributions of El and either E 3 or M2 transitions. The large El contribution indicated that the state has isotopic spin 1, since $0 \rightarrow 0$ isotopic spin electric dipole transitions are forbidden, as previously pointed out. This isotopic spin assignment is in conflict with the fact that the state produces both alphas and deuterons, a fact requiring isotopic spin zero. The reasons for an E3 contribution 10^3 times greater than that predicted by the single particle model in the ground state transition and the absence of a gamma transition to the 0.72 mev state in B^{10} also were not understood.

The narrow 1.085 mev resonance exhibited itself in $Be^9(p,p)$ and $Be^9(p,\gamma)$. Its absence in the deuteron and alpha producing reactions indicated that the state either had isotopic spin 1, or total angular momentum 0, even parity. The latter combination prohibits breakup into states with spin and parity 0^+(Be^8 or α) and 1^+(d or Li^6) by conservation of total angular momentum and parity. The smallness of the anomaly in the elastic scattering indicated a total angular momentum for the state of zero, since the magnitude of the anomaly increases with increasing J. A zero spin assignment was also consistent with known information on the gamma decay scheme.

The region between 1.1 and 2.5 mev had not been surveyed in detail. This fact, along with the discrepancies in assignments from earlier data discussed above, led to the inquiry reported in the present paper.

II. EXPERIMENTAL APPARATUS

1. General discussion

A schematic representation of the experimental arrangement is given in fig. 2A. Protons are accelerated in a 1.8 Mv electrostatic generator which was constructed in 1938(4) and partially rebuilt in 1946 and 1952(5). Upon emergence from the accelerator, the proton beam is separated into its H^+, HH^+, and HHH^+ components by means of a crossfield magnet, the desired component entering an 80° electrostatic analyzer, while the other components are blocked out by a slit system. The electrostatic analyzer is similar in design to that described by Fowler, et al(6), the plates having been built to a tolerance of one part in a thousand with a radius of curvature of one meter. The size of the entrance and exit slits of the analyzer determines its energy resolution ($E/\delta E$, where δE is the spread in energy of particles traversing the analyzer) which, for the usual slit widths of about 2mm. is around 500.

Upon emergence from the electrostatic analyzer and before entering the target chamber, the proton beam passes through horizontal and vertical slit systems which, in addition to collimating the beam, supply error signals to feedback systems that control the accelerating voltage and crossfield magnet strength, respectively.

After reaction, the emergent particles are analyzed by a high resolution double focussing magnetic spectrometer(7) which is mounted to allow a continuously variable scattering angle from 0 to 160 degrees with respect to the incident beam direction(8).

This variation is made possible by requiring the incident and emergent beams to lie respectively 10° above and below the horizontal plane, as indicated in fig. 2B.

Particles of the proper momentum emerge from the bottom of the magnet through an exit slit whose width determines the momentum resolution of the magnetic analyzer. During the present experiment a .1294 inch wide slit, corresponding to a momentum resolution ($\frac{P}{\delta P}$, where δP is the spread in momentum of the particles getting through the exit slit) of 293 was used.

The resultant analyzed particles are then counted by means of a .008 inch thick cesium iodide, thallium activated, scintillation crystal, backed by a DuMont 6291 photomultiplier, standard preamplifier, amplifier and scaling circuits.

The beam is moved on and off the target at the beginning and ending of each experimental run by means of a magnet activated by a current integrator that fires after a known amount of charge has been collected. The beam current discharges a capacitor whose change in voltage is fed to the grid of the normally cut off first stage of a high gain amplifier. The output of this amplifier activates a series of relays that turn on the magnet and shut off the scalars when the capacitor has been discharged.(9)

2. The electrostatic analyzer energy calibration

The equation obeyed by a particle of charge Ze, rest mass M, and velocity v, traveling in a circular equilibrium orbit of radius r in the presence of a radial electric field $\vec{E} = \frac{V}{r} / \ell n \frac{r_1}{r_2}$, where r_1 and r_2 are the radii of the analyzer plates, V, the difference of potential between the plates, is

$$\frac{ZeV}{r} \Big/ \ln\frac{r_1}{r_2} = \frac{Mv^2}{r\sqrt{1-v^2/c^2}} \tag{1}$$

The kinetic energy, E_{10}, of such a particle is given by

$$E_{10} = Mc^2 \left[\frac{1}{(1-v^2/c^2)^{\frac{1}{2}}} - 1\right] \tag{2}$$

Combining equations 1 and 2 gives

$$E_{10} = \frac{ZeV}{2}\left[\ln\frac{r_1}{r_2}\right]^{-1} \frac{(1 + E_{10}/Mc^2)}{(1 + E_{10}/2Mc^2)}$$

$$= \frac{ZeV}{2}\left[\ln\frac{r_1}{r_2}\right]^{-1}\left[1 + \frac{E_{10}}{2Mc^2} + \dots\right] \tag{3}$$

A small fraction of the potential difference V across the analyzer plates is fed into a potentiometer whose reading, E_{pot}, is then related to the particle energy by

$$E_{10} = ZC_{pot}\, E_{pot}\, (1 + E_{10}/2\,Mc^2 \dots) \tag{4}$$

The constant, C_{pot} is determined by consideration of a nuclear gamma ray resonance of known energy. If a thin target of thickness T in suitable energy units is bombarded by protons of energy near a narrow gamma ray resonance, the proton energy E_1 corresponding to the peak of the gamma yield is given by (10)

$$E_1 = E_R + T/2 \tag{5}$$

where E_R is the gamma ray resonance energy.

In general, E_1 differs from E_{10} for two reasons. First, the target itself is raised to potential V_T($\sim$300 volts) with respect to the equilibrium orbit of the analyzer in order to retard the escape of electrons knocked from the target by the incident beam. Secondly, small surface contamination layers that may be present on the target degrade the incident beam energy by a small amount, ΔE_1. Thus

$$E_{10} = E_1 + \Delta E_1 + ZeV_T \tag{6}$$

Combining 4, 5 and 6 gives

$$C_{pot} = \frac{E_R}{ZE_{pot}} \left[1 + \frac{T/2+\Delta E_1+ZeV_T}{E_R} - \frac{E_R}{2ZMc^2}\right] \tag{7}$$

Some methods of measuring ΔE_1 are given in Part 4 of Section III.

The electrostatic analyzer had been calibrated in the past by observing the many resonances in the reaction $F^{19}(p,\gamma)$. As a result of comparisons between the 873.5 and the (then) 1381 kev resonances, it was concluded that the calibration constant, C_{pot}, was a function of energy to the extent of 7 parts in 1000 over the range from 600 to 1400 kev. As a first step in the analyzer calibration at the outset of the present experiment, it was decided to check the validity of this conclusion.

Since the HH^+ molecules in the incident beam break up into two atoms upon striking the target, a beam of particles of some energy E can be obtained directly by using the mass one beam, or indirectly by using the mass two beam at an accelerating energy of 2E. By this method, the electrostatic analyzer calibration constants obtained at energies E and 2E can be compared. This procedure was carried out at the 669 and 873.5 kev resonances on a 2.4 kev (At E_{10} = 873.5 kev) fluorine target evaporated on a copper backing. The results, shown in fig. 3, indicate a variation in the calibration constant of 2 parts in 1000 between energies of 670 and 1740 kev. This variation being of the same order as that observed in a series of calibrations at the same energy, (see fig. 4) it is assumed that the electrostatic analyzer calibration constant is independent of energy. This conclusion, along with the calibration constants determined from the data of fig. 3, requires the former 1381 kev level to lie at 1373 kev. Later comparison of this resonance with the $Li^7(p,n)$ threshold by Dr. C. A. Barnes has established its energy as 1372 kev.

Periodically during the course of the present experiment, the electrostatic analyzer calibration has been rechecked. A summary of this data is given in fig. 4. The best value of the constant C_{pot} was .10075 ± .00010 during the course of the experiment. Following the completion of the present experiments, the electrostatic analyzer was dismantled and reassembled, causing the calibration constant to decrease somewhat.

3. The magnetic spectrometer energy calibration

The momentum P of a particle of charge Ze and rest mass M traveling in a circular equilibrium orbit of radius r under the influence of a magnetic field B is

$$Pc = ZeBr \tag{8}$$

The energy E_{20} of such a particle is given by

$$\begin{aligned} E_{20} &= \sqrt{P^2c^2 + (Mc^2)^2} \quad -Mc^2 \\ &= Mc^2 \left[\sqrt{\left(\frac{ZeBr}{Mc^2}\right)^2 + 1} \quad - 1 \right] \\ &= \frac{(ZeBr)^2}{2Mc^2} \left[1 - \left(\frac{ZeBr}{2Mc^2}\right)^2 + \ldots \right] \end{aligned} \tag{9}$$

Thus, in order to measure the energy of a particle traversing the magnetic spectrometer, it is necessary to measure only the magnetic field B that affects the particle. In practice, such a procedure is difficult. However, it was found at the time of construction of the magnet that the external stray field, B_o, was proportional to the field B in the equilibrium orbit.(8) It is this external field, B_o, that is measured by means of a fluxmeter apparatus of the following type.(5)

A current I passes through a coil placed in the field B_o and I is adjusted to produce a constant torque on the coil. Hence, when in adjustment,

$$B_o I = \text{constant} \tag{10}$$

Since B_o is proportional to B, equation 9 becomes

$$E_{20} = \frac{Z^2}{M} \frac{K_{sp}}{I^2} \left[1 - \frac{E_{20}}{2Mc^2}{}_2 + \ldots \right] \tag{11}$$

where K_{sp}, the magnetic spectrometer calibration constant is to be determined, and I is measured by means of a potentiometer device.

In practice, K_{sp} is determined from the energy position of the elastically scattered protons from a thick copper target. If the yield of resultant particles is plotted as a function of the fluxmeter current I, momentum profiles of the type shown in fig. 5 are obtained. The midpoint in the rise of the profile gives the I value corresponding to the energy of resultant protons scattered from the surface layer of the target.

This energy E_2 can be determined from the electrostatic analyzer calibration and the laws of conservation of energy and momentum, since

$$E_2 = \alpha E_1 \, . \tag{12}$$

E_1 may be obtained from equations 4, 6, and 7, and α is given, in the general case of particle 1 incident on particle 0, producing particles 2 and 3, by

$$\left(\frac{E_2}{E_1}\right)^{\frac{1}{2}} = \alpha^{\frac{1}{2}} = \frac{(M_1 M_2)^{\frac{1}{2}}}{M_2+M_3} \cos\theta \pm \left[\frac{M_3}{(M_2+M_3)} \frac{Q}{E_1} + \frac{M_3-M_1}{M_2+M_3} + \frac{M_1 M_2}{(M_2+M_3)^2} \cos^2\theta\right]^{\frac{1}{2}} \tag{13}$$

In general, E_2 differs from E_{20} because of a surface contamination layer of thickness ΔE_1 to protons of energy E_1, and because the target is raised to potential V_T. Hence

$$E_{20} = E_2 - \frac{\varepsilon_2}{\varepsilon_1} E_1 + ZeV_T \tag{14}$$

where ε_2 and ε_1 are the stopping cross-sections for protons of energies E_{20} and E_{10} in the contamination layer. Combining equations 11, 12, and 14 gives

$$K_{sp} = \frac{M\alpha I^2}{Z^2} E_{10} \left[1 - \frac{(\varepsilon_2 + \varepsilon_1 \alpha)}{\varepsilon_1 \alpha} \; \frac{\Delta E_1}{E_{10}} + \frac{(1-\alpha)}{\alpha} \frac{ZeV_T}{E_{10}} + \frac{\alpha E_{10}}{2Mc^2} \right] \qquad (15)$$

where I is now the fluxmeter current corresponding to the midpoint in the rise of the momentum profile.

The energy calibration of the magnetic spectrometer was repeated at regular intervals during the course of the experiment. To verify the constancy of K_{sp} with resultant particle energy and scattering angle, the many calibrations are plotted in fig. 6. This data indicates that the calibration constant, K_{sp}, is independent of both scattering angle and resultant particle energy to better than 1 part in 600 over the entire range of energies and angles used in the present experiment.

4. The magnetic spectrometer effective solid angle calibration

In principle there are two ways that an absolute cross-section can be determined. The first of these is to measure accurately all quantities that enter into the determination of the cross-section. This involves measuring current integrator capacitors and firing voltages, counter efficiencies, and the acceptance solid angle and resolution of the magnetic spectrometer. Since some of these quantities are difficult to determine, and since other uncertainties, such as the possible energy or angular variations of these quantities would, if not accounted for, give rise to appreciable errors in the determination of absolute cross-sections, a second method of measuring absolute cross-sections has been adopted in this experiment.

This method involves the comparison of the given cross-section to the assumed Coulomb cross-section for the elastic scattering of protons by copper. That is, approximate values of all quantities listed above, except the acceptance solid angle of the magnetic spectrometer, are assumed. From the yield of elastically scattered protons by copper, an effective acceptance solid angle is calculated by assuming the elastic scattering follows the well-known Coulomb law. This effective acceptance solid angle is then used in the calculation of the absolute cross-section of interest.

It was known at the outset of this experiment that the effective acceptance solid angle decreased by 7°/o at the largest scattering angles. This effect was thought to be caused by the large stray fields of the magnetic spectrometer warping the paths of the incident and resultant beams at the large scattering angles, since the spectrometer is in closest proximity to the electrostatic analyzer in this position. Movements of the incident beam in the target chamber or the resultant beam in the exit slits of the magnetic spectrometer were easily visible as the magnetic spectrometer was rotated. For this reason, a large piece of iron that comprised part of the target chamber was removed and an additional length of small diameter iron tubing, through which the incident beam passes, was added to the tubing already present. A light pipe system was also constructed at the exit slits of the magnetic spectrometer to guarantee that the resultant beam hit the scintillation crystal regardless of the relative beam position when traversing the exit slit. These improvements, along with the procurement of improved copper targets (See Part 7 of Section III) have reduced the variation of effective acceptance angle with scattering angle to about 3% (See fig. 7). A summary of the effective acceptance solid angle measurements during the course of the present experiment is given in fig. 8. It should be emphasized that this variation of the effective acceptance solid angle is that for the elastic scattering of protons from copper. The application of such a variation to the products of proton bombardment of beryllium is an approximation, since $\frac{E_2}{E_1}$, hence the stray magnetic field for a given incident particle energy is different in the two cases.

The variation of the effective acceptance solid angle with the incident beam position in the target chamber was checked after the iron target chamber piece was replaced and exit slit light pipe system inserted. There was no variation in the effective acceptance solid angle with vertical beam position over a range of four millimeters. The variation with horizontal beam position is shown in fig. 9. Since the beam position can be reproduced to about 0.2 millimeters and since the variation of the uncorrected beam position with scattering angle is of the order of one millimeter, a very small error is introduced as a result of the shifting beam, provided that the target is uniform.

The average forward angle effective acceptance solid angle measured during the course of the experiment was

$\Omega_L = 3.10 \times 10^{-3}$ steradians.

5. Particle detection equipment

In thick target studies of protons elastically scattered from beryllium, a background yield of deuteron and alpha reaction products is always present. Since this background yield produces voltage pulses somewhat smaller than those produced by elastically scattered protons when stopping in scintillating material, it was decided to improve the detection equipment in order to bias out this background yield. The former detection equipment, zinc sulfide scintillating powder dusted on a 1P21 photomultiplier tube, was replaced by a cesium iodide, thallium activated crystal, backed by a 6291 photomultiplier.

Typical integral bias curves with the new detection equipment are shown in fig. 10. Introduction of the new detection equipment reduced the background yield, as determined by the number of counts at the foot of a momentum profile, from an average of about 8% to 3% of the elastic proton yield.

III. EXPERIMENTAL TECHNIQUES

1. Determination of cross-sections from thick target data

If charged particles of energy E_{10} are incident on a thick target, the momentum profile plot of the number of resultant particles versus their momentum displays a sharp step at a momentum corresponding to the energy αE_{10}, where α is given by equation 13. This step corresponds to resultant particles produced in the surface layer of the target. At resultant particle energies less than αE_{10} the observed particles are those which are produced in a layer beneath the surface and which have suffered energy losses in passing through the target material before and after reacting. Typical momentum profiles are shown in fig. 5. When using thick target techniques, the yield at the peak of the momentum profile is obtained and converted into a cross-section in the following way.

By definition, $d\sigma/d\Omega$, the differential cross-section per unit solid angle in the laboratory system for the reaction producing N_R resultant particles that enter the magnetic spectrometer through solid angle Ω_L at laboratory angle θ_L when N_B incident particles bombard a region of a target of thickness t parallel to the incident beam and containing n disintegrable nuclei per unit volume, is

$$d\sigma/d\Omega = \frac{N_R}{N_B \Omega_L n t} \qquad (16)$$

The number of bombarding particles corresponding to N_R counts is given by

$$N_B = \frac{CV}{Ze} \qquad (17)$$

where C is the capacitance of a current integrator capacitor, V, its firing voltage, and Ze is the charge on the incident particle. The effective acceptance solid angle Ω_L is discussed in Part 4 of Section II. Thus, it remains only to determine the target thickness t within which N_R resultant particles at any one setting on the plateau of the resultant particle momentum profile are produced, in order to obtain the differential cross-section in the laboratory system.

Since the magnetic spectrometer passes all particles in the energy interval $\frac{\delta E_{20}}{2}$ about some energy E_{20}, and since, on the average, a given energy less than αE_{10} corresponds to a given depth in the target at which the resultant particle is produced, an energy spread in the resultant analyzed and counted particles corresponds to a region in the target in which these particles are produced.

For the quantitative relationship between the energy spread of resultant particles and the thickness t of the region in which they are produced, reference is made to the geometry of the bombarding process illustrated in fig. 11B. In the following derivations, it is assumed that the thick target is homogeneous and presents a smooth surface to the incident particles entering the target at angle θ_T and emerging at angle θ'_T with respect to the target normal. If ΔE_x is the energy lost by particles in traversing a distance x in the target, from fig. 11B,

$$\delta E_{20} = \frac{\partial E_2}{\partial E_1} \Delta E_t + \Delta E_b \tag{18}$$

where

$$\frac{\partial E_2}{\partial E_1} = a + E_1 \frac{\partial a}{\partial E_1} \tag{19}$$

The second term in the above equation is zero in the case of elastic scattering, as is seen from equation 13. Since

$$\Delta E_t = t\,\frac{dE_1}{dx}\,, \quad \Delta E_b = b\,\frac{dE_2}{dx}\,, \quad b = t\,\frac{\cos\theta_T}{\cos\theta'_T} \tag{20}$$

and

$$-\frac{dE}{dx} = N_s\, \varepsilon(E) \tag{21}$$

where N_s is the number of stopping atoms per unit volume, and $\varepsilon(E)$ is the stopping cross-section for particles of energy E in the target material, equations 18 through 21 can be combined to give

$$t = \frac{\delta E_{20}}{N_s \left[\varepsilon(E_{10})\,\frac{\partial E_2}{\partial E_1} + \varepsilon(E_{20})\,\frac{\cos\theta_T}{\cos\theta'_T}\right]} \tag{22}$$

The energy spread of particles passed by the magnetic spectrometer is given by

$$\frac{E_{20}}{\delta E_{20}} = \tfrac{1}{2}\,\frac{p}{\delta p} = \tfrac{1}{2}\,R \tag{23}$$

The momentum resolution R of the magnetic spectrometer is calculated from first order theory to be

$$R = 2\,(1+M)\,\frac{r_o}{\delta r} \tag{24}$$

where M is the magnification (0.8 in the present case), r_o the equilibrium radius (10.5 inches), and δr the width of the magnetic spectrometer exit slits (.1294 inches). Combining equations 16, 17, 22, and 23 gives,

$$d\sigma/d\Omega = \frac{N_s}{n}\ \frac{ZeN_R}{CV}\ \frac{R\left[\varepsilon(E_{10})\frac{\partial E_2}{\partial E_1} + \varepsilon(E_{20})\frac{\cos\theta_T}{\cos\theta'_T}\right]}{2\Omega_L\ E_{20}} \tag{25}$$

To determine the differential cross-section in the center-of-mass system, the above laboratory cross-section need be multiplied only by the ratio of the laboratory to center-of-mass solid angle which is

$$\frac{\Omega_L}{\Omega_{CM}} = \frac{\sqrt{1 - X^2 \sin^2\theta_L}}{\left[\sqrt{1-X^2\sin^2\theta_L} + X\cos\theta_L\right]^2} \tag{26}$$

where, for the general case of particle 1 incident on particle 0, producing particles 2 and 3

$$X^2 = \frac{M_1\ M_2}{M_o\ M_3} \Bigg/ \left[1 + \frac{(M_o+M_1)}{M_o}\ \frac{Q}{E_1}\right] \tag{27}$$

and E_1 is the actual reaction energy, determined as follows.

From fig. 11B,

$$\begin{aligned} E_1 &= E_{10} - \Delta E_{\ell\sec\theta_T} \\ E_{20} &= \left[E_{10} - \Delta E_{\ell\sec\theta_T}\right]\frac{\partial E_2}{\partial E_1} - \Delta E_{\ell\sec\theta'_T} \\ \Delta E_{\ell\sec\theta_T} &= \ell\sec\theta_T\ N_s\ \varepsilon(E_{10}) \\ \Delta E_{\ell\sec\theta'_T} &= \ell\sec\theta'_T\ N_s\ \varepsilon(E_{20}) \end{aligned} \tag{28}$$

Solving these equations for E_1 and ℓ yields,

$$E_1 = \frac{E_{20} + \dfrac{\varepsilon\,(E_{20})}{\varepsilon\,(E_{10})}\dfrac{\cos\theta_T}{\cos\theta'_T}\,E_{10}}{\dfrac{\partial E_2}{\partial E_1} + \dfrac{\varepsilon\,(E_{20})}{\varepsilon\,(E_{10})}\;\dfrac{\cos\theta_T}{\cos\theta'_T}} \tag{29}$$

and

$$\ell = \frac{\left(\dfrac{\partial E_2}{\partial E_1}\;E_{10}-E_{20}\right)}{\dfrac{\partial E_2}{\partial E_1} + \dfrac{\varepsilon\,(E_{20})}{\varepsilon\,(E_{10})}\;\dfrac{\cos\theta_T}{\cos\theta'_T}}\quad\frac{\cos\,\theta_T}{N_s\varepsilon\,(E_{10})} \tag{30}$$

The center-of-mass scattering angle θ_{CM} is obtained from the laboratory scattering angle θ_L from the equation,

$$\sin\,(\theta_{CM} - \theta_L) = X \sin\,\theta_L \tag{31}$$

For purposes of simplifying later theoretical calculations based on the present data, ratios of the measured elastic scattering cross-section to the calculated Coulomb cross-section are plotted. The Coulomb cross-section is given by

$$\frac{d\sigma_R}{d\Omega} = 1.296\left[\frac{Z_1 Z_o}{E_1}\left(\frac{M_o+M_1}{M_o}\right)\csc^2\frac{\theta_{CM}}{2}\right]^2 \times 10^{-3}\ \frac{\text{barns}}{\text{steradian}}$$

$$= \frac{.02562}{E_1^{\,2}}\csc^4\frac{\theta_{CM}}{2}\quad\frac{\text{barns}}{\text{steradian}}\quad\text{for Be}^9(p, p) \tag{32}$$

where E_1, M_1, and Z_1 are the reaction energy in mev in the laboratory system, mass, and charge of the incident particle, and Z_o and

M_o are the charge and mass of the target nucleus.

In the previous equations, the stopping cross-section for particles of the incident beam energy has been inserted in place of the correct stopping cross-section averaged between the incident and reaction energies. Similarly, the stopping cross-section of emergent energy particles rather than an average between the reaction and emergent energies, has been used. That these approximations introduce negligible errors can be seen by writing the approximate equation for the stopping cross-section

$$\varepsilon(E) = aE^{-b} \tag{33}$$

where b is roughly 0.5 experimentally for E greater than a few hundred kev. From the above equation,

$$\frac{d\varepsilon}{\varepsilon} = -b\frac{dE}{E} \tag{34}$$

and since $\frac{dE}{E}$ is of the order of 1°/o during the beam traversal before or after reaction, the fractional change in the stopping cross-section is of the order of ½°/o and the fractional difference between the stopping cross-sections for the incident and average energy particles is about 1/4°/o. Furthermore, $\varepsilon(E_{10})$ is smaller than the correct value and $\varepsilon(E_{20})$ is larger, both by about 1/4°/o. Thus, there is a further cancellation of errors and the resultant error in the experimental cross-section due to the choice of energies at which the stopping cross-section is evaluated is certainly negligible.

2. Thick target techniques

The position on the momentum profile at which data is recorded, hence the depth in the target at which the reaction occurs, can be adjusted by varying the quantity ($\alpha E_{10} - E_{20}$), as can be seen from equation 30. In running angular distributions (Cross-section versus scattering angle curves) or excitation curves (Cross-section versus reaction energy curves) the first step is to run a momentum profile at some angle and energy in order to determine a value for the following constant K in the expression

$$\alpha E_{10} - E_{20} = K E_{20} \tag{35}$$

From equations 4, 11, and 35, the relation between the electrostatic analyzer and magnetic spectrometer settings is then,

$$E_{pot} I^2 = \frac{(1+K) K_{sp} Z}{M C_{pot} \alpha} \tag{36}$$

If the following constant K is too small, data is obtained from the sloping front of the momentum profile and the full yield is not obtained. If K is too large, the incident particles must penetrate a great depth in the target before reacting. Thus, the straggling that arises from the fact that the energy loss of particles in matter is a statistical phenomenon becomes important, and the detailed structure of the profile is lost. In the present experiment, the following constant varied between 0.01 and 0.02 depending on the incident particle energy.

After making an appropriate choice of K, equation 36 can be used to obtain the magnetic spectrometer setting as a function of the electrostatic analyzer setting, and a whole series of thick target experimental yields may be determined without running momentum profiles at each point. It was in this fashion that the excitation curves of figs. 12 and 13 were obtained.

When running angular distributions, an additional condition is that the reaction energy E_1 of equation 29 remains constant during a series of variable angle measurements. This condition, along with the requirement of constant following depth expressed in equation 36, provides two equations in the two unknowns E_{pot} and I, which may be solved to yield

$$E_{pot} = \frac{E_1}{C_{pot}} \frac{\left[\frac{\partial E_2}{\partial E_1} + \frac{\varepsilon(E_{20})}{\varepsilon(E_{10})} \frac{\cos\theta_T}{\cos\theta'_T}\right]}{\left[\frac{\partial E_2}{\partial E_1} + \frac{\varepsilon(E_{20})}{\varepsilon(E_{10})} \frac{\cos\theta_T}{\cos\theta'_T} - \frac{M}{Z(1+K)}\right]} \qquad (37)$$

$$I = \frac{(1+K)Z K_{sp}}{ME_1 \frac{\partial E_2}{\partial E_1}} \frac{\left[\frac{\partial E_2}{\partial E_1} \frac{M}{Z(1+K)} + \frac{\varepsilon(E_{20}) \cos\theta_T}{\varepsilon(E_{10}) \cos\theta'_T}\right]}{\left[\frac{\partial E_2}{\partial E_1} + \frac{\varepsilon(E_{20})}{\varepsilon(E_{10})} \frac{\cos\theta_T}{\cos\theta'_T}\right]} \qquad (38)$$

Since E_{pot} varied by at most a few percent over the range of angles used at one energy, it was held fixed in the course of an angular distribution measurement and the following depth was varied slightly to compensate for this small error. The angular distributions of $Be^9(p,p)$ obtained by this method are illustrated in figs. 14 through 28.

3. Determination of cross-sections from thin target data

When a thin target is bombarded by monoenergetic particles, resultant particles with energy αE_{10} are produced in the surface layer of the target, and particles with energies somewhat less than αE_{10} are produced in succeeding depths of the target. However, since the target is not infinitely thick to the incident particles, resultant particles in only a narrow energy region below αE_{10} are produced. Hence, a thin target momentum profile will exhibit a group of resultant particles at a momentum dictated by kinematics and with a width related to the target thickness. Typical thin target momentum profiles are shown in fig. 29.

To deduce the cross-section from a thin target measurement, the entire momentum profile *in the neighborhood of the* particle group of interest is first obtained. The number of counts N(I) obtained at any fluxmeter setting I are those due to all particles with momenta in the interval $\frac{\delta P}{2}$ about the mean momentum P, which is related to I as indicated in Part 3 of Section II. The acceptance momentum interval δP is related to the acceptance fluxmeter current interval δI and the momentum resolution of the magnetic spectrometer, R, by

$$\frac{P}{\delta P} = \frac{I}{\delta I} = R \tag{39}$$

If y is the number of particles of a particular type produced in the target per incident particle, per unit solid angle, per unit interval in the fluxmeter scale, then y is related to N(I) by

$$y\, \Omega_L\, \delta I = \frac{N(I)}{CV/Ze} \tag{40}$$

The total yield Y per incident particle, per unit solid angle, is just the same yield per unit fluxmeter interval integrated over all fluxmeter settings. Hence, from equations 39 and 40

$$Y = \int y\,dI = \frac{ZeR}{CV\Omega_L} \int \frac{N(I)}{I}\,dI \tag{41}$$

The differential cross-section for the process producing the resultant yield Y per unit solid angle, per incident particle, is defined as

$$d\sigma/d\Omega = \frac{Y}{nt} \tag{42}$$

Equations 41 and 42 combine to give

$$d\sigma/d\Omega = \frac{ZeR}{CV\Omega_L nt} \int \frac{N(I)}{I}\,dI \tag{43}$$

The thickness t of the thin target may be determined in a variety of ways, some of which will be discussed in the following section.

4. Thin target techniques

Thin target techniques have been used in the measurement of the $Be^9(p,d)$ and $Be^9(p,\alpha)$ angular distributions at 333 kev shown in figs. 30 and 31, the $Be^9(p,\alpha)$ and $Be^9(p,d)$ excitation curves near 470 kev at $\theta_L = 138^o$, shown in fig. 32, the $Be^9(p,p)$ excitation curves near the 1084 kev resonance shown in figs. 33 and 34, and the forward angles of some of the $Be^9(p,p)$ angular distributions of figs. 14 through 28.

The 333 kev $Be^9(p,d)$ and $Be^9(p,\alpha)$ angular distributions were obtained to check the validity of the elastic scattering analysis which concluded that the 330 kev resonance level in B^{10} is formed by s-waves, a conclusion requiring isotropic reaction product angular distributions. Thin target techniques were used in an attempt to separate the resultant deuteron, alpha, and Li^{6++} groups, all of which appear at nearly the same magnetic spectrometer setting in this energy region. The target used in the absolute cross-section determinations was a $4\frac{1}{2}$ kev (to 1 mev protons) beryllium layer evaporated on a chromium plated brass backing. The target thickness was determined by the momentum width of the deuteron and alpha groups and also by the difference in momentum of protons elastically scattered from chromium through the beryllium layer and protons scattered from a clean chromium surface. This target proved unsatisfactory at the forward angles since it was suitable only for reflection experiments that become uncertain at forward angles due to the small glancing angles of incidence and reflection. Thus, forward angle relative determinations were made by using an unsupported beryllium foil as a target in a transmission experiment. These relative cross-sections were then normalized to the absolute data obtained from the beryllium on chromium target.

The excitation curves for $Be^9(p,d)$ and $Be^9(p,\alpha)$ at $\theta_L = 138^o$ were run near 470 kev to check earlier data$^{(11)}$ that exhibited a peak in the deuteron cross-section and no anomaly in the alphas near this energy. The results, which are shown by fig. 32 to be in essential agreement with the earlier work, were obtained from the beryllium target evaporated on a chromium backing by the previous techniques, with but one exception. In the particular energy and angular region under discussion, the resultant deuterons and alphas from a thin target emerge through the magnetic spectrometer at identical field settings. The separation of the counts at any magnetic spectrometer setting into the two particle groups of interest was accomplished by pulse height analysis. This is possible since the resultant alphas possess twice the energy of deuterons passing through the magnetic spectrometer at the same setting, hence produce somewhat greater voltage pulses upon stopping in a cesium iodide scintillation crystal.

Thin target techniques were used to make measurements at the forward angles in several of the angular distributions for $Be^9(p, p)$ in order to check on the validity of thick target reflection data obtained as far forward as 60° with resulting glancing angles of incidence and reflection of 30°. Thin unsupported beryllium foils were used to obtain these relative angular distributions which were normalized to the absolute thick target measurements at the largest scattering angle that thin target data was taken. The general agreement between this thin and thick target data is evidenced in figs. 19, 21, and 23.

In the study of the 3 kev wide 1084 kev resonance it was desired to use a target much thinner than the width of the resonance in order to insure that the decrease in energy resolution due to finite target thickness was small compared to the width of the state of interest. To meet this requirement a target composed of a 2/3 kev layer of beryllium evaporated on a 5 kev unsupported nickel foil was prepared. The target thickness was determined from the difference in momentum of protons scattered from the nickel foil through the beryllium and protons scattered from a clean nickel foil. Relative cross-sections, normalized to values in the excitation curves and angular distributions, were obtained as follows.

From equation 43 it is seen that if the momentum profile is restricted to a narrow region of fluxmeter currents, the cross-section is proportional to the area under the momentum profile curve. Since, in the present case of a target much thinner than the momentum resolution of the magnet, the width of the momentum profile is the width of the magnet acceptance momentum interval and is a constant over a narrow region of momenta, the area under a momentum profile is proportional to the number of counts at its peak. Hence, relative cross-sections may be obtained from the number of counts at the peak of the momentum profile, and it was in this way that the data of figs. 33 and 34 was obtained. The two percent error indicated on this data arises from statistical fluctuations and the error involved in determining the peak of the momentum profile.

5. The stopping cross-section of protons in beryllium

Since the stopping cross-section of particles in a given target material enters into the determination of thick target cross-sections and thin target thicknesses, its measurement is an essential part of any complete experimental procedure. The stopping cross-section, $\varepsilon(E)$, is defined from

$$\varepsilon(E) = \frac{-1}{N_s}\frac{dE}{dx} \qquad (21)$$

where N_s is the number of stopping atoms per unit volume. Thus, an absolute determination of the stopping cross-section requires measurement of the energy loss of a beam in passing through the material of interest and a knowledge of the number of stopping atoms per square centimeter of this material. Since this latter quantity is a constant for any given target, relative stopping cross-sections may be obtained by measuring only the energy loss of particles in traversing the target of interest. In this manner the relative stopping cross-sections for protons of energies between 250 and 2600 kev in beryllium (fig. 35) were obtained after normalizing to the absolute measurements of Bader.(12)

For these relative measurements, a target was prepared by evaporating a thin layer of beryllium on half of a thick copper target. The energy loss of protons in the beryllium was determined from the difference in energy between protons elastically scattered from the clean copper surface with energy E_{20} and from the copper surface through the beryllium layer with energy E'_{20}. This difference is proportional to the stopping cross-section of protons in beryllium at some energy E_x which is determined from the energies E_{20} and E'_{20} as(8)

$$E_x = \frac{E_{20}+E'_{20}}{1+a} + \frac{E_{20}-E'_{20}}{2(1+a)}\left(\frac{\eta - a}{\eta + a}\right) \qquad (44)$$

where

$$\eta = \frac{\varepsilon(E_{20})}{\varepsilon(E_{10})}$$

$$a = E_2/E_1 \qquad \text{for Cu(p, p)}$$

The second term in the above expression being at most a few percent of the first term, the stopping cross-sections required to calculate it may be obtained with sufficient accuracy by using only the first term in the above equation to determine the energy to which the relative stopping cross-section measurement applies.

6. Target surface contamination

The presence of contamination layers on a target surface must be guarded against continually since it can affect the yield of the particles of interest in several ways.

One way results from the straggling of the incident and resultant particles in the surface contamination layer. In addition to decreasing the energy resolution, such a straggling tends to cause a rounding of the top of the thick target step in the momentum profile, as can be seen by comparison of the two profiles of fig. 5 in which the same amount of surface contamination produces a relatively greater effect at the lower energy. If such a rounding of the thick target step becomes appreciable, the following point is no longer at the top of the momentum profile and a reduced yield is obtained.

A second troublesome effect occurs in elastic scattering experiments if the surface contamination layer has nearly the same atomic weight as the target of interest. In this case, tails from the contamination layer elastic scattering peaks may extend into the region of momenta corresponding to the elastic scattering peak from the target of interest, and a false high yield is obtained unless this background yield is subtracted. This problem is most prevalent at low energies and forward angles where the carbon and oxygen contaminant, and beryllium target elastic scattering peaks are in closest proximity to each other.

For these reasons, the buildup of surface contamination layers with bombardment, an effect that becomes appreciable for incident particle energies less than about 600 kev, should be kept at a minimum. The combination of frequent target changes and heating of the targets during bombardment was found to reduce surface contamination layer buildup to a negligible amount. In fig. 36, the rates of surface contamination layer buildup with bombardment for heated and unheated targets are compared.

7. Target surface roughness

In a study of nuclear reactions, the quality of smoothness of the target surface under consideration is an important parameter in determining relative thick target yields and the resultant absolute cross-sections. That yields may be affected by a rough or scratched surface has been shown through an experimental inquiry into the number of elastically scattered protons from different types of thick copper surfaces.

Since absolute differential cross-sections are determined by comparing the yield from a given reaction to that from the assumed Coulomb scattering of protons by copper, in the course of the present experiment several determinations of yields from copper targets were made, and it was observed that there were day to day variations in yield of about 5°/o. In an attempt to understand the cause of this variation, the following three types of copper targets were prepared and bombarded:

I. A copper target made from machine shop electrolytic copper was polished with 2-0 emery polishing paper, washed, polished with 4-0 emery polishing paper, and cleaned in petroleum ether. (This is the polishing procedure used on targets whose results are described above.)

II. A copper target made from chemically pure copper was polished to an optical flat by use of polishing paper, diamond dust, and etching, by Dr. F. S. Buffington of the Caltech Metallurgy Department.

III. Copper was evaporated on chromium-plated brass sheets.

Of these three target types, II and III gave the same reproducible elastic proton yields while the results from type I were typically 9% low and variable. That this is due to something in the polishing procedure used on targets of type I was shown by polishing targets II in this fashion and obtaining a reduced yield.

The phenomena might be due to a contamination layer introduced in the polishing procedure, but this explanation is doubted because:

(a) Machined, unpolished surfaces produced the same low yields.

(b) Momentum profiles of the elastically scattered protons indicated clean copper surfaces by virtue of the fact that the yield rose from zero to the maximum value in a momentum interval comparable to the momentum resolution of the magnetic spectrometer used in the analysis of the scattered protons. This was independent of the type of surface under bombardment, and would not be the case if contaminant were present, since straggling effects would tend to broaden the top and bottom of the step.

(c) No contaminant was observed on the target surface under a high-powered microscope.

A second plausible explanation for the reduced yield is that scratches on the rough target surface are responsible. That is, if a proton incident near the bottom of a scratch emerges through the smooth part of the target surface after reacting, it traverses a distance in the target of the order of the scratch depth. If this distance is much greater than the normal path length in copper of the resultant analyzed and counted particles, protons incident near the bottom of a scratch emerge with a momentum less than that required to traverse the resultant particle magnetic spectrometer and be counted. Thus, a reduced yield from scratched targets would be observed.

A simple qualitative calculation shows that this is a reasonable mechanism for yield loss. After polishing a target surface with 4-0 emery polishing paper, the deepest scratches observed under a microscope were of the order of 3 microns. The energy difference between incident and resultant protons in a typical experiment might be thirty kev. In copper at a bombarding energy of 700 kev, this corresponds to a penetration of about 0.5 microns in the target by the incident proton beam. Since the scratch depth is six times this great, any proton incident near the bottom of a scratch is expected to be lost, by virtue of the previous argument.

To test this theory further, two experiments were performed on a copper target surface, parts of which were scratched to a maximum depth of the order of 5 microns in horizontal and vertical directions. In the first of these experiments, yields from the vertically and horizontally scratched surfaces relative to that from a smooth surface were obtained as a function of the scattering angle. These results are shown in fig. 37. To correlate these results with the general ideas developed above, a theory based on the hypothesis that the reduced yield is caused by the scratched surface must be shown to produce the correct angular dependence of relative yield for the two types of scratches.

As the first step in the development of this theory it must be realized that the only component of a scratch effective in reducing the yield of elastically scattered protons is that component perpendicular to the beam plane, i.e., the plane formed by the incident and resultant beams. Thus, if α_V and α_H are the angles between this beam plane and the vertical and horizontal scratches respectively, and if F is the fraction of the surface scratched, then $F \cos \alpha_{V,H}$ is the fraction of the scratched surface that is effective in reducing the yield. To determine $\alpha_{V,H}$ the geometry of the scattering process must be considered.

In fig. 38 the target (not shown) is in a vertical plane, while, for reasons of obtaining a larger range of scattering angles, the incident and resultant proton beams lie respectively 10° above and below the horizontal plane. Hence, θ_{sp}, which is the component of the laboratory scattering angle in the horizontal plane, and which is the experimentally measured angle in any experiment, is related to the actual laboratory scattering angle, θ_L, by

$$\cos \theta_L = \sin^2 10^\circ + \cos^2 10^\circ \cos \theta_{sp} \tag{45}$$

With α_V and α_H defined as above, it can also be shown that

$$\cot \alpha_H = \tan \alpha_V = \tan 10^\circ \tan \theta_{sp}/2 \tag{46}$$

As a second step in the development of the theory, the loss of yield from a proton beam incident on one scratch must be determined. In doing this, a scratch will be replaced by an isosceles triangular indentation as illustrated in fig. 11A. In this figure, $\theta_T = \theta_T'$ is the angle between the normal to the target and either the incident or emergent beam, and is related to θ_{sp} by

$$\cos \theta_T = \cos 10^\circ \sin \theta_{sp}/2 \tag{47}$$

The distance S that a particle travels in the target before reacting is determined by the energy difference between incident and resultant beams and was constant throughout the experiment under discussion.

According to this triangular abstraction of a scratched surface, all incident protons in either the shaded or cross-hatched regions in fig. 11A feel the presence of the scratch. But since the protons in both shaded regions may travel some distance other than S, react, and emerge with the proper momentum to be analyzed and counted, it is assumed that no loss of yield accompanies these end effects. This is an especially good approximation, relatively speaking, if $D >> S$, which is nearly the case in the present experiment. Thus, if complicating effects from other scratches near enough to the scratch of interest to influence the particles that enter that scratch are neglected, only the proton beam in the cross-hatched region is lost as far as producing reaction products is concerned.

Since $\frac{2R - 2L(\tan\theta + \tan\phi)}{2R}$, the ratio of the cross-hatched length to the scratch length, is the fraction of the scratch effective in reduction of yield, and $F \cos \alpha_{V,H}$ is the fraction of the surface scratched in a direction perpendicular to the beam plane, the fraction of incident particles lost is $[1 - \frac{S}{R}(\sin\theta_T + \cos\theta_T \tan\phi)]F \cos\alpha_{V,H}$. In the derivation of this expression it is assumed that $R > S(\sin\theta_T + \cos\theta_T \tan\phi)$ and $\theta_T > \phi$. If either of these conditions is violated, all particles that enter the scratch are scattered from some depth beneath the scratch and can re-emerge through the scratch with the proper momentum to be analyzed and counted.

If G is the fraction of the total yield obtained at angle θ_T from scratches of half interior angle ϕ, then

$$G = \begin{cases} 1 - F\cos\alpha_{V,H}\,[1 - \frac{S}{R}(\sin\theta_T + \cos\theta_T \tan\phi)] & \phi < \beta \\ 1 & \phi > \beta \end{cases} \qquad (48)$$

where β is the smaller of the two values obtained from $\beta = \theta_T$, and $\tan\beta = \frac{R/S - \sin\theta_T}{\cos\theta_T}$.

This expression must be averaged over all angles ϕ to obtain the experimental decrease in yield from a scratched surface. For a uniform distribution of angles ϕ between 0 and $\pi/2$,

$$G = 1 - \frac{2\beta}{\pi} F \cos \alpha_{V,H} [1 - \frac{S}{R} \sin \theta_T] + \frac{2SF}{\pi R} \cos \alpha_{V,H} \cos \theta_T \ln \sec \beta \qquad (49)$$

For a Gaussian distribution of angles ϕ about a mean μ with standard deviation σ,

$$G = 1 - \frac{a}{c} F \cos \alpha_{V,H} [1 - \frac{S}{R} \sin \theta_T] + \frac{b}{c}\frac{S}{R} F \cos \alpha_{V,H} \cos \theta_T$$

$$\text{where } a = \frac{1}{\sqrt{2\pi}} \int_{-\mu/\sigma}^{\frac{\beta-\mu}{\sigma}} \exp(-t^2/2)dt \quad b = \frac{1}{\sqrt{2\pi}\,\sigma} \int_0^{\beta} \tan\phi \exp[\frac{(\phi-\mu)^2}{2\sigma^2}] d\phi \qquad (50)$$

$$c = \frac{1}{\sqrt{2\pi}} \int_{-\mu/\sigma}^{\mu/\sigma} \exp(-t^2/2)\, dt$$

Plots of G for each of these distributions are shown in fig. 37. In these curves F = .40 and R = 5 microns, values in good agreement with what one observes under a microscope. The length S was fixed by the constant difference between initial and final proton energies as 0.75 microns.

It is seen that the general shapes of the theoretical curves for the relative yields of protons from vertically and horizontally scratched targets are independent of any assumption on the distribution of ϕ. The general agreement between experiment and theory is taken as evidence that scratches on the surface are responsible for the reduced yield.

The second experiment performed on rough target surfaces in an attempt to understand the nature of the reduced yield phenomenon involved the variation of relative yield with target angle. If the angle θ_T between the target normal and incident beam is varied while the incident energy E_{10}, resultant energy E_{20}, and laboratory scattering angle θ_L, remain fixed, experimental data of the type shown in fig. 39 is obtained.

The theoretical variation in relative yield from a smooth surface as a function of target angle is given by equation 25. For the particular energy and scattering angle illustrated in fig. 39, the theoretical equation for the yield $Y(\theta_T)$ as a function of target angle θ_T is

$$\frac{Y\,(\theta_T)}{Y\,(60^{\circ}30')} = \frac{30.65}{14.94 + 15.71\,\frac{\cos\theta_T}{\cos(121^{\circ} - \theta_T)}} \tag{51}$$

It should be noted that this theoretical expression is expected to break down for large target angles since it is experimentally obvious that $Y(90^{\circ}) = 0$.

However, for smaller target angles, the agreement shown in fig. 39 between experiment and the theory for a smooth target surface is very good, even in the cases of vertically and horizontally scratched surfaces. This latter phenomenon would seem to be quite unexpected from the point of view of the scratch theory of reduced yields, because a rough target surface corresponds to a range of allowable θ_T, hence an averaging over some region of the theoretical curve for a smooth surface. The result is that one expects a rough surface to produce a yield curve with a smaller slope than that for a smooth surface. However, a simple qualitative argument shows that this effect is quite small.

Since 40% of the target surface is scratched and about 10% of the incident beam is lost in the scratches, about 33% of the emergent proton beam feels the presence of the scratches. However, not all of these protons produce a perturbing yield independent of θ_T, since those protons incident on the back side of a scratch and emergent through the smooth surface follow the same dependence on θ_T as do those protons incident on a smooth surface. This fact can be seen by examining fig. 11B and observing that the derivation of the thick target differential cross-section as a function of θ_T is the same whether the surface near the point of impingence of the incident beam is the flat or dashed, triangular, surface.

It is assumed that all protons incident on the back side of a scratch emerge through the smooth surface. This is true for small θ_T, because $\theta_T + \theta_T' = 121^\circ$, so θ_T' is large. For large θ_T, θ_T' is small, and the distance that the scattered beam travels before emergence from the target is liable to be less than S. To fulfill the condition that the proton travels a distance of the order of 2S in the target, it must travel a distance greater than S before reacting, hence, most likely emerges through the smooth surface. With this assumption, the perturbing yield is seen to arise from those protons incident on the front side of a scratch.

For $\theta_T > \phi$, no protons are incident in this manner. For $\theta_T < \phi$, anywhere from zero to half of the protons incident on a scratch strike the front surface. Hence as a rough estimate, it may be said that on the average, one-eighth of the protons incident on a scratch hit the front surface. Since about one-third of the resultant protons are incident on scratches, the perturbing yield is expected to be about $4^{o}/o$ of the total yield.

If this perturbing yield is independent of the target angle θ_T, then one expects:

$$\frac{Y(\theta_T)}{Y(60^\circ 30')} = .96 \; \frac{30.65}{14.94+15.71 \; \dfrac{\cos\theta_T}{\cos\,(121^\circ - \theta_T)}} + .04 \qquad (52)$$

At $\theta_T = 50^\circ$, this amounts to a yield increase of about $2^{o}/o$.

In conclusion, it seems reasonable to say that a scratched target surface reduces the yield of scattered particles in a manner dependent on the direction and depth of the scratches and on the angle of scattering. If this phenomenon is to be avoided, roughness on target surfaces must be kept below a fraction of the depth of penetration of that part of the incident proton beam that produces the observed reaction products. This means that an optically flat surface is required in the accurate determination of relative thick target yields and the resultant absolute cross-sections.

Unscratched beryllium thick targets were prepared by polishing 1/4 inch diameter beryllium disks in the following way. The beryllium disk is first mounted in a plastic mold one inch in diameter and is then polished with Axolite 120 through 400 polishing paper using a 10°/o oxalic acid solution directly on the polishing paper as an etchant. Following this procedure, the final polish is obtained on a Microcloth wheel using a mixture of 10°/o oxalic acid and 1552AB Gamma Polishing Alumina number 3 which has a grain size of 0.1 microns, this combination serving as a simultaneous abrasive and etching agent.

8. Corrections to the experimental yields

Before determining cross-sections from a thick or thin target yield by the methods previously discussed, the experimental yield must be corrected for three small effects.

The first of these effects involves the subtraction of any background yield that may arise from surface contamination layers on the target or, in the case of elastic scattering studies with thick targets, from the deuterons or alphas produced deep enough in the target to emerge with the same momentum as the protons elastically scattered from the surface layers. This background yield, determined from the magnitude and energy variation of the yield at the foot of the momentum profile of interest, was always less than 10°/o of the yield of interest and averaged about 1/3 of this amount throughout the entire experiment.

A second correction to the experimental yield arises from the dead time of the detection equipment. If two particles arrive at the scintillation crystal within some time interval τ, only one pulse is recorded on the scaling unit. The fractional decrease in counting rate, $\frac{\Delta N}{N}$, is given to a high degree of accuracy by the probability $u(\tau)$ that in the time interval τ following the arrival of a particle at the scintillation crystal, a second particle also arrives. This equating of $\Delta N/N$ to $u(\tau)$ neglects the additional loss in counting rate that arises from three or more particles arriving at the scintillation crystal within the time interval τ, but since this probability is small compared to $u(\tau)$, no appreciable error is made in neglecting it.

If a particle arrives at the scintillation crystal at time t_o, the probability $du\,(t'-t_o)$ of the next particle arriving at the scintillation crystal in the time interval dt' around t' is given by

$$du(t'-t_o) = [1 - u(t'-t_o)]\,\nu\,dt' \tag{53}$$

where ν is the average frequency of particle arrival at the crystal. Integrating equation 53 from $t' = t_o$ to $t' = t_o + \tau$ and setting the result equal to $\frac{\Delta N}{N}$ gives

$$\frac{\Delta N}{N} = 1 - e^{-\nu\tau} \approx \nu\tau \tag{54}$$

By means of a double pulser that produces two pulses separated by a variable time interval, the dead time τ of the counting equipment has been measured as about 10^{-5} seconds. However, particle yields obtained with variable counting rates indicate a smaller value of the dead time, hence the value $\tau = 5\text{x}10^{-6}$ seconds has been adopted. In the course of the present experiment the dead time correction was never allowed to be greater than 2°/o of the total yield.

A third correction to the total yield arises from the fact that the magnetic spectrometer is set to pass only the positively charged component of the resultant protons or deuterons and the doubly charged component of the resultant alpha particles. At proton or deuteron energies less than about 200 kev or alpha energies less than about 1.5 mev, the singly charged positive component of the alphas, and the neutral and negatively charged components of all three types of particles become appreciable and must be accounted for. No correction to any experimental deuteron yields was made for charge neutralization. However, the alpha yields in the angular distribution at 333 kev and in the excitation curves near 470 kev had to be increased by about 16°/o to compensate for neutral and singly charged alphas that were not being counted. Similarly, the elastic proton yields below about 200 kev were corrected by up to 20°/o.

The method of correction of the data for the components of the resultant beam that were not being counted relies on the fact that charge exchange cross-sections are so large ($\sim 10^{-16}$ cm^2) that the charge equilibrium ratios are determined by the last few atoms on the target surface.(13) Since the last few atoms on the target surface comprise the surface contamination layer, the charge equilibrium ratios should be independent of the target material under bombardment. Thus, the correction for the singly charged and neutral alpha particles may be obtained from Allison and Warshaw(14), and the correction for neutral and negatively charged resultant protons may be obtained from the deviation of the low energy cross-section for the elastic scattering of protons by copper from the Coulomb cross-section. Before attributing these low energy deviations to charge neutralization, the resultant data must first be corrected for the screening effect of the orbital electrons in copper. Wensel(15) calculates that this screening effect, which is inversely proportional to E, decreases the ratio-to-Rutherford elastic scattering cross-section for protons on copper by about $2\frac{1}{2}$°/o at 200 kev. The ratio of the measured elastic scattering cross-section for protons on copper to the calculated Coulomb cross-section, corrected for the screening of the orbital electrons, is plotted as a function of the resultant particle energy in fig. 40. This curve is also taken as the probability that the emitted proton is positively charged, hence the yields of protons elastically scattered from beryllium have been corrected by this curve for the uncounted neutral and negatively charged resultant protons.

9. Probable errors in the experimental absolute cross-sections

Except where otherwise specifically noted, the total uncertainty in the absolute cross-sections of figs. 12 through 34 averages about 7°/o. This uncertainty arises from the various probable errors listed in Table I.

TABLE I. Probable Errors in Absolute Cross-Section Measurements

SOURCE OF ERROR	PERCENT ERROR
1. Statistical counting fluctuations	1.5
2. Background subtraction	1.5
3. Corrected for dead time of counting equipment	0.5
4. Current integrator uncertainties	0.5
5. Effective solid angle measurement	
(a) Statistical counting fluctuations in Cu(p,p)	1.0
(b) Uncertainty in $\mathcal{E}_{Cu}$	4.0
(c) Assumption that Cu(p,p) is Rutherford	?
(d) Equating Ω_L from Cu(p,p) to Ω_L for $Be^9(p,p)$	?
(e) Uncorrected variation with angle	1.5
6. Uncertainty in the stopping cross-section of protons in beryllium	4.0
7. Uncertainty in scattering angle measurement	1.0
8. Uncertainties in E_{10} and E_{20}	0.3

Total probable error 7%

IV. THEORETICAL ANALYSIS OF THE ELASTIC SCATTERING DATA

1. Introduction

In general, two types of analysis may be performed on elastic scattering experimental data. The first type, applicable when the resonance of interest is relatively narrow, involves the analysis of excitation curves. The second type, applicable to broader resonances, involves detailed fitting of angular distributions.

In the narrow level type of analysis, excitation curves in the region of the resonance are studied at angles corresponding to the zeroes of the various Legendre polynomials. It will be shown that under the assumption of the formation of no more than one non s-wave state in the compound nucleus by protons of one orbital angular momentum, the anomaly in the elastic scattering cross-section that arises from the coherent interference of the background and Coulomb amplitudes with the resonance amplitude disappears at the zero of the Legendre Polynomial corresponding to the ℓ-value of the proton wave forming the resonance level. The result is an anomaly at this particular angle that increases the cross-section symmetrically about the resonance energy. Hence, a casual survey of the cross-section excitation curves at a series of angles might be hoped to yield the parity of the compound nuclear state and to limit its total spin to at most one of $(2\ell+1)$ possible values. The total spin can further be determined by the size of the cross-section anomaly which depends on a statistical factor involving the total spin. Detailed fitting of the excitation curves at all angles can then be accomplished by assuming that the energy variation of non-resonant phase shifts or of the resonant channel potential phase shift is negligible over the region of the narrow resonance.

If these variations are not negligible over the region of the resonance, the detailed fitting of the excitation curves becomes impossible since no accurate a priori energy variation of non-resonant or potential phase shifts can be assumed. In this case, the broad level type of analysis must be employed. In broad level analysis, theoretical fits of the experimental angular distributions are obtained with arbitrary fitting parameters that are related to these resonant, non-resonant, and potential phase shifts. The energy dependences of these fitting parameters are then studied in an attempt to determine the existence and properties of the states in the compound nucleus B^{10} formed by the interaction of Be^9 and protons.

2. Derivation of theoretical cross-section equations

(a) General derivation

The first problem in either the broad or narrow level type of analysis is to derive a theoretical equation for the cross-section of the process $Be^9 + p \rightarrow B^{10*} \rightarrow Be^9 + p$ subject to the conditions of the conservation of parity and

$$\vec{J}_{Be} + \vec{J}_p + \vec{\ell} = \vec{J}_B = \vec{J}'_{Be} + \vec{J}'_p + \vec{\ell}' \tag{55}$$

$$m_{Be} + m_p + m_\ell = m_B = m'_{Be} + m'_p + m'_\ell \tag{56}$$

where the $\vec{J}$'s are total vector spins, the m's are components of the $\vec{J}$'s along the direction of the incident plane wave, and the prime quantities refer to reaction products. It is experimentally known that $J_{Be} = J'_{Be} = 3/2$ and $J_p = J'_p = \frac{1}{2}$. Furthermore, the plane wave nature of the incident beam requires $m_\ell = 0$ since the operator corresponding to the z-component of angular momentum is $-i\hbar \frac{\partial}{\partial\phi}$, and a plane wave has no ϕ-dependence. Thus, the most general theoretical elastic scattering cross-section is calculated by summing over all possible amplitudes for the elastic scattering process that arise from all allowable combinations of ℓ, ℓ', m'_ℓ, m_B, J_B, m_{Be}, m'_{Be}, and m'_p.

The problem is simplified from this infinite complexity by explicit assumption of the particular values for ℓ, ℓ', and J_B to be considered in the construction of the theoretical cross-section equation of interest. In the present case, for reasons that will later become clear, the allowed values of ℓ, ℓ' and J_B have been chosen as follows:

(a) $\ell = 0, 2 \quad \ell' = 0, 2 \quad J_B = 1^-, 2^-$

(b) $\ell = \ell' = 1 \quad J_B = 0^+, 2^+$ with $J_B = 2^+$ being formed only by channel spin one.

The formalism of describing initial and final particle configurations in terms of channel spins is adopted. In this formalism, the angular momenta of Be^9 and the proton are combined to form a channel spin and its z-component. Thus, the total spin in a channel,

J_{ch}, and its z-component, m_{ch}, are given by

$$\vec{J}_{ch} = \vec{J}_{Be} + \vec{J}_{p} \qquad m_{ch} = m_{Be} + m_{p} \tag{57}$$

It therefore follows that J_{ch} equals 1 or 2, and the eight possible substates of a spin 3/2 particle (4 substates) combining with a spin $\frac{1}{2}$ particle (2 substates) are represented in terms of the eight possible substates of spins 2 (5 substates) and 1 (3 substates). The combination of a channel spin and its z-component will hereafter be called a channel spin configuration and will be written (J_{ch}, m_{ch}).

Following the calculation of the many amplitudes for the elastic scattering process subject to the conservation of parity, total spin, and its z-component, the theoretical cross-section is obtained by taking the absolute square of the sum of these amplitudes and averaging over initial and summing over final channel spin configurations. Since this summation involves both coherently and incoherently interfering amplitudes, it is mathematically convenient to tabulate the various amplitudes by groups having the properties that all amplitudes within a group interfere coherently while all amplitudes between groups interfere incoherently. The theoretical cross-section is then obtained by taking the absolute square of each group and summing over all groups, taking care to divide the result by 8 to account for the averaging over initial channel spins.

Since no experimental technique can differentiate two scattering processes possessing the same initial and final channel spin configurations, such processes interfere coherently regardless of differences in intermediate orbital angular momentum or compound nucleus configurations. Hence, the tabulations of the many amplitudes for the elastic scattering process are carried out in groups of constant initial and final channel spin configurations. To do this, an eight-by-eight amplitude matrix is constructed. The rows or columns of the amplitude matrix correspond respectively to the eight possible configurations of initial or final channel spins 1 and 2. Each element in the amplitude matrix is the summation of all possible amplitudes for the formation and break up of a compound nuclear state of spin J_B by orbital angular momenta ℓ and ℓ' through the given initial and resultant channel spin configurations.

The most general term in any of the matrix elements is a product of three parts: two Clebsch-Gordon coefficients that represent the probability amplitudes for formation and decay of the compound nucleus through a particular combination of channel spins and orbital angular momenta, an angular dependent factor given by the spherical harmonic $Y^{m'}_{\ell'}$, and a group of constants and phase shift dependent terms that at present will be denoted by $f^{J_B}_{J_{ch}, J'_{ch}, \ell, \ell'}$. The amplitude matrix for the situation described above is given in fig. 41. In this figure, f_c represents the Coulomb scattering amplitude and is given by the equation

$$f_c = \sqrt{R}\; e^{i\xi} \quad \text{where } \xi = -\alpha_0\, \ell n \sin^2 \frac{\theta_{CM}}{2}$$
$$\alpha_0 = Z_0 Z_1 e^2/\hbar v \qquad (58)$$

and R is the Coulomb scattering cross-section given by equation 32.

As an example of the detailed calculation of the amplitude matrix, the term corresponding to the process of s-waves combining with the incident channel spin configuration (2, 2) to form a $J_B = 2$ state in the compound nucleus that then decays by d-wave emission through the resultant channel spin state (2, 2) will be calculated. From the conservation of the z-component of angular momentum it follows that $m_B = 2$ and $m'_\ell = 0$. The Clebsch-Gordon coefficient for the formation of the compound nuclear state (2, 2) from the channel spin and orbital angular momentum configurations (2, 2) and (0, 0) is 1. The Clebsch-Gordon coefficient corresponding to the decay of this state into configurations (2, 2) and (2, 0) is $\sqrt{1/14}$. The angular dependence associated with the outgoing orbital angular momentum wave being Y_2^o, the full amplitude for the above process is then $\sqrt{1/14}\ Y_2^o\ f^2_{2,2,s,d}$.

In general the term $f^{J_B}_{J_{ch}, J'_{ch}, \ell, \ell'}$ is given by

$$f^{J_B}_{J_{ch}, J'_{ch}, \ell, \ell'} = \frac{\sqrt{4\pi}\, i}{2k}\ i^{(\ell-\ell')}(2\ell+1)^{\frac{1}{2}} e^{i(\eta_\ell+\eta'_\ell-2\eta_o)} f_{sc} \tag{59}$$

where, $$e^{i(\eta_\ell-\eta_o)} = \frac{(1+ia_o)\ldots(\ell+ia_o)}{(1+a_o^2)^{\frac{1}{2}}\ldots(\ell^2+a_o^2)^{\frac{1}{2}}}$$

The scattering amplitude, f_{sc}, is related to the phase shifts and partial widths in a way that will be developed. The remaining terms in the above definition arise from the conversion of a probability amplitude into the square root of a cross-section and the expansion of the incident plane and resultant spherical waves in terms of Coulomb wave functions and Legendre polynomials.

(b) Discussion of the scattering amplitude f_{sc}

It remains only to determine the value of the scattering amplitude f_{sc} in order to obtain the theoretical cross-section for s-wave, p-wave, or d-wave formation and decay of a compound nuclear state of spin 1^-, 2^-, 0^+, or 2^+, in B^{10}, by the elastic scattering of protons from Be^9.

Before determining f_{sc}, it is first necessary to make a distinction between the physical and theoretical definitions of elastic scattering. Theoretically, elastic scattering is associated with the re-emission of the incident particle with its orbital angular momentum and channel spin configurations unchanged. Physically, elastic scattered particles are those that interact with the nucleus and emerge without exciting the nucleus. These particles may have their orbital or intrinsic spins reoriented in the process and still be counted since the detection equipment is spin insensitive. While the theoretical equations must account for these particles that undergo spin realignment in scattering, they are considered throughout the theory as being components of the non-elastic or reaction cross-section. It is therefore necessary to distinguish between the scattering amplitudes of the two different types of processes, elastic scattering with and without change of spin orientation. These scattering amplitudes will be referred to as $f_{\underline{\underline{sc}}}$ and $f_{\underline{sc}}$ respectively.

For the general case of true elastic scattering, i.e. no change of spin configurations,

$$f_{\underline{sc}} = S_{p,p} - 1 \tag{60}$$

where $S_{p,p}$ is the proton-proton component of the scattering matrix.

That is, $S_{p,p}$ is the coefficient of the outgoing true elastically scattered spherical proton wave function produced as a result of the interaction of the unit normalized incoming plane proton wave with the target nucleus.(16) In terms of $S_{p,p}$, the total reaction cross-section for the case of spinless particles may be obtained from the requirement of the conservation of particles as

$$\sigma_{\text{Reaction}} = \pi \lambda\!\!\!^{-}{}^2 \left(1 - |S_{p,p}|^2\right) \tag{61}$$

For the simplest case of no reaction cross-section, equation 62 requires $|S_{p,p}|^2 = 1$, hence $S_{p,p}$ may be written

$$S_{p,p} = e^{2i\delta} \tag{62}$$

For the case of no potential scattering, the requirement of a resonance shape in the elastic scattering anomaly determines the energy variation of δ in the simplest case as

$$\cot \delta = \frac{E_R - E}{\Gamma/2} \tag{63}$$

where E_R is the resonance energy of the level, and Γ is its width in energy units. Thus $\underline{f}_{sc} = e^{2i\delta} - 1$ and $\sigma_{\text{Reaction}} = 0$.

The further generalization of $\underline{f}_{sc}$ to the more complicated cases that include resonant and non-resonant reaction cross-sections or potential scattering phase shifts will be accomplished by geometrical rather than mathematical arguments. To proceed in this direction, a scattering amplitude diagram is constructed by plotting $\underline{f}_{sc}$ in the complex plane as in fig. 42A. As the energy E is increased through the resonant region, 2δ increases through 360° in a counterclockwise direction, and $\underline{f_{sc}}$ is represented by a vector whose origin is at the point (1, 0) and whose end traces out the full unit circle.

To include the possibility of a resonant reaction cross-section, $\underline{f_{sc}}$ must be multiplied by the probability amplitudes for formation and break up of the compound nuclear state via the elastic scattering process. Hence

$$\underline{f_{sc}} = (a^{\ell}_{J_B, J_{ch}})^2 \frac{\Gamma_{p\ell}}{\Gamma} (e^{2i\delta} - 1) \tag{64}$$

The channel spin amplitude $a^{\ell}_{J_B, J_{ch}}$ is the nuclear probability amplitude of forming the given J_B from the orbital angular momentum and the channel spin J_{ch}, and is related to the method of nuclear coupling of the intrinsic angular momenta of the target and bombarding particle with their relative orbital angular momentum. From its definition it follows that

$$a^{\ell}_{J_B, J_{ch}} = 0 \qquad \text{unless} \qquad \vec{J}_B = \vec{J}_{ch} + \vec{\ell}$$

and (65)

$$(a^{\ell}_{J_B, 1})^2 + (a^{\ell}_{J_B, 2})^2 = 1$$

From the scattering amplitude diagram of fig. 42B, it is seen that the scattering amplitude now traces out a circle of radius

$$(a^{\ell}_{J_B, J_{ch}})^2 \frac{\Gamma_{p\ell}}{\Gamma}$$

in the complex plane, as the phase shift goes through resonance. The proton-proton component of the scattering matrix is now given by

$$S_{p,p} = (a^{\ell}_{J_B, J_{ch}})^2 \; \frac{\Gamma_{p\ell}}{\Gamma} \; (e^{2i\delta} - 1) + 1 \qquad (66)$$

Hence

$$\sigma_{\text{Reaction}} = 4\pi\lambda\!\!\!^{-}{}^2 (a^{\ell}_{J_B, J_{ch}})^2 \; \frac{\Gamma_{p\ell}}{\Gamma} \; \frac{\Gamma_R}{\Gamma} \; \sin^2\delta \qquad (67)$$

where $\Gamma_R = \Gamma - (a^{\ell}_{J_B, J_{ch}})^2 \, \Gamma_{p\ell}$. This is the well known Breit-Wigner one level formula.

The most general case for $f_{\underline{sc}}$, illustrated in fig. 42C, occurs when the center of the resonance circle is removed from the real axis by an angular amount 2ϕ, and from tangency with the unit circle by the amount C, with the entire resonance circle lying on or within the unit circle as is required by the conservation of particles. In this case,

$$f_{\underline{sc}} = e^{2i\phi} \; (a^{\ell}_{J_B, J_{ch}})^2 \; \frac{\Gamma_{p\ell}}{\Gamma} \; (e^{2i\delta} - 1) + (1 - C)e^{2i\phi} - 1 \qquad (68)$$

and

$$\sigma_{\text{Reaction}} = \pi\lambda\!\!\!^{-}{}^2 C(2-C) + 4\pi\lambda\!\!\!^{-}{}^2 (a^{\ell}_{J_B, J_{ch}})^2 \; \frac{\Gamma_{p\ell}}{\Gamma} \left[\frac{\Gamma_R}{\Gamma} - C \right] \sin^2\delta$$

(69)

It is seen that 2ϕ represents an elastic scattering potential phase shift since its presence affects only $f_{\underline{sc}}$, hence the elastic scattering, but not the reaction cross-section. The quantity C represents a non-resonant contribution to the reaction cross-section that occurs through the same spin configurations as the resonant contribution. It should be noted that in this case of a non-resonant reaction occurring through the same spin configurations as the resonant reaction, partial decay widths cannot be obtained from the reaction cross-section in the usual way, because of the presence of the C in the resonant reaction cross-section. In fact, under the extreme case of $\frac{\Gamma_R}{\Gamma} = C$, the resonance reaction cross-section disappears entirely.

For reasons of later comparisons between experiment and theory, it must be pointed out that what has been drawn as and called resonance circles above are not expected to be circles in the actual case, but rather to be elliptical in nature. The reasons for this effect are two-fold.

First, the radius of the resonance circle is proportional to $\frac{\Gamma_{p\ell}}{\Gamma}$, which for $Be^9(p,p)$ in the energy region under consideration is a monotonically increasing function of the proton energy. Thus, a stretching of the resonance circle into an elliptical shape is expected.

Secondly, the potential phase shift increases monotonically with proton energy, being proportional to the square root of this energy for the case of hard sphere s-wave potential scattering. Such an energy dependence tends to rotate the center of the resonance circle clockwise while the scattering amplitude traces out the circle. This results in an elliptically-shaped rotation.

Having derived expressions for the true elastic scattering amplitude $f_{\underline{sc}}$, it is next necessary to deduce expressions for the scattering amplitude $f_{\underline{\underline{sc}}}$ corresponding to physical elastic scattering accompanied by a change of either the orbital angular momentum or channel spin configurations or both. Since the cross-section for any of these processes is proportional to the square of the appropriate scattering matrix element, it follows that $\underline{\underline{f_{sc}}}$ is just the appropriate scattering matrix element.

To derive $\underline{\underline{f_{sc}}}$, the double requirement that the scattering matrix be unitary and that the resulting scattering matrix elements yield the proper Breit-Wigner resonance energy dependences, is invoked. By inspection it is seen that the $\underline{\underline{f_{sc}}}$ satisfying the above double requirement for the case of no non-resonant reaction cross-section, hence C = 0, is

$$\underline{\underline{f_{sc}}} = e^{2i\phi_{\ell\ell'}} \frac{(\Gamma_{p\ell}\Gamma_{p\ell'})^{\frac{1}{2}}}{\Gamma} a^{\ell}_{J_B, J_{ch}} a^{\ell'}_{J_B, J'_{ch}} (e^{2i\delta} - 1) \qquad (68a)$$

For the case $C \neq 0$:

$$\underline{\underline{f_{sc}}} = a\,(e^{2i\delta} - 1) + b \qquad (68b)$$

where a and b are complicated functions of the channel spin amplitudes, partial widths, and C, obtained from the condition of unitarity of the scattering matrix.

This requirement does not place any restriction on the potential scattering phase shift $\phi_{\ell\ell'}$ of equation 68a. However other general considerations show that $\phi_{\ell\ell'}$ is equal to the pure elastic scattering potential phase shift ϕ of equation 68.$^{(26)}$

It is noted that in the special case of no non-resonant reaction cross-section or potential scattering, the forms of $\underline{f_{sc}}$ and $\underline{\underline{f_{sc}}}$ become identical. It is further noted that this entire development is applicable to the calculation of physical reaction cross-sections if the scattering amplitude $\underline{\underline{f_{sc}}}$ (which is a reaction amplitude from the point of view of the theory) represents the physical reaction amplitude and if the following changes are made:

1. The Coulomb amplitude, f_c, must be removed from the amplitude matrix.
2. While $(\eta'_\ell - \eta'_o)$ retains the same functional form as $(\eta_\ell - \eta_o)$, it must be remembered that the numerical values of these quantities will differ.
3. The partial width $\Gamma'_{p\ell}$ of the outgoing proton must be replaced by the partial width Γ'_R of the outgoing reaction product.

(c) The completed theoretical cross-section equations

A completed theoretical cross-section equation is obtained by choosing the desired form of f_{sc}, inserting it in the amplitude matrix, squaring each element, and averaging over initial while summing over final channel spin configurations.

To allow for the possibilities of potential scattering and non-resonant reactions in the pure s-wave formation and decay of the compound nucleus, the s-wave scattering amplitudes are given the general form

$$\underline{f_{sc}}(J_B) = f_{J_B} + i\, g_{J_B} - 1 \qquad (70)$$

The p-wave and d-wave scattering amplitudes are assumed to contain no non-resonance reactions or potential scattering. Hence, for p-wave or d-wave formation or decay

$$\underline{f_{sc}} = \underline{\underline{f_{sc}}} = \alpha^{\ell}_{J_B, J_{ch}} \alpha^{\ell'}_{J_B, J'_{ch}} \frac{(\Gamma_{p\ell}\Gamma'_{p\ell})^{\frac{1}{2}}}{\Gamma} (e^{2i\delta} - 1) \qquad (71)$$

With these choices of scattering amplitudes, the following theoretical cross-section equations may be calculated:

(i) pure s-wave scattering

$$\frac{d\sigma/d\Omega}{d\sigma_R/d\Omega} - 1 = \left[\frac{\sin\xi}{k\sqrt{R}} - \frac{1}{2k^2 R}\right](X-1) - \frac{\cos\xi}{k\sqrt{R}}\,Y - \frac{U}{4k^2 R} \tag{72}$$

where

$$X = \frac{3}{8} f_1 + \frac{5}{8} f_2 = \sum_{J=1}^{2} \frac{(2J+1)}{8}\Big\{\cos 2\phi_J [1 - C_J - 2\frac{\Gamma_{p_J}}{\Gamma_J}\sin^2\delta_J] - \frac{2\Gamma_{p_J}}{\Gamma_J}\sin 2\phi_J \sin\delta_J \cos\delta_J\Big\}$$

$$Y = \frac{3}{8} g_1 + \frac{5}{8} g_2 = \sum_{J=1}^{2} \frac{(2J+1)}{8}\Big\{\sin 2\phi_J [1 - C_J - 2\frac{\Gamma_{p_J}}{\Gamma_J}\sin^2\delta_J] + \frac{2\Gamma_{p_J}}{\Gamma_J}\cos 2\phi_J \sin\delta_J \cos\delta_J\Big\}$$

$$U = 1 - \frac{3}{8}(f_1^2 + g_1^2) - \frac{5}{8}(f_2^2 + g_2^2) = 1 - 3/8\,|S_{p,p}|^2_{J=1} - 5/8\,|S_{p,p}|^2_{J=2}$$

$$= \frac{\sigma_{\text{Reaction}}}{\pi\lambda\!\!\!^{-}{}^2}$$

$d\sigma_R/d\Omega = R$ [see equation 32]

$$\xi = -a_o \ln \sin^2 \frac{\theta_{CM}}{2} \qquad a_o = \frac{Z_o Z_1 e^2}{\hbar v}$$

(ii) pure s-wave scattering mixed with d-wave formation and decay of a $J_B = 2^-$ state

$$\frac{d\sigma/d}{d\sigma_R/d} - 1 = \text{pure s-wave terms} - \frac{\sqrt{5\pi}}{4k\sqrt{R}}\, Y_2^o \frac{\Gamma_{p_d}}{\Gamma}[A_2\cos\xi - B_2\sin\xi]$$

$$+ \frac{\sqrt{5\pi}}{8k^2 R}\, Y_2^o \frac{\Gamma_{p_d}}{\Gamma}\Big\{A_2[g_1(1-a_2^2) + g_2 a_2^2] + B_2[(1-a_2^2)(f_1-1) + a_2^2(f_2-1)]$$

$$
\begin{aligned}
&+ 4 \frac{\Gamma_{p_s}}{\Gamma} a_2^2 \sin^2 \delta_2 \Big\} + \sqrt{\frac{5}{14}}\, \frac{5}{128} \frac{\Gamma_{p_d}}{\Gamma^2} (\Gamma_{p_d} \Gamma_{p_s})^{\frac{1}{2}} a_2 [\tfrac{10}{7} a_2^2 - 1] \\
&\qquad \cdot [5 - 42 \mu^2 + 45 \mu^4] [A_1 A_2 + B_1 B_2] \\
&+ \frac{1}{k^2 R} \left(\frac{\Gamma_{p_d}}{\Gamma} \right)^2 \sin^2 \delta_2 \Big\{ (.8464 - 1.9531 \mu^2 + 2.1484 \mu^4) \qquad (73) \\
&\qquad - a_2^2 (.8557 - 4.2411 \mu^2 + 2.7902 \mu^4) \\
&+ a_2^4 (.6112 - 3.0293 \mu^2 + 1.9930 \mu^4) \Big\} + \frac{5}{64} (7 - 6 \mu^2 + 15 \mu^4) \frac{\Gamma_{p_d}}{\Gamma} \frac{\Gamma_{p_s}}{\Gamma} \frac{\sin^2 \delta_2}{k^2 R}
\end{aligned}
$$

where

$A_1 = 2 \sin \delta_2 \cos (\delta_2 + \eta_2)$

$B_1 = -2 \sin \delta_2 \sin (\delta_2 + \eta_2)$

$A_2 = 2 \sin \delta_2 \cos (\delta_2 + 2\eta_2)$

$B_2 = -2 \sin \delta_2 \sin (\delta_2 + 2\eta_2)$

$$e^{i\eta_2} = \frac{(1 + i a_o)(2 + i a_o)}{(1 + a_o^2)^{\frac{1}{2}} (2 + a_o^2)^{\frac{1}{2}}}$$

δ_2 = resonant phase shift for $J_B = 2$

a_2 = channel spin amplitude for formation of a $J_B = 2$ state by d-waves and channel spin 2

Γ_{p_d} = d-wave proton width

Γ_{p_s} = s-wave proton width

$\mu = \cos \theta_{CM}$

(iii) pure s-wave scattering mixed with p-wave formation and decay of a $J_B = 2^+$ state through channel spin 1

$$\frac{d\sigma/d\Omega}{d\sigma_R/d\Omega} - 1 = \text{s-wave terms} - 5/8\,\frac{\mu}{k\sqrt{R}}\,\alpha_1^2\,\frac{\Gamma_{p_2}}{\Gamma_2}\left[A_3\cos\xi - B_3\sin\xi\right]$$

$$+ 5/8\,\frac{\mu}{2k^2R}\,\alpha_1^2\,\frac{\Gamma_{p_2}}{\Gamma_2}\left[g_1A_3 - B_3(1-f_1)\right] + \frac{(13+21\mu^2)}{32k^2R}\left(\alpha_1^2\,\frac{\Gamma_{p_2}}{\Gamma}\right)^2\sin^2\delta_1 \tag{74}$$

where

$A_3 = 2\sin\delta_1\cos(\delta_1 + 2\eta_1)$

$B_3 = -2\sin\delta_1\sin(\delta_1 + 2\eta_1)$

$e^{i\eta_1} = \frac{(1+i\alpha_o)}{(1+\alpha_o^2)^{\frac{1}{2}}}$

Γ_{p_2} = p-wave $J_B = 2^+$ proton width

Γ_2 = p-wave $J_B = 2^+$ total width

δ_1 = p-wave $J_B = 2^+$ resonance phase shift

α_1 = channel spin amplitude for formation of a $J_B = 2$ state by p-waves and channel spin 1 ($\alpha_1^2 = 1$ in the above formula)

(iv) pure s-wave scattering mixed with p-wave formation and decay of states with $J_B = 2^+$ and $J_B = 0^+$

$$\frac{d\sigma/d\Omega}{d\sigma_R/d\Omega} - 1 = \text{s-wave terms} + \text{p-wave } J_B = 2^+ \text{ terms}$$

$$+\sin\delta_o\cos\delta_o\left\{\frac{\mu}{8k^2R}\,\frac{\Gamma_{p_o}}{\Gamma_o}\left[g_1\cos 2\eta_1 + (1-f_1)\sin 2\eta_1\right]\right.$$

$$\left. - \frac{\mu}{4k\sqrt{R}}\,\frac{\Gamma_{p_o}}{\Gamma_o}\left(\cos\xi\cos 2\eta_1 + \sin\xi\,\sin 2\eta_1\right) + \frac{\alpha_1^2}{8k^2R}\,\frac{\Gamma_{p_o}}{\Gamma_o}\,\frac{\Gamma_{p_2}}{\Gamma_2}(3\mu^2 - 1)\sin 2\delta_1\right\}$$

$$+\sin^2\delta_o\Big\{\frac{\mu}{4k\sqrt{R}}\frac{\Gamma_{p_o}}{\Gamma_o}(\cos\xi\sin2\eta_1-\sin\xi\cos2\eta_1)$$
$$-\frac{\mu}{8k^2R}\frac{\Gamma_{p_o}}{\Gamma_o}[g_1\sin2\eta_1-(1-f_1)\cos2\eta_1] \qquad (75)$$
$$+\frac{1}{8k^2R}\left(\frac{\Gamma_{p_o}}{\Gamma_o}\right)^2+\frac{a_1^2}{4k^2R}\frac{\Gamma_{p_o}}{\Gamma_o}\frac{\Gamma_{p_2}}{\Gamma_2}(3\mu^2-1)\sin^2\delta_1\Big\}$$

where

Γ_{p_o} = p-wave $J_B = 0^+$ proton width

Γ_o = p-wave $J_B = 0^+$ total width

δ_o = p-wave $J_B = 0^+$ resonance phase shift

3. Broad level analysis

In broad level analyses, theoretical equations of the above types are applied to fitting experimental angular distributions. Since, within certain limitations that will be discussed later, there is no a priori variation of s-wave potential phase shifts or non-resonance reaction cross-sections with energy, f_1, g_1, f_2, and g_2 are considered unknown parameters whose values are determined by obtaining the best fit to the experimental data. The validity of the analysis then rests on two points:

(1) The degree to which the theoretical equation can be made to fit the experimental angular distributions by varying the fitting parameters f_1, f_2, g_1, and g_2.

(2) The degree to which the energy variation of the fitting parameters approximates a reasonable behavior of potential scattering and compound nucleus level formation.

As has been pointed out, in the neighborhood of a resonance, the scattering amplitude diagram obtained by plotting f versus g or X versus Y is expected to approximate a counterclockwise elliptical motion as the energy is increased. The center of this resonance ellipse is rotated from the real axis through an angle equal to twice the potential phase shift, the deviation from tangency of the unit circle and resonance ellipse is related to the non-resonant reaction-cross-section, and the radius of the ellipse at any energy is proportional to Γ_p/Γ at that energy. A behavior of this type is required of the fitting parameters before a reasonable analysis of the data is assured.

The simplest theoretical elastic scattering equation is obtained from the assumption of s-wave formation and decay of the compound nucleus. Hence, unless there are existing experimental arguments for believing that the states of interest are not formed by s-waves, the simplest analysis is obtained by attempting to fit the experimental angular distributions with the pure s-wave theoretical cross-section equation. This was the first method applied in the analysis of the elastic scattering of protons by beryllium.

The three unknown fitting parameters in the theoretical s-wave equation are required by definition to satisfy the inequalities,

$$X^2 + Y^2 \leq 1 \qquad 0 \leq U \leq 1 \tag{76}$$

Furthermore, U is related to the total s-wave reaction cross-section as in equation 72. Since the detailed fitting of the experimental angular distributions happened to be insensitive to the choice of U, it was estimated from the known reaction cross-section.(17) Pure s-wave fits on all angular distributions were then made with a theoretical equation involving only the two undetermined parameters X and Y. In certain energy regions, the pure s-wave analysis failed to meet the above double requirement on the validity of the analysis procedure. In these regions, others of the previously written theoretical cross-section equations were used in attempting to obtain a fit of the data. These procedures will be covered more thoroughly in later discussions of the properties of the states in B^{10} as determined from the theoretical analysis of $Be^9(p, p)$.

4. Narrow level analysis

The general philosophy involved in analyzing narrow resonances is to run excitation curves in the neighborhood of the resonance at a series of angles corresponding to zeroes of Legendre polynomials. It is seen from the amplitude matrix (fig. 41) that Coulomb and s-wave amplitudes appear only in the diagonal elements, and that the angular dependent terms in the diagonal elements are of the form Y_ℓ^0. If the background is composed of at most s-wave and Coulomb amplitudes, the interference terms between this background and the narrow resonance can therefore contain only the angular dependence $P_\ell^0 (\cos \theta)$. Thus, the determination of the angle at which interference effects disappear is enough to yield the orbital angular momentum of the proton forming the state. Furthermore, the magnitude of the anomaly at this angle is simply related to the J-value of the state of interest, and the J-value can thus be estimated with some degree of accuracy if $\frac{\Gamma_p}{\Gamma}$ is known.

A more complete and definitive analysis involves explaining the magnitude of the resonance anomaly at angles other than that at which the interference terms disappear. To carry out this procedure on the narrow 1084 kev resonance, the following procedure was adopted.

The most general theoretical cross-section equation may be written in the form

$$\frac{d\sigma/d\Omega}{d\sigma_R/d\Omega} = \text{slowly varying background terms} + A(E,\theta)\sin\delta\cos\delta + S(E,\theta)\sin^2\delta \qquad (77)$$

where δ is the resonance phase shift, and $A(E,\theta)$ and $S(E,\theta)$ are two theoretically calculable functions of energy and angle, whose energy variations are assumed small compared to the energy variation of δ in order that the narrow resonance type of analysis be applicable.

The first step in the complete narrow level analysis is to fit the experimental excitation curves with an equation of the above form, choosing $S(E,\theta)$ and $A(E,\theta)$ to obtain the best fits, and calculating δ from equation 64. The angular variations of the $S(E,\theta)$ and $A(E,\theta)$ thus determined are then compared with theoretically calculated values based on different assumptions of background,

ℓ, ℓ' and J_B. The best agreement between these theoretically and experimentally determined quantities may then lead to definite statements on the spins and parities of the state of interest.

The above analysis procedure has obvious advantages over other plausible procedures for two reasons. First, experimental errors due to resolution or incident beam energy variation with scattering angle due to stray magnetic field variations are eliminated before the theoretical analysis is attempted. This is accomplished by requiring the best possible fit at all angles using only one resonant energy and total width for the state. Secondly, information on the resonance energy and width of the state is obtained by a straightforward procedure assuming only that resonance theory can explain the anomaly of interest. For the 1084 kev resonance the energy and width thus determined are

$E_R \approx 1084$ kev and $\Gamma \approx 3$ kev.

The detailed discussion of the application of the above procedures to the analysis of the narrow 1084 resonance will be carried out in Part 5B of Section IV, below.

5. The states of B^{10}

A summary of the properties of the states of B^{10} in the energy region covered by the present experiment is given in Table 2. The following discussion concerns the methods of theoretical deduction of these properties.

(a) The 330 kev state

The structure of the elastic scattering excitation curves between 200 and 700 kev indicates the presence of a broad

TABLE II. Properties of the States of B^{10} Reached by $Be^9 + p$

Properties Determined from $Be^9(p,p)$			Properties determined from $Be^9(p,d)$:$Be^9(p,\alpha)$:$Be^9(p\gamma)$		
Er (kev)	J, Parity	Widths	Er (kev)	J, Parity	Widths
~330	$1^-, 2^-$	$\frac{\Gamma_p(330)}{\Gamma(330)} \sim \begin{cases} .18 \text{ if } J_B = 2 \\ .30 \text{ if } J_B = 1 \end{cases}$	336	1^-	$\theta_p^2/3 \sim 0.5$ $\theta_d^2/3 \sim 0.4$ $\theta_\alpha^2/3 \sim 0.05$
~980	2^+	$\frac{\Gamma_p}{\Gamma} = 0.9$ $\theta_p^2/3 \sim 0.07$			
~998	2^-	$\frac{\Gamma_p}{\Gamma} = 0.65 \pm .15$ $\Gamma = 150 \pm 50$ kev $\theta_p^2/3 \sim 0.02$	993	2^-	$\Gamma = 88$ kev $\Gamma_\gamma = 23$ ev
1084 ± 2	0^+	$\Gamma = 3$ kev	1085 ± 2	0	$\Gamma_\gamma = 6.0$ ev
~1330	2^-	$\frac{\Gamma_p}{\Gamma} = 0.65 \pm .15$ $\Gamma = 400 \pm 100$ kev $\theta_p^2/3 \sim 0.05$			

resonance anomaly near 330 kev. From its large width and the presence of an interference anomaly at all angles of observation, the compound nuclear state appears to be formed by s-waves. Thus, the first procedure involved in the low energy analysis was to attempt to fit the appropriate angular distributions by a pure s-wave theoretical cross-section equation. Results of this procedure are shown in figs. 14 through 20. In these figures the 7°/o error indicated on the 110 degree data serves to orient the eye to the accuracy within which the theoretical expressions approximate the experimental data.

In the region between 220 and 776 kev the pure s-wave theoretical equation is seen to agree with the experimental data to within experimental error. Thus, the only remaining requirement on a valid analysis in this region is that the fitting parameters X and Y determined in the above analysis procedure exhibit the proper resonance behavior expected of an s-wave state. The plot of X versus Y is included in the scattering amplitude diagram of fig. 43.

It is seen that the plot of the fitting parameters does exhibit a counterclockwise elliptical rotation with increasing energy in this energy region. That this is the expected energy variation associated with a resonance is seen by recalling Part 2B of Section IV in which it is pointed out that the presence of a resonance requires an elliptical rotation of the resonant scattering amplitude plotted in the complex plane, and that this rotation is confined to the interior of the unit circle with its exact location yielding information on the potential phase shift and the non-resonant reaction cross-section.

Thus, the double requirement of obtaining good fits to the experimental data and of the fitting parameters exhibiting a proper energy variation is satisfied, and it remains only to determine the properties of the 330 kev state from the scattering amplitude diagram in order to complete the analysis in this energy region. Before carrying out this procedure, it should be mentioned that the isotropy of the deuteron and alpha particle angular distributions at 333 kev (figs. 30 and 31) is in agreement with the elastic scattering conclusion of an s-wave state.

From the tangency of the resonance ellipse and unit circle in the scattering amplitude diagram, the quantity C of equation 69 is zero, and there is no non-resonant reaction cross-section in the s-wave channels at the lowest energies. From the fact that the center of the resonance circle is near the real axis, the potential scattering phase shift is nearly zero. Both of these effects are to be expected at sufficiently low energies.

Under the assumptions that the potential and non-resonant phase shifts are constant over the region of the resonance, it is seen from equation 72 that the radius of the resonance ellipse is given by $\omega \frac{\Gamma_p}{\Gamma}$, where

$$\omega = \begin{cases} 3/8 \text{ for } J_B = 1 \\ 5/8 \text{ for } J_B = 2 \end{cases} \qquad (78)$$

Since the radius and $\frac{\Gamma_p}{\Gamma}$ vary with energy because of barrier penetration, it is required in discussing partial or total widths to specify the energy to which these quantities refer. From the radius of the resonance ellipse at 330 kev the partial proton width at that energy is given by

$$\frac{\Gamma_p}{\Gamma} = \begin{cases} .18 \text{ if } J_B = 2 \\ .30 \text{ if } J_B = 1 \end{cases} \tag{78a}$$

It must be emphasized that these values of partial proton width are accurate to about only a factor of two. This arises from the fact that the theoretical equations yield values for $\frac{d\sigma/d\Omega}{d\sigma_R/d\Omega} - 1$, which in the energy region under consideration is a number of the order of 0.1. A five percent decrease in cross-section halves this number and thereby changes the fitting parameters and the radius of the resonance ellipse considerably.

The total width of the 330 kev state may be determined from detailed fitting of the low energy region of the amplitude diagram by assuming that the non-resonant phase shift remains zero over the region of the resonance, the potential phase shifts possess an energy variation proportional to the square root of the energy, and the resonant phase shift is given by$^{(18)}$

$$\cot \delta = \frac{E_\lambda + \Delta_\lambda(E) - E}{\Gamma_\lambda/2} \tag{79}$$

where

$$\Delta_\lambda(E) = \sum_{s\ell} \Delta_{\lambda s\ell}(E) \qquad \Delta_{\lambda s\ell}(E) = -\gamma_{\lambda s\ell}\left[g_{s\ell}(E) + \ell\right]$$

$$g_{s\ell} = \left[d \ln \left(F_{s\ell}^2 + G_{s\ell}^2\right)^{\frac{1}{2}} / d \ln x\right]_{x=kR}$$

$F_{s\ell}$ is the regular solution of the Coulomb wave equation, $G_{s\ell}$, the irregular solution, and Γ_λ is the total width of the λ-th resonance. E_λ is its true energy, related to the measured resonance energy E_R and the level shift $\Delta_\lambda(E)$ by

$$E_\lambda + \Delta_\lambda (E_R) = E_R \tag{80}$$

The usual approximation (applied in equation 64) that $\Delta_\lambda(E)$ is constant over the region of a broad resonance is probably poorer than the basic assumption of resonance theory that the logarithmic derivative with respect to energy of the wave function at the nuclear surface is at most a linear function of energy. Thus, it is necessary to calculate $\Delta_\lambda(E)$ as a function of energy before determining the total width of the state. However, the determination of $\Delta_\lambda(E)$ involves knowledge of $\gamma_{\lambda s\ell}$, the reduced width for the emission of the s-th particle with orbital angular momentum ℓ. Since this information cannot be obtained by elastic scattering, recourse must be made to the known reaction cross-sections in order to determine the total width of the state.

The one level formula for the total reaction cross-section may be written$^{(18)}$

$$\sigma_{\text{Reaction}} = \pi \lambdabar^2 \omega \frac{\Gamma_p \Gamma_s}{(E_\lambda + \Delta_\lambda(E) - E)^2 + \Gamma^2/4} \tag{81}$$

where Γ_s is the partial width for the emergent particle, in the present case an alpha or a deuteron. The total width is the sum of the partial widths and any partial width is given in the center-of-mass system by

$$\Gamma_s = 2\,k\,R\,P_\ell \left(\frac{df}{dE}\right)_s^{-1} \tag{82}$$

where

$$f = R \left[\frac{dU/dr}{U}\right]_{r=R}$$

$$P_\ell = \text{penetration factor} = \frac{1}{F^2(R)+G^2(R)}$$

and $U(r)/r$ is the radial part of the nuclear wave function for $r > R$. Writing

$$\left(\frac{df}{dE}\right)^{-1} = \gamma_{\lambda s \ell} = \theta^2_{\lambda s}\,\frac{\hbar^2}{2\mu R^2} \tag{83}$$

where μ = the reduced mass of the system

$$\theta^2_{\lambda s} = R\,|U(R)|^2 \Big/ \int_\tau |\phi|^2\,d\tau$$

ϕ = complete nuclear wave function for $r < R$

one obtains after simplification,

$$\theta^2_{\lambda s} = .110\,A_{red}\,R\,\frac{\Gamma_{s_L}}{P_\ell\sqrt{E}} \times 10^{13} \tag{84}$$

and

$$\gamma_{\lambda s \ell} = 2.277\,\frac{\Gamma_{s_L}}{P_\ell\sqrt{E}}\,\frac{10^{-13}}{R} \tag{85}$$

where R = nuclear radius in centimeters

Γ_{s_L} = s-th partial width in the lab system in mev

E = incident particle energy in the lab system, in mev.

The discussion of partial widths is usually carried out by comparison of the experimentally determined $\theta^2_{\lambda s}$ to the theoretical upper limit of 3 obtained in the single particle limit. It is this ratio that will be referred to as the fraction of the single particle limit.

The one level formula may be solved for $\frac{\Gamma_p}{\Gamma}$ at the resonant energy E_R to give

$$\Gamma_p/\Gamma = \tfrac{1}{2} \pm \tfrac{1}{2}\sqrt{1-\sigma_{\mathrm{Reaction}}/\pi\lambda\!\!\!^{-2}} \tag{86}$$

where $\sigma_{\mathrm{Reaction}}$ is the sum of the s-wave resonant deuteron and alpha reaction cross-sections at 330 kev. Assuming all of the reaction cross-section arises from the 330 kev resonance, $\sigma_{\mathrm{Reaction}}$ may be obtained from figs. 30 and 31. Equation 86 then yields

$$\Gamma_p/\Gamma = .33 \text{ or } .67 \text{ at } E_1 = 330 \text{ kev} \tag{87}$$

if $J_B = 1$ is the assumed spin of the state, as gamma ray data seems to indicate.(19) The choice $\Gamma_p/\Gamma = .33$ is more consistent with the radius of the resonance circle in the scattering amplitude diagram. With this choice, the one level formula yields

$$\Gamma_a/\Gamma = .29; \quad \Gamma_d/\Gamma = .38 \tag{88}$$

at 330 kev. It remains only to determine Γ from a detailed fitting of the one level formula over a range of energies in order to evaluate the various partial widths of the state of interest. To accomplish this, total reaction cross-section data is obtained from the assumption of the angular isotropy of particle emission required of an s-wave resonance, and from the data of Thomas, Rubin, Fowler and Lauritsen,(11) increased by 8°/o to agree with the determination of the cross-sections at 333 kev given in figs. 30 and 31. Penetration factors are calculated from Christy and Latter,(20) and the level shift $\Delta_\lambda(E)$ is obtained from the tables of Coulomb wave functions given by Breit, et al.(21) A plot of $\Delta_\lambda(E)$ as a function of energy for a particular set of reduced partial widths is given in fig. 44.

The conclusion reached from the detailed fitting of the reaction cross-section data by the one level formula is that no total width less than the single particle limit will yield the correct cross-sections at resonance and the large contribution above resonance indicated by the data of Thomas, Rubin, Fowler and Lauritsen.(11) Thus, a background reaction cross-section presumably exists in other than the s-wave channels, since the scattering amplitude diagram resonance ellipse is tangent to the unit circle. The determination of the total and partial widths being dependent on the nature and amount of this background, it is impossible without further detailed investigations in this energy region to determine partial widths for the 330 kev state.

However, some general conclusions do follow from the gross features of the reaction cross-section curves. The total width and the reduced partial widths of the 330 kev state must be quite large. The best fit of the one level formula to the experimental data with a particular choice of background subtraction is obtained for a proton reduced width that is about 50°/o of the single particle limit of 5.7 mev, a deuteron reduced width that is about 40°/o of the single particle limit of 1.9 mev, and a reduced alpha width of about 5°/o of the single particle limit of 1.7 mev. Various methods of background subtraction can vary these values by factors as large as two or three, but it must generally be true that very large proton and deuteron reduced widths and a somewhat smaller alpha reduced width are required to explain the experimental data.

The clarification of the situation around 330 kev requires more complete experimental determinations of angular distributions of the reaction products in order to determine the nature of the background and its relation to the anomaly near 470 kev first observed by Thomas et al,(11) and verified during the course of the present experiment, as shown in fig. 32. The inclusion of pick-up amplitudes in the construction of the reaction cross-section and/or the inclusion of a second resonance with presumably a small proton width may be required to explain the experimental data.

(2) The states in B^{10} between proton energies of 776 and 1664 kev

The first step in the analysis of the angular distributions between 776 and 1664 kev was to attempt a fitting by the pure s-wave theoretical cross-section equation in the manner previously indicated. Results of this fitting procedure are shown in figs. 21 through 28, where the 7% error on the 110° data at all energies again serves to orient the eye to the accuracy with which the theoretical equation fits the experimental data.

The discrepancy between the theoretical fits and the experimental data being greater than the probable error of the experimental determinations at many angles in the majority of the angular distributions, the validity of the pure s-wave analysis was highly suspect. Further doubt was cast on this validity near one mev when one considered the scattering amplitude diagram plot of the fitting parameters X and Y obtained in the analysis procedure (See fig. 43).

Near one mev, the amplitude diagram plot of X versus Y exhibited the hint of a resonance circle, but there were not enough angular distributions in this region to establish its existence or non-existence. Recourse was thus made to the excitation curves at three angles which supply enough information to determine roughly X and Y as a function of energy.

It was found that between 900 kev and 1 mev the pure s-wave theoretical equation provided extremely poor fits to the excitation curves. Furthermore, the fitting parameters tended to make a clockwise circle in the amplitude diagram, a behavior that is nonsensical from the point of view of resonance theory.

The experimental reason for the above behavior is that in the excitation curves, the increase in $\frac{d\sigma/d\Omega}{d\sigma_R/d\Omega}$ corresponding to the anomaly near one mev comes at a lower energy at the forward angles than at the back angles. Thus, over a region of energies, the angular distribution of $\frac{d\sigma/d\Omega}{d\sigma_R/d\Omega}$ is peaked in the forward direction, a behavior difficult to explain with a pure s-wave theoretical equation. Since this equation can satisfy neither of the two requirements on a valid theoretical analysis, the situation near one mev was investigated more thoroughly.

Because the excitation curves near one mev exhibit interference minima at all angles of observation, it seemed desirable to retain the assumption that the one mev state is formed predominantly by s-waves. A hint of a possible modification of the pure s-wave equation was supplied by the ground state gamma ray transition angular distribution which is of the form $1+(.10\pm.03)\sin^2\theta$.(22) This non-isotropy is explainable by the assumption of a small contribution to the formation of the state by d-wave protons. And thus, a second attempt at analysis of the angular distributions was made by allowing for d-wave formation and decay of the compound state in the theoretical cross-section equation. For such a possibility, if the compound state has $J_B = 2^-$, the appropriate theoretical cross-section is given by equation 73.

This theoretical cross-section equation has as unknowns f_1, g_1, f_2, g_2, $\frac{\Gamma_{p_s}}{\Gamma}$, $\frac{\Gamma_{p_d}}{\Gamma}$, and a_2, where Γ_{p_s} is the width for s-wave protons, Γ_{p_d} is the width for d-wave protons, and a_2 is the probability amplitude of formation or decay of the compound nuclear state through channel spin two if the interaction occurs with a d-wave proton. Since the theoretical equation now contains seven unknowns, a unique analysis of the experimental data was nearly impossible. However, qualitative consideration of the theoretical equation was enough to show that the inclusion of d-wave protons does not improve the fitting of the experimental data for any set of assumptions on the seven unknowns.

The only appreciable contribution of the d-wave terms can be shown by calculation to come at large scattering angles, where it tends to increase the theoretical cross-section calculated from the pure s-wave equation. This behavior, illustrated in fig. 45 for a particular set of assumptions on the unknown parameters, tends to decrease the existing agreement between theory and experiment. Thus, the theoretical analysis near one mev was not aided by the addition of d-waves, so it became necessary to look to sources other than the gamma ray angular distribution data for clues to assumptions that would enable a fit of this data. A source of such a clue was obtained from a study of the narrow 1084 kev level, since the analysis in this region is sensitive to the assumed background which arises in part from the one mev broad level.

The gross features of the thin target excitation curves near 1084 kev illustrated in figs. 33 and 34 supply some insight into the spin and parity of the compound nuclear state. Under the experimentally verified assumption that $\Gamma_p / \Gamma = 1$, the smallness of the anomaly at the forward angles is consistent only with a $J_B = 0$ state in B^{10}, since the magnitude of the anomaly increases with J_B. The determination of the parity of the state rests on the magnitudes of the interference terms at the zeroes of $P_1(\cos \theta)$ and $P_2(\cos\theta)$. At 90° there is practically no interference as is seen by the symmetry of the anomaly about the resonance energy, while at 125°16', the resonance anomaly is composed almost entirely of interference terms. While such a behavior may not be inconsistent with d-wave formation of the compound state if one assumes the background to be composed in a large measure of other than s-wave amplitudes, the simplest assumption is that the 1084 state is formed by p-waves, hence $J_B = 0^+$.

With the assumptions that $J_B = 0^+$, that there is no potential scattering or non-resonance reaction cross-section in the p-wave channels, and that only s-wave amplitudes are present in the background, the theoretical fits illustrated in figs. 33 and 34 are obtained. Since these assumptions are not sufficient to explain the anomaly at the back angle, additional amplitudes must be introduced into the theoretical equation.

As has been pointed out, $J_B = 0^+$ is the simplest assumption that will yield reasonable agreement with experiment. The presence of p-wave potential scattering or non-resonance reactions is unlikely in view of the p-wave barrier penetration factor at these energies. Thus, the only reasonable variable in the analysis is the nature of the background that interferes with the narrow 0^+ state.

An obvious extension of the analysis is to include the supposed d-wave present in the formation of the one mev state. However, it is seen from the amplitude matrix of fig. 41 that the 2^- d-wave amplitudes do not interfere with the 0^+ p-wave amplitudes. And thus, some other assumption must be advanced.

A logical approach is to include all p-wave amplitudes in the background, then all d-wave amplitudes, etc., until the background contains enough variables to fit the experimental data. Of the possible p-wave amplitudes, only those leading to a 2^+ state in B^{10} are considered plausible in the background. The reasons for this are that, of the four possible p-wave states, the 1^+ and 3^+ states do not interfere with a 0^+ state. A broad

0^+ state in the background is undesirable for the two reasons that it will not produce the detuerons and alpha particles that must be present in this energy region to account for the cosθ term in the deuteron and alpha angular distributions near one mev(17), and that the inclusion of a broad 0^+ state in the background interfering with the narrow 0^+ state at 1084 kev requires calculations from the two level formula that are extremely difficult if not impossible to make. Thus, a 2^+ p-wave state is inserted in the background. With the assumptions of no potential scattering or non-resonance reaction cross-section from this state, the new parameters $\alpha_1^2 \Gamma_{p_2} / \Gamma_2$ and cot δ_1 are inserted into the analysis, where α_1 is the probability amplitude of the formation of a $J_B = 2^+$ state from p-wave protons through channel spin one, Γ_{p_2} and Γ_2 are respectively the partial proton and total width of the 2^+ state, and δ_1 is its resonance phase. The appropriate theoretical cross-section for a 2^+ state and an arbitrary amount of s-wave interfering with a narrow 0^+ state is given in equation 75.

With this equation, the theoretical fits of the experimental data shown in figs. 33 and 34 are obtained with the following choices of variable parameters:

$$f_1 = -.4, \quad g_1 = -.9, \quad \alpha_1^2 \Gamma_{p_2} / \Gamma_2 = 0.9, \; \cos \delta_1 = -.918.$$

As a further assumption in the following discussions, it is assumed that $\alpha_1^2 = 1$ and $\Gamma_{p_2} / \Gamma_2 = 0.9$, values that are accurate to about 10% if the 1084 kev analysis is correct.

With the above choice of parameters, the only unknown involving the assumed 2^+ state is its resonance energy, if one assumes that δ_1 is given by equation 64. Since cos δ_1 is negative near the narrow level, the resonance energy of the 2^+ state is less than 1084 kev. It cannot, however, be more than a few hundred kev less and still possess a reduced width smaller than the single particle limit. Such a state may be calculated to produce a 90° anomaly symmetric about its resonance energy and of magnitude 0.8 on a ratio-to-Rutherford plot. And thus, a possible conclusion from the 1084 kev narrow level analysis is that a 2^+ p-wave state with a large Γ_p / Γ exists somewhere in the range between about 800 and 1080 kev, and this state produces a sizable anomaly in the elastic scattering of protons by beryllium.

Such a set of conclusions must be tested on the elastic scattering angular distributions and excitation curves in the neighborhood of one mev. The theroetical cross-section formula expressing the presence of a 2^+ p-wave state and an arbitrary amount of s-wave is given in equation 74. With the choice of the resonance energy for the 2^+ state, this equation possesses the four unknowns f_1, g_1, f_2, and g_2, which are related to the real and imaginary parts of the $J_B = 1^-$ and $J_B = 2^-$ s-wave scattering amplitudes. Thus, the presence of a p-wave state breaks up the degeneracy in s-wave amplitudes and detailed fitting enables the determination of the variation of both the $J_B = 2^-$ and $J_B = 1^-$ s-wave scattering amplitudes, rather than a combination of them as was obtained with the pure s-wave equation.

The first step in the analysis procedure is to determine the resonance energy of the assumed 2^+ state. From the 90° excitation curve and the fact that at this angle the 2^+ state produces a symmetric anomaly of magnitude 0.8, it seems clear that its resonance energy must lie near 1 mev. A more accurate determination is achieved through considering all three excitation curves between 900 kev and 1 mev and obtaining the best theoretical fit to the experimental data for reasonable fitting parameters by varying the resonance energy of the 2^+ state. Results of this procedure are shown in fig. 12 for the two assumptions $E_R = 998$ kev and $E_R = 980$ kev. From these results and the reasonableness of the fitting parameters assumed in this analysis, the resonance energy of the 2^+ state is 980 kev to within about 10 kev. The fitting parameters used in this analysis are shown in the scattering amplitude diagram of fig. 43. The width of the 2^+ p-wave state at 980 kev as determined from its resonance energy and cos δ_1 at 1085 kev, neglecting effects of the level shift $\Delta_\lambda(E)$, is 90 kev. This corresponds to a reduced width that is about 7°/o of the single particle limit.

The next step in the analysis is the fitting of the angular distributions between 887 and 1664 kev with the theoretical s-wave and p-wave $J_B = 2^+$ cross-section equation. The results of this process are shown in figs. 21 through 28. At all energies the addition of the p-wave state improves the character of agreement between experiment and theory. It remains only to study the energy variations of the fitting parameters f_1, g_1, f_2, and g_2, defined in equation 70, to determine the validity of the fitting procedure and the properties of the s-wave states thus revealed. The scattering amplitude diagram plots of f_1 versus g_1 and f_2

versus g_2 are shown in fig. 43.

The general behavior of the energy variation of f_2 versus g_2 indicates two counterclockwise resonance circles corresponding to two $J_B = 2^-$ states in B^{10} near energies of 998 kev and 1330 kev. The energy variation of f_1 versus g_1 shows what may be interpreted as the tail of the 330 kev resonance along with a potential phase shift and the hint of what might be a higher energy s-wave $J = 1^-$ resonance that causes the scattering amplitude diagram plot to reverse direction and start in a counterclockwise circle at the higher energies. These behaviors might be expected in view of Lane's prediction of four s-wave states, two $J_B = 1^-$ and two $J_B = 2^-$, in this energy region.(23)

The validity of the fitting procedure being assumed by virtue of its satisfying the double requirement of fitting the data with proper energy-varying fitting parameters, the scattering amplitude diagram must be studied in greater detail to determine the properties of the potential phase shifts in the $J_B = 1^-$ channel and the compound nuclear states in the $J_B = 2^-$ channel.

From a simple model of hard sphere scattering in the absence of a Coulomb potential, Wigner(24) derives the inequality

$$\frac{d\phi}{dk} > -R \tag{89}$$

from the law of causality that the scattered wave cannot emerge before the incident wave enters the scattering region. In this inequality, ϕ is the potential scattering phase shift, k the wave number, and R the radius of the hard sphere. The energy variation of the $J_B = 1^-$ potential phase shift, as revealed in the scattering amplitude diagram of f_1 versus g_1, violates this inequality by about a factor of ten between 887 and 1220 kev. However, it is felt that this violation is not sufficient to cast very strong doubt on the validity of the analysis, for the following reasons.

The theoretical derivation of Wigner's inequality does not include effects of compound nuclear states or of the Coulomb potential and either of these effects might alter the inequality somewhat. A stronger argument involves the theoretical means of determining the variation of the potential phase shift with energy. This variation is determined essentially by the 887 and 1085 kev theoretically deduced phases, since all other phases can be varied over a rather large range without disturbing the theoretical fitting to any great extent. The reasons why the 887 and 1085 kev fitting parameters cannot be varied greatly are that the 1085 kev fit comes from the narrow level analysis which is rather sensitive to f_1 and g_1, and the 887 kev analysis occurs in a region where the elastic scattering cross-section is nearly equal to the Coulomb cross-section. This means that at 887 kev the theoretical $\frac{d\sigma/d\Omega}{d\sigma_R/d\Omega} - 1$ is a small number obtained from differences of large numbers, and the analysis is extremely sensitive to the choice of the fitting parameters. Inclusion of another p-wave amplitude to explain the reaction cross-section angular anisotropy around 800 kev would thus mainly effect the 887 kev analysis without disturbing the other angular distributions greatly. This in turn might move the $J_B = 1^-$ fitting parameters at 887 kev in such a direction as to decrease $-\frac{d\phi}{dk}$ by a large factor. It is for reasons of this nature that the large energy variation of the $J_B = 1^-$ potential phase shift is not considered a detrimental fact on the validity of the s-wave and p-wave $J_B = 2^+$ analysis.

The scattering amplitude diagram plot of f_2 versus g_2 exhibits segments of two counterclockwise circles whose near tangency with the unit circle indicates little or no non-resonance reaction cross-section in the $J_B = 2^-$ s-wave channel. The amount of rotation of the centers of the two circles from the real axis being indefinite but fairly small, there is a lesser amount of potential scattering evidenced in the $J_B = 2^-$ channel than in the $J_B = 1^-$ channel. The resonance energies of the two states, corresponding to rotations through half the resonance circles, are about 998 and 1330 kev respectively. The ratio of proton to total width is given by the radii of the two circles as $\Gamma_p/\Gamma = 0.65 \pm 0.15$ for both states. The total widths of the two states obtained from the low energy side of the 998 kev resonance circle, the high energy side of the 1330 kev resonance circle, and equation 64, are $\Gamma(998) = 150 \pm 50$ kev and $\Gamma(1330) = 400 \pm 100$ kev. The reduced proton widths of the 998 and 1330 kev states are respectively about 2% and 5% of the single particle limit.

Since much information on the states of B^{10} is obtained from the elastic scattering analysis assuming a 2^+ p-wave state at 980 kev, it is interesting to compare the conclusions of this analysis with those obtained from a study of gamma rays and reaction products from the bombardment of protons by beryllium.

Gamma ray transitions to the ground state from the s-wave state near one mev are electric dipole while those from the p-wave state are magnetic dipole. If $\alpha_1^2 = 1$, the p-wave state is formed only by channel spin one and the two types of gamma rays do not interfere. The electric dipole gammas are isotropic while the magnetic dipole gammas follow the angular distribution $1 + 0.167 \sin^2 \theta$ (Appendix 1). Thus, the combination of s-wave and p-wave $J_B = 2$ states near one mev can lead to the observed angular distribution $1 + (.10 \pm .03) \sin^2 \theta$, with appropriate choices of the partial gamma widths.

Additional experimental information has been obtained by Devons(25) from a study of the angular correlation of internal conversion pairs, a study whose theoretical interpretation gives the strength of the various multipole orders involved in the gamma transition. From the bombardment of 50 to 100 kev thick beryllium foils with protons of energies between about 950 and 1050 kev, Devons deduces the existence of a mixed E1, and E3 or M2 transition to the ground state with the E1 gamma width being about 3°/o of that predicted by the single particle model.(16) However, the E3 or M2 width comes out about 10^3 times larger than that predicted by either the single particle or liquid drop models. This theoretically impossible conclusion is obviated under the assumptions of a p-wave 2^+ state at 980 kev and an s-wave 2^- state at 998 kev, since the resultant M1 and E1 transitions to the ground state will lead to roughly the experimental angular correlation of internal conversion pairs for gamma widths within the single particle model limit.(26) The reasons for this conclusion follow from the experimental angular correlation that is peaked at small angles and remains fairly large at larger angles. The property of the theoretical $\Lambda = 1$ (E1 transition) correlation function is that it remains relatively larger at large angles than the $\Lambda = 2$ (M1 or E2 transitions) or $\Lambda = 3$ (M2 or E3) transitions that are peaked more at the smaller angles. With nearly equal contributions of $\Lambda = 1$ and $\Lambda = 3$, Devons fits the experimental data and from the gamma width, $\Gamma_\gamma = 23$ ev, of the state, deduces the large width of the M2 or E3 transition. However, nearly equal amounts of $\Lambda = 1$ and $\Lambda = 2$ provide at least a qualitative fit of the data and give reduced widths that are 3% and 80% of the single particle model limit for the E1 and M1 transitions respectively.

The $Be^9(p,d)$ and $Be^9(p,\alpha)$ experimental determinations below one mev provide much insight into the states of B^{10}. The principal experimental facts are that the total reaction cross-sections are peaked near 940 kev and exhibit angular anisotropies that indicate an interference between states of opposite parity that is large in the region between 500 kev and 1 mev but that peaks somewhat near 750 kev and one mev. These behaviors are qualitatively partially understood in terms of the elastic scattering analysis, but their quantitative theoretical interpretation must depend on more thorough experimental data and analysis.

The qualitative understanding of the total reaction cross-section peaking about 50 kev below the 998 kev proton or gamma ray resonance energy follows from the assumption that the reaction products are produced by the $J_B = 2^-$ level and the realization that there are two overlapping states of the same spin and parity in B^{10}, the 998 and 1330 kev 2^- levels. Under such circumstances it is possible for the total reaction cross-section to peak at an energy different from the true resonance energy. It must be pointed out, however, that such a behavior is not predicted by the scattering amplitude diagram of f_2 versus g_2. The total reaction cross-section is proportional to $\left[1 - |S_{p,p}|^2\right]$ where, in the scattering amplitude diagram, $S_{p,p}$ is the distance from the center of the unit circle to a point on the resonance circle. Thus, the scattering amplitude diagram predicts that the s-wave $J_B = 2^-$ reaction cross-section will peak near one mev.

The peaking of the cosθ term in the reaction angular distributions near one mev is explained by the presence of the 2^+ p-wave state if the assumption that $\alpha_1^2 = 1$ is relaxed somewhat to allow for the formation of this state through channel 2. The state can then interfere with the 2^- s-wave state which is only formed in channel 2.

The interference between states of opposite parity that exists down to 500 kev in the reaction product angular distributions cannot be understood in terms of the states deduced from the elastic scattering experiment. It is plausible that a second p-wave state with a small proton width exists near 700 kev. Such a state might produce a negligible effect in elastic scattering but could cause interference in the reaction product angular distributions. The test of this hypothesis should involve a non-proton induced reaction leading to this energy region in B^{10}. The only choice of a nuclear reaction satisfying these requirements is $Li^6 + \alpha$. A study of the reaction products and elastic scattering produced under alpha bombardment of Li^6 by alphas near 5 mev might lead to a clarification of the theoretical situation of the states of B^{10} near 7.50 mev.

It is seen that the assumption of a 2^+ p-wave state at 980 kev in the proton bombardment of beryllium explains the experimental elastic scattering data quantitatively, the gamma ray data at least semi-quantitatively, and the reaction data qualitatively in part. It is thus of pertinent interest to inquire into some further experimental method of testing the hypothesis of the existence of such a state.

One experimental method involves measurement of the gamma ray angular distribution at a series of energies around one mev, in order to determine the energy variation of the coefficient of the $\sin^2\theta$ term. Since the p-wave barrier penetration factor increases with energy in this energy region much more rapidly than the s-wave penetration factor, the s-wave state might be expected to predominate below the resonance energy, and the p-wave state above. Thus, the coefficient of the $\sin^2\theta$ term in the gamma ray angular distribution will increase with energy and it is this increase that might be experimentally verified. Unfortunately, however, the uncertainty in the experimental determination of the $\sin^2\theta$ coefficient is about the same magnitude as its expected energy variation, so this experiment would not serve as a very decisive test.

A second, more definitive experimental test would be to study the polarization effects produced by the elastic scattering of one mev protons by beryllium in a double scattering experiment. Under the assumptions of only s-wave states and Coulomb scattering, no polarization will be produced, while the presence of a p-wave state in addition to the s-wave states results in a theoretically calculable amount of polarization. And therein lies an experimental test of the hypothesis of a 2^+ state in B^{10}.

One of the more reasonable experimental approaches to this problem involves the elastic scattering of protons by helium as the polarizer and the second scattering from beryllium as the analyzer. Incident protons of energies near 2 mev scattered at angles near 90^o by helium are emitted with a large polarization and the proper energy to interact with beryllium through the states of interest in B^{10}. Rough considerations indicate that with a reasonable geometry several hundred counts might be obtained in a twenty-four hour period.

As a final remark on the possible existence of a 2^+ state in B^{10} it should be noted that in a recent Physical Review article, Kurath(27) applies an intermediate coupling scheme to B^{10} and theoretically deduces the energies of the first five even parities states almost quantitatively. He also predicts the existence of a 2^+ state at almost exactly the same energy as that hypothesized from the theoretical analysis of the elastic scattering of protons by beryllium.

APPENDIX I

CALCULATION OF THE THEORETICAL M1 GAMMA RAY RELATIVE ANGULAR DISTRIBUTION FOR THE TRANSITION FROM A P-WAVE $J_B = 2^+$ EXCITED STATE FORMED ONLY IN CHANNEL ONE TO A 3^+ STATE

The theoretical angular distribution cross-section for the reaction $Be^9+p \longrightarrow B^{10*} \longrightarrow B^{10}+\gamma$ is the absolute square of a summation of amplitudes, each of which corresponds to the interaction through some particular incident channel spin configuration, incident orbital angular momentum, compound nuclear spin configuration, final state spin configuration, and gamma ray total spin and projection. Any amplitude is made of three factors: two Clebsch-Gordon coefficients that represent the probability amplitudes for formation and decay of the compound nucleus; $X_{\ell,m}$, the vector angular dependent part of the magnetic field for electric multipole transitions or the electric field for magnetic multipole transitions; and a group of constants and phase shift dependent terms given by an equation analogous to 59 with the modifications that $\ell'=0$, $(\eta_\ell' - \eta_o) = 0$, and with the addition of a phase shift dependence on the multipolarity of the gamma ray. Since this third factor in any amplitude appears in all amplitudes obtained from a single initial orbital angular momentum, it, along with all other multiplying constants, may be neglected in the derivation of a relative angular distribution, unless one wishes to consider the interference between two different multipole transitions.

Assuming the excited state to have spin $J_B = 2^+$ and to be formed by only p-wave protons through channel spin one, the various relative amplitudes for the gamma transition to the 3^+ ground state in B^{10} are calculated in Table III. In this table, the two columns of Clebsch-Gordon coefficients correspond to the probability amplitudes for formation and decay of the compound state through the listed initial and final spins and projections. The last column gives the relative amplitudes that are needed to calculate a relative angular distribution.

These relative amplitudes interfere incoherently since it is possible, by means of a polarization experiment, to determine the projection of the spin of the emitted gamma ray. Thus, the relative angular distribution is obtained by summing over the absolute squares of the relative amplitudes, obtaining the squares of the vector field quantities from the tables of Kraus.(28) The result of this algebraic process yields the relative angular distribution $[1+(1/6)\sin^2\theta]$ for the M1 transition from a 2^+ state formed only in channel one to the 3^+ ground state of B^{10}.

TABLE III. Relative Amplitudes Involved in the Gamma Ray Transition from a 2^+ State Formed by P-Waves through Channel Spin One to a 3^+ State.

J_{ch}	m_{ch}	ℓ	m_ℓ	J_B	m_B	Clebsch-Gordon Coefficient	J_{GND}	m_{GND}	J_γ	m_γ	Clebsch-Gordon Coefficient	Relative Amplitude
1	1	1	0	2	1	$\sqrt{\frac{1}{2}}$	3	2	1	-1	$\sqrt{\frac{10}{21}}$	$\sqrt{\frac{5}{21}}\ X_{1,-1}$
							3	1	1	0	$-\sqrt{\frac{8}{21}}$	$-\sqrt{\frac{4}{21}}\ X_{1,0}$
							3	0	1	1	$\sqrt{\frac{3}{21}}$	$\sqrt{\frac{3}{42}}\ X_{1,1}$
1	0	1	0	2	0	$\sqrt{\frac{2}{3}}$	3	1	1	-1	$\sqrt{\frac{2}{7}}$	$\sqrt{\frac{4}{21}}\ X_{1,-1}$
							3	0	1	0	$\sqrt{\frac{3}{7}}$	$\sqrt{\frac{6}{21}}\ X_{1,0}$
							3	-1	1	1	$\sqrt{\frac{2}{7}}$	$\sqrt{\frac{4}{21}}\ X_{1,1}$
1	-1	1	0	2	-1	$\sqrt{\frac{1}{2}}$	3	0	1	-1	$\sqrt{\frac{3}{21}}$	$\sqrt{\frac{3}{42}}\ X_{1,-1}$
							3	-1	1	0	$-\sqrt{\frac{8}{21}}$	$-\sqrt{\frac{4}{21}}\ X_{1,0}$
							3	-2	1	1	$\sqrt{\frac{10}{21}}$	$\sqrt{\frac{5}{21}}\ X_{1,1}$

APPENDIX II

SAMPLE CALCULATIONS

(1) Calculation of an elastic scattering differential cross-section from experimental thick target data.

The data to be converted into a differential cross-section is the E_{10} = 1007 kev momentum profile of fig. 5, for which E_{20} = 806 kev. From equation 25

$$(d\sigma/d\Omega)_L = \frac{N_s}{n}\,\frac{ZeR}{2CV\Omega_L}\,\frac{\left[\varepsilon(E_{10})\frac{\partial E_2}{\partial E_1} + \varepsilon(E_{20})\frac{\cos\theta_T}{\cos\theta_T'}\right]}{E_{20}}\,N_R$$

For a pure beryllium target

$$\frac{N_s}{n} = 1$$

From equation 24,

$$R = 292.1$$

Also

$C = .1015 \times 10^{-6}$ farads

$V = 9.30$ volts

$\Omega_L = 3.10 \times 10^{-3}$ steradians

Therefore

$$\frac{ZeR}{2CV\Omega_L} = \frac{1 \times 1.602 \times 10^{-19} \times 292.1}{2 \times .1015 \times 10^{-6} \times 9.30 \times 3.10\times10^{-3}} = 7.996\times10^{-9}/\text{steradians}$$

From fig. 35,

$\varepsilon(E_{10}) = 3.41 \times 10^{-15}$ ev-cm^2 $\qquad$ $\varepsilon(E_{20}) = 3.93 \times 10^{-15}$ ev-cm^2

From equations 19 and 13,

$$\frac{\partial E_2}{\partial E_1} = .81921$$

Thus, for $\theta_T = \theta_T'$

$$\epsilon(E_{10})\frac{\partial E_2}{\partial E_1} + \epsilon(E_{20}) = (3.41 x .8192 + 3.93) \times 10^{-15} = 6.72 x 10^{-15} ev\text{-}cm^2$$

The yield at the peak of the momentum profile of fig. 5 is 4283 counts. The background is 257 counts.

Therefore,

$$N_R = 4026 \text{ counts}$$

Combining the above numbers gives

$$(d\sigma/d\Omega)_L = 7.996 \times 10^{-9}/\text{steradian} \times \frac{6.72x10^{-15} ev\text{-}cm^2}{806 \times 10^3 ev} x 4026$$

$$= .2684 \times 10^{-24} \text{ cm}^2/\text{steradian}$$

$$= .2684 \text{ barns/steradian}$$

This is the differential cross-section for the elastic scattering of protons by beryllium in the laboratory system at a laboratory angle $\theta_L = 83^\circ 35'$. The center-of-mass differential cross-section is

$$d\sigma/d\Omega = \frac{\Omega_L}{\Omega_{CM}} (d\sigma/d\Omega)_L$$

where $\frac{\Omega_L}{\Omega_{CM}}$ is calculated from equations 26 and 27 to be

$$\frac{\Omega_L}{\Omega_{CM}} = .98145$$

Thus,

$$d\sigma/d\Omega = .98145 \times .2684 = .2634 \text{ barns/steradian}$$

The center-of-mass scattering angle, θ_{CM}, is calculated from equation 31 to be

$\theta_{CM} = 90^{\circ}$

The reaction energy to which the above cross-section refers is given by equation 29 as,

$$E_1 = \frac{806 + \frac{3.93}{3.41} \times 1007}{.81921 + \frac{3.93}{3.41}} = 997 \text{ kev}$$

The Rutherford differential cross-section, from equation 32, is

$$d\sigma_R/d\Omega = \frac{.02562}{(.997)^2 x (.70711)^4} = .1031 \text{ barns/steradian}$$

Thus

$$\frac{d\sigma/d\Omega}{d\sigma_R/d\Omega} = \frac{.2634}{.1031} = 2.56$$

(2) Calculation of the theoretical elastic scattering cross-section at $E_1 = 997$ kev and $\theta_{CM} = 90^{\circ}$

The theoretical cross-section that will be evaluated in the following calculation is given by equation 75, in which the non-Coulomb contribution to the elastic scattering is assumed to arise from an arbitrary amount of s-wave and a p-wave $J_B = 2^+$ state at $E_R = 980$ kev. The fitting parameters that will be used are those deduced from the theoretical analysis of the angular distribution at 998 kev.

For the special case $\theta_{CM} = 90^{\circ}$, equation 75 becomes

$$\frac{d\sigma/d\Omega}{d\sigma_R/d\Omega} = 1 + \left[\frac{\sin\xi}{k\sqrt{R}} - \frac{1}{2k^2R}\right]\left(\frac{3}{8}f_1 + \frac{5}{8}f_2 - 1\right) - \frac{\cos\xi}{k\sqrt{R}}\left(\frac{3}{8}g_1 + \frac{5}{8}g_2\right)$$

$$- \frac{1}{4k^2R}\left[1 - \frac{3}{8}(f_1^2 + g_1^2) - \frac{5}{8}(f_2^2 + g_2^2)\right] + \frac{13}{32k^2R}\left(\alpha_1^2 \frac{\Gamma_{p_2}}{\Gamma_2}\right)^2 \sin^2\beta_1$$

From theoretical fitting the following parameters are deduced at 998 kev:

$$a_1^2 \Gamma_{p_2}/\Gamma_2 = 0.9$$

$$\sin^2 \beta_1 = .8129$$

$$f_1 = -.150 \quad g_1 = -.930 \quad f_2 = -.223 \quad g_2 = .092$$

Thus

$$(\tfrac{3}{8} f_1 + \tfrac{5}{8} f_2 - 1) = -.056 - .139 - 1.000 = -1.195$$

$$(\tfrac{3}{8} g_1 + \tfrac{5}{8} g_2) = -.349 + .058 \qquad = -.291$$

$$1 - \tfrac{3}{8}(f_1^2 + g_1^2) - \tfrac{5}{8}(f_2^2 + g_2^2) = 1 - .333 - .036 \qquad = .631$$

The Coulomb cross-section $R = d\sigma_R/d\Omega$, is calculated in Part (1) to be .1031 barns/steradian

$$k^2 = \frac{p^2}{\hbar^2} = \frac{2\mu E_{CM}}{\hbar^2} = 2\left(\frac{M_o}{M_o + M_1}\right)^2 E_L \times \frac{M_o}{m_o} \times \frac{m_o}{\hbar^2}$$

$$= 2 \times (.8994)^2 \times 1836 \times \frac{m_o}{a_o m_o e^2} E_L$$

$$= 2970 \times \frac{E_L}{a_o r_o m_o c^2}$$

$$= \frac{2970 \qquad E_L(\text{mev})}{2.818 \times 10^{-13} \text{cm} \times 5.292 \times 10^{-9} \text{cm} \times .511}$$

$$= 3.897 \times 10^{24} E_L(\text{mev})\ \text{cm}^{-2}$$

$$\therefore k^2 R = 3.897 \times .997 \times .1031 = .4005$$

and $\dfrac{1}{k^2 R} = 2.497 \qquad \dfrac{1}{k\sqrt{R}} = 1.580$

From equation 72

$$\xi \approx -\alpha_o \ln \sin^2 \frac{\theta_{CM}}{2}$$

$$\alpha_o^2 \approx \frac{Z_1^2 Z_o^2 e^4}{\hbar^2 v^2} \approx \left(\frac{Z_1 Z_o e^2}{\hbar}\right)^2 \frac{M_o}{2E_L}$$

$$\approx \left(\frac{Z_1 Z_o}{137}\right)^2 \frac{M_o c^2}{2E_L}$$

$$\approx \left(\frac{4}{137}\right)^2 \frac{938.2}{2E_L(\text{mev})}$$

$$\approx \frac{.39982}{E_L(\text{mev})}$$

$$\approx .4010$$

$$\therefore \alpha_o \approx .6333$$

and $\xi \approx -.6333(-.6931) \approx .4389$

$$\sin\xi \approx .4249 \qquad \cos\xi \approx .9052$$

$$\frac{\sin\xi}{k\sqrt{R}} - \frac{1}{2k^2 R} \approx .6713 - 1.2485 \approx -.5772$$

$$\frac{\cos\xi}{k\sqrt{R}} \approx 1.4302$$

$$\frac{1}{4k^2 R} \approx .6243$$

$$\frac{13}{32k^2 R} \approx 1.0145$$

Thus

$$\frac{d\ \ /d\Omega}{d\ {}_R/d\Omega} = 1 + (-.5772)\text{x}(-1.195) - 1.4302\text{x}(-.291) - .631\text{x}.6243$$

$$+ \{1.0145 \times 0.9 \times .8129\}$$

$$= 1 + .7120 + \{.7422\}$$

$$= 2.454$$

This is 4°/o lower than the experimental value of 2.56 calculated in Part (1).

The number in brackets above is the contribution to the theoretical cross-section that arises from the presence of the assumed 2^+ p-wave state. This state is seen to contribute about 50°/o of the total anomaly at this particular angle and energy.

REFERENCES

1. Ajzenberg and Lauritsen, R.M.P., 27, 77, (1955).
2. Elliott and Flowers, Proc. Roy. Soc. (London) A229, 536 (1955).
3. MacDonald, Phys. Rev. 98, 60, (1955).
4. Lauritsen, Lauritsen and Fowler, Phys. Rev. 59 241 (1941).
5. E. A. Milne, Ph.D. Thesis, California Institute of Technology, (1953).
6. Fowler, Lauritsen, Lauritsen, ~~Phys. Rev.~~ R.S.I. 18, 818 (1947).
7. Snyder, Rubin, Fowler, Lauritsen, R.S.I., 21, 852 (1950).
8. W. D. Warters, Ph.D. Thesis, California Institute of Technology (1953).
9. Bouricious and Shoemaker, R.S.I., 22, 183 (1951).
10. Fowler, Lauritsen, Lauritsen, R.M.P., 20, 236 (1948).
11. Thomas, Rubin, Fowler, Lauritsen, Phys. Rev. 75, 1612 (1949).
12. Bader, To be published in Phys. Rev.
13. Phillips, Phys. Rev. 97, 404 (1955).
14. Allison and Warshaw, R.M.P. 25, 779 (1953).
15. W. A. Wensel, Ph.D. Thesis, California Institute of Technology (1952).
16. Blatt and Weiskopf, Theoretical Nuclear Physics, Wiley and Sons, New York (1952).
17. Neuendorffer, Inglis, Hanna, Phys. Rev., 82, 75 (1951).
18. Wigner, Eisenbud, Phys. Rev. 72, 29, (1947).
19. Clegg (Private Communication).
20. Christy and Latter, R.M.P. 20, 185 (1948).
21. Breit et al., R.M.P. 23 (1951).
22. Devons and Hine, Proc. Roy. Soc. (London) 199A, 56 (1949).
23. Lane, AERE, T/R 1289, (1954). (Harwell Report, Unpublished).

REFERENCES (Cont'd)

24. Wigner, Phys. Rev. 98, 145 (1955).

25. Devons and Goldring, Proc. Phys. Soc. (London) 67A, 413 (1954).

26. R. F. Christy (Private communication).

27. Kurath, Phys. Rev. 101, 216 (1956).

28. A. A. Kraus, Jr., Ph. D. Thesis, California Institute of Technology (1953).

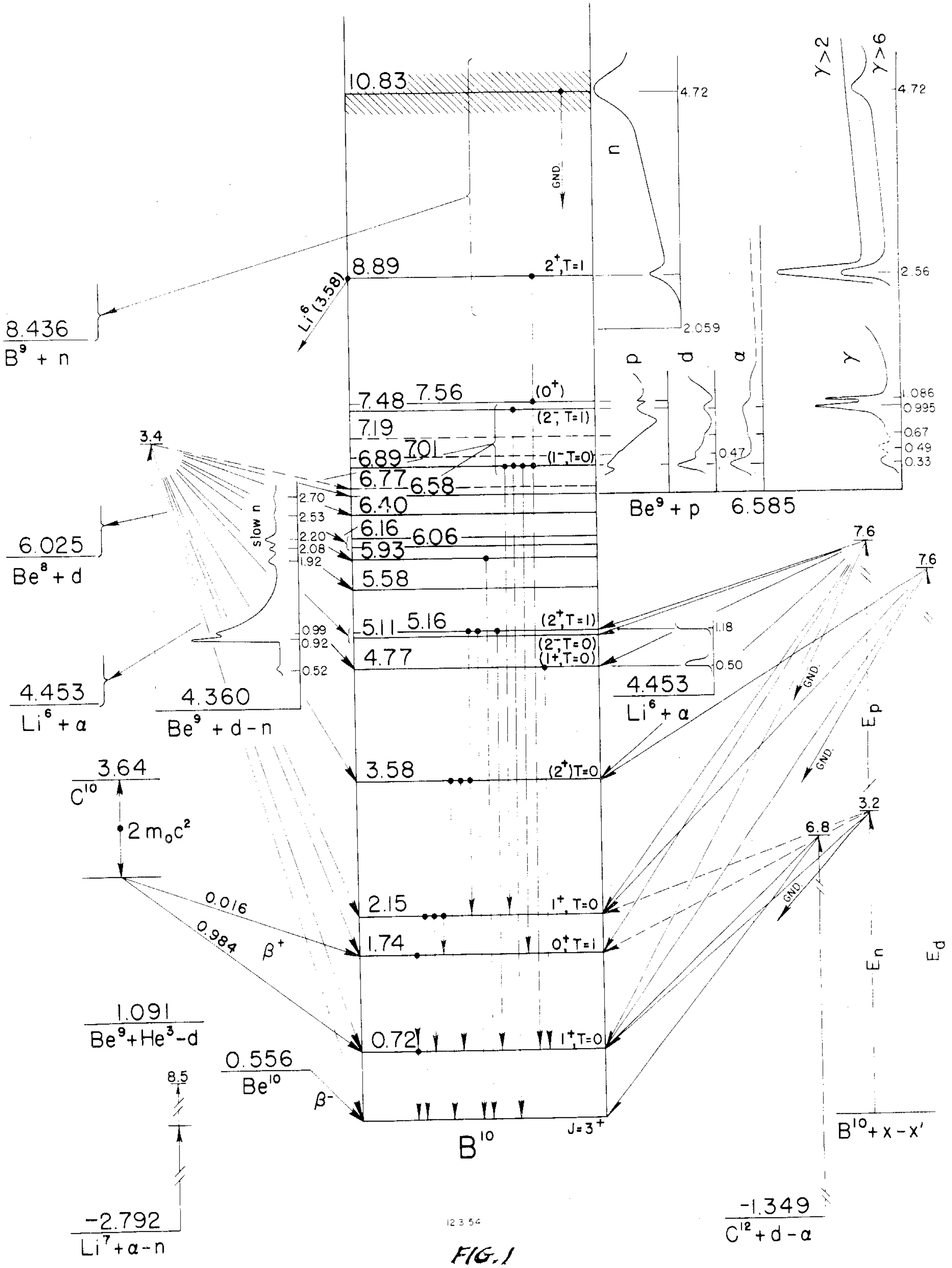
10.83
GND.
n
4.72
γ>2
γ>6
4.72
8.89
2+, T=1
Li6(3.58)
2.56
2.059
8.436
B9 + n
p
d
α
γ
7.48
7.56
(0+)
(2-, T=1)
1.086
0.995
7.19
0.67
7.01
0.49
6.89
(1-, T=0)
0.47
0.33
6.77
6.58
3.4
6.40
Be9 + p
6.585
2.70
2.53
slow n
6.025
Be8 + d
6.16
2.20
6.06
2.08
5.93
1.92
5.58
7.6
7.6
5.11
5.16
(2+, T=1)
1.18
0.99
0.92
(2-, T=0)
4.77
(1+, T=0)
0.50
0.52
4.453
Li6 + α
4.453
Li6 + α
4.360
Be9 + d - n
GND.
Ep
GND.
3.64
C10
3.58
(2+)T=0
3.2
2 m0c2
6.8
GND
0.016
2.15
1+, T=0
0.984
β+
1.74
0+, T=1
En
Ed
1.091
Be9+He3-d
0.72
1+, T=0
0.556
Be10
8.5
β-
J=3+
B10
B10 + x - x'
-1.349
C12 + d - α
-2.792
Li7 + α - n
12 3 54

FIG. 1

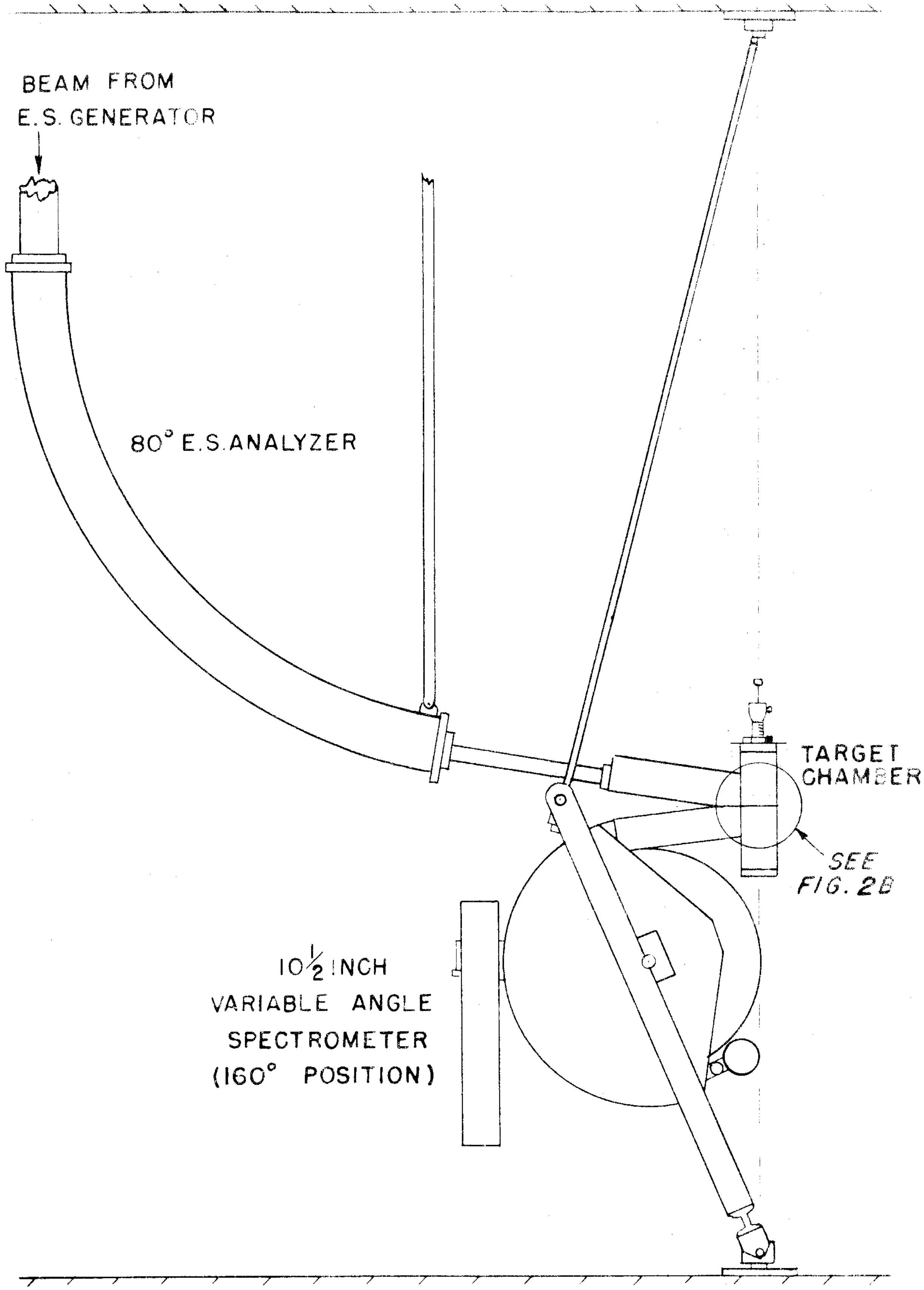

FIGURE 2A - LAYOUT OF APPARATUS

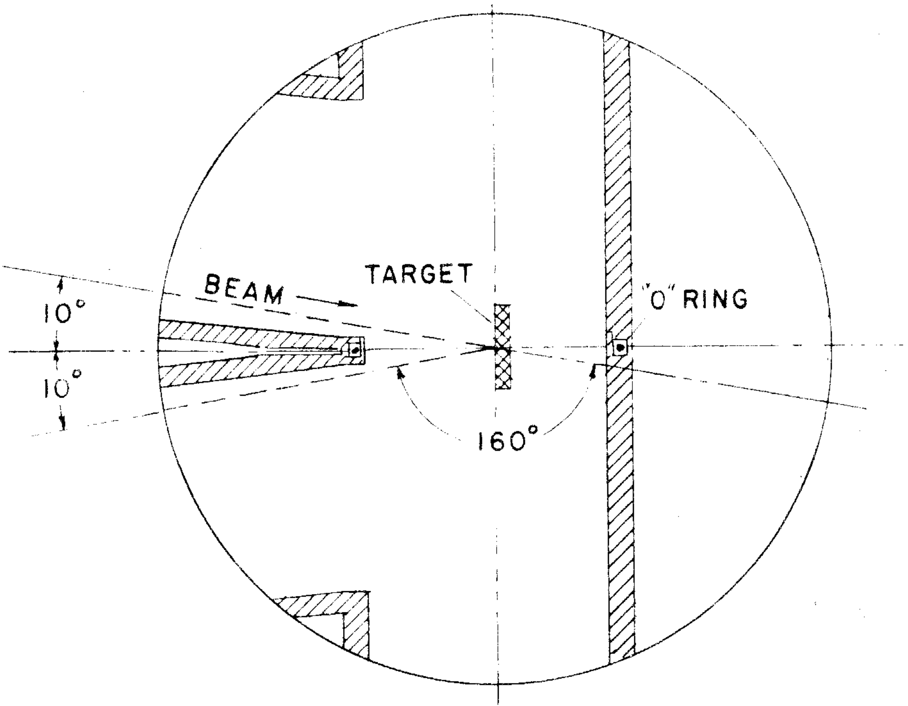

160° POSITION

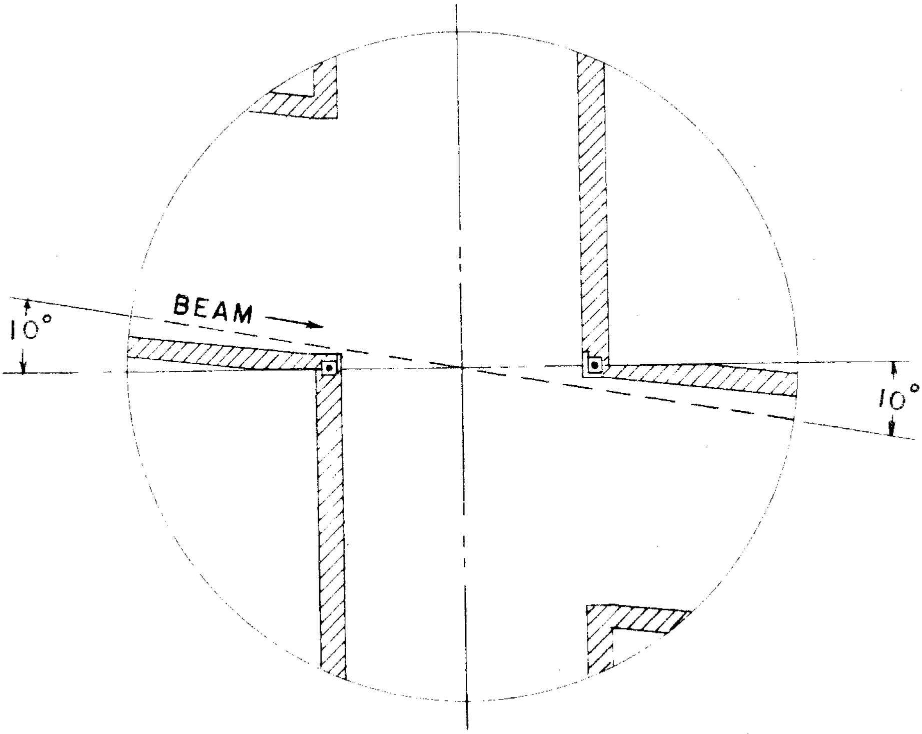

0° POSITION

FIGURE 2B- TARGET CHAMBER DETAIL

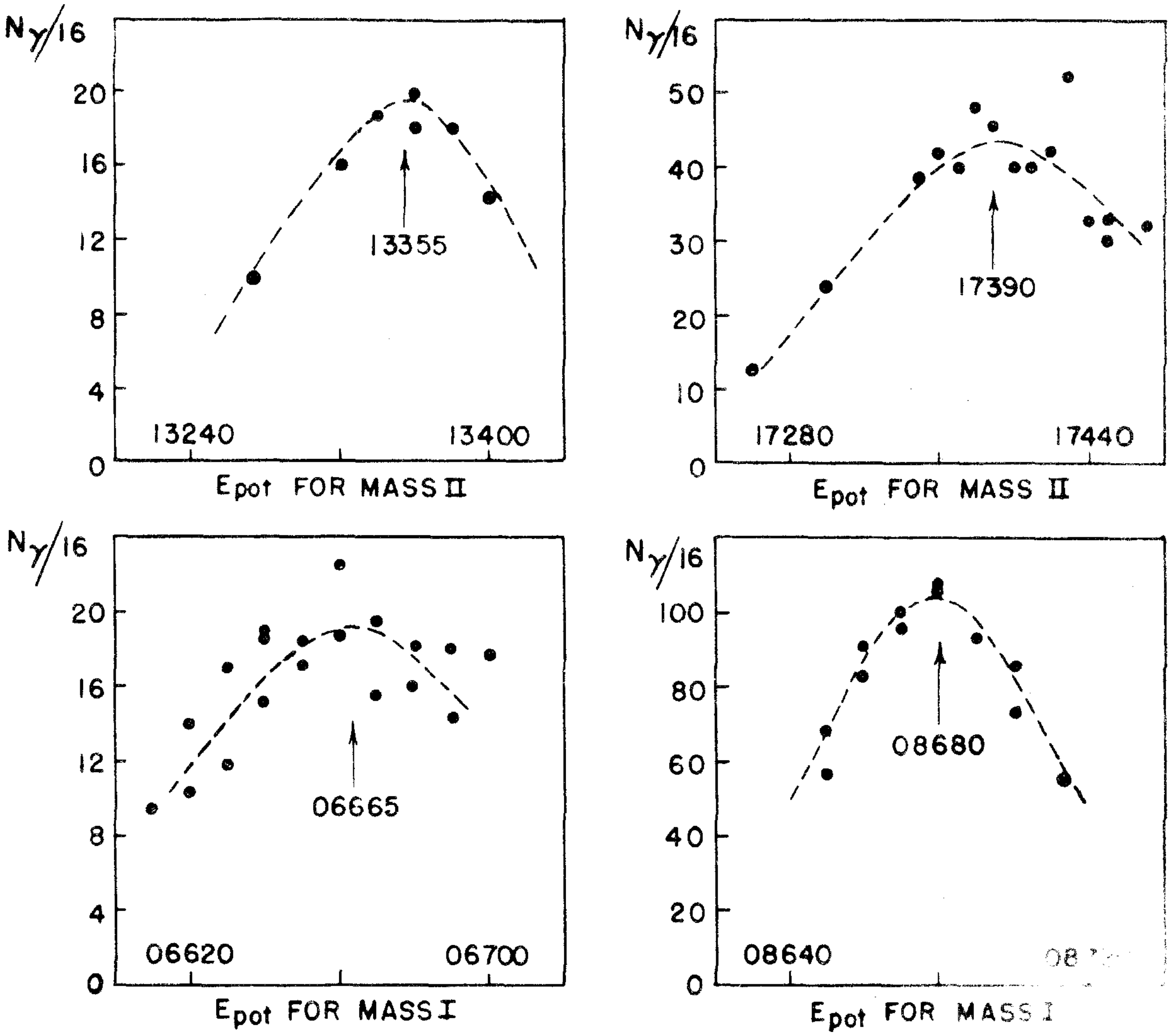

669 KEV RESONANCE 873.5 KEV RESONANCE

COMPARISON OF ELECTROSTATIC ANALYZER ENERGY CALIBRATIONS WITH MASS I AND II BEAMS INCIDENT ON A THIN FLUORINE TARGET.

FIGURE 3

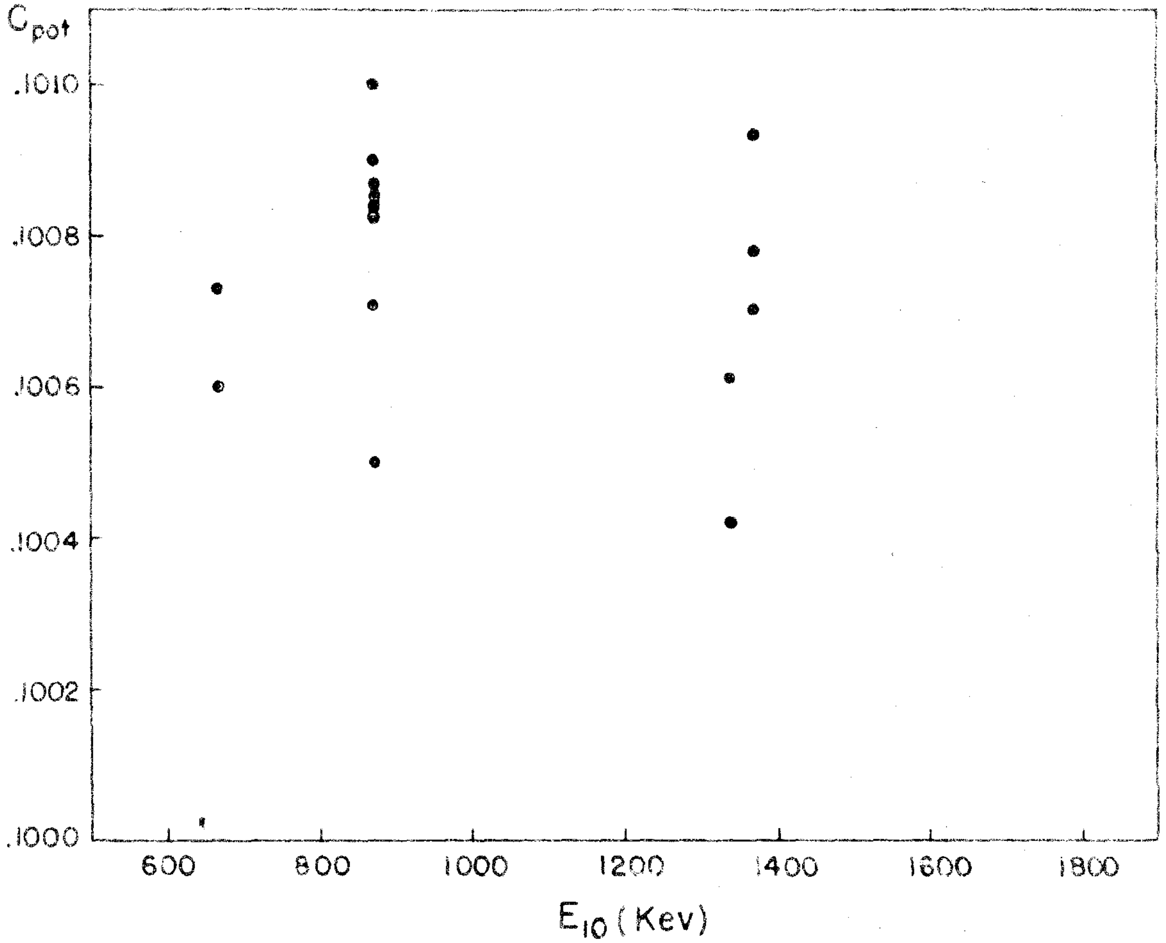

ELECTROSTATIC ANALYZER ENERGY CALIBRATIONS OBTAINED FROM THIN TARGET STUDIES OF $F^{19}(p,\gamma)$

(NOTE PRESENCE OF SUPPRESSED ZERO ON ORDINATE SCALE)

FIGURE 4

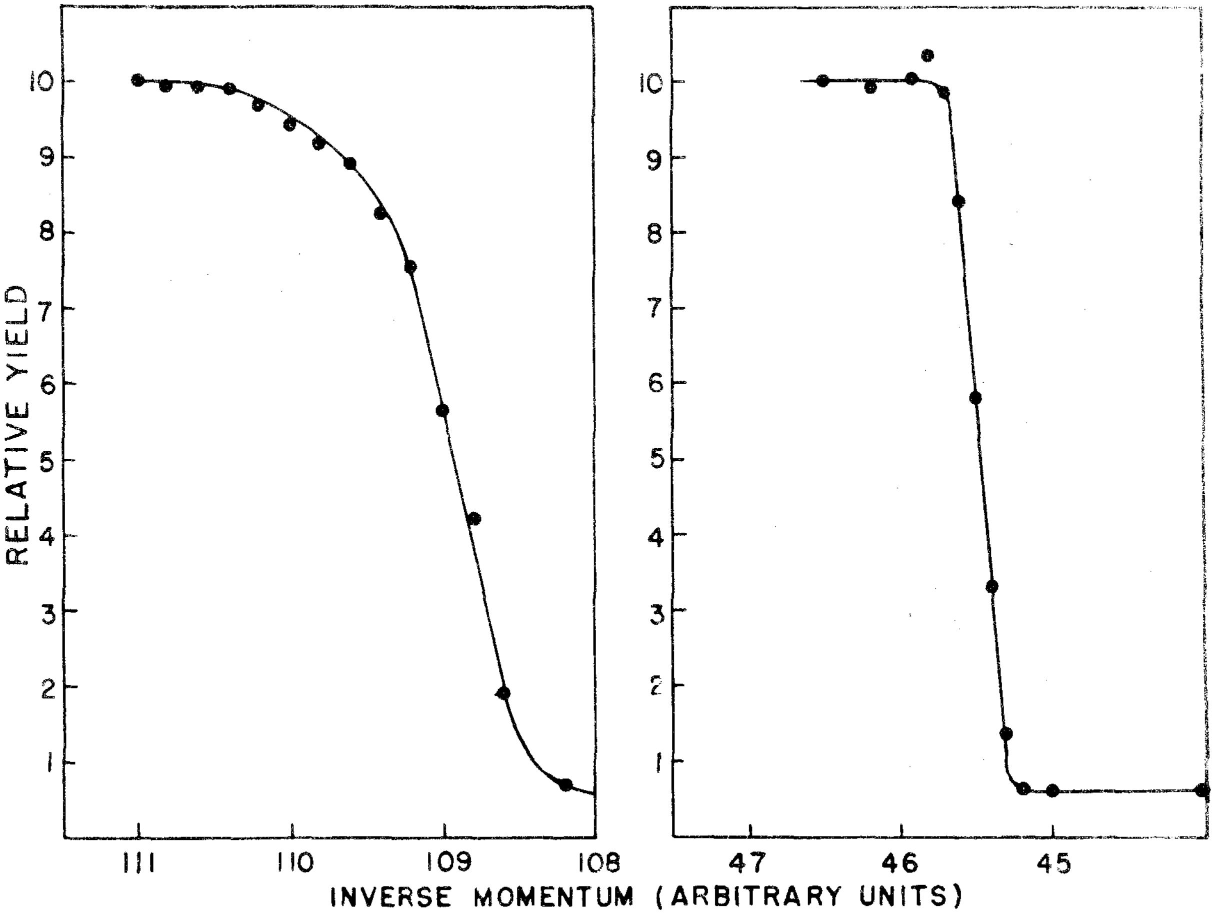

$E_{10} = 222$ Kev

$\theta_{LAB} = 158° 39'$

$E_{10} = 1007$ Kev

$\theta_{LAB} = 83° 35'$

TYPICAL MOMENTUM PROFILES OF PROTONS ELASTICALLY SCATTERED FROM A THICK BERYLLIUM TARGET.

FIGURE 5

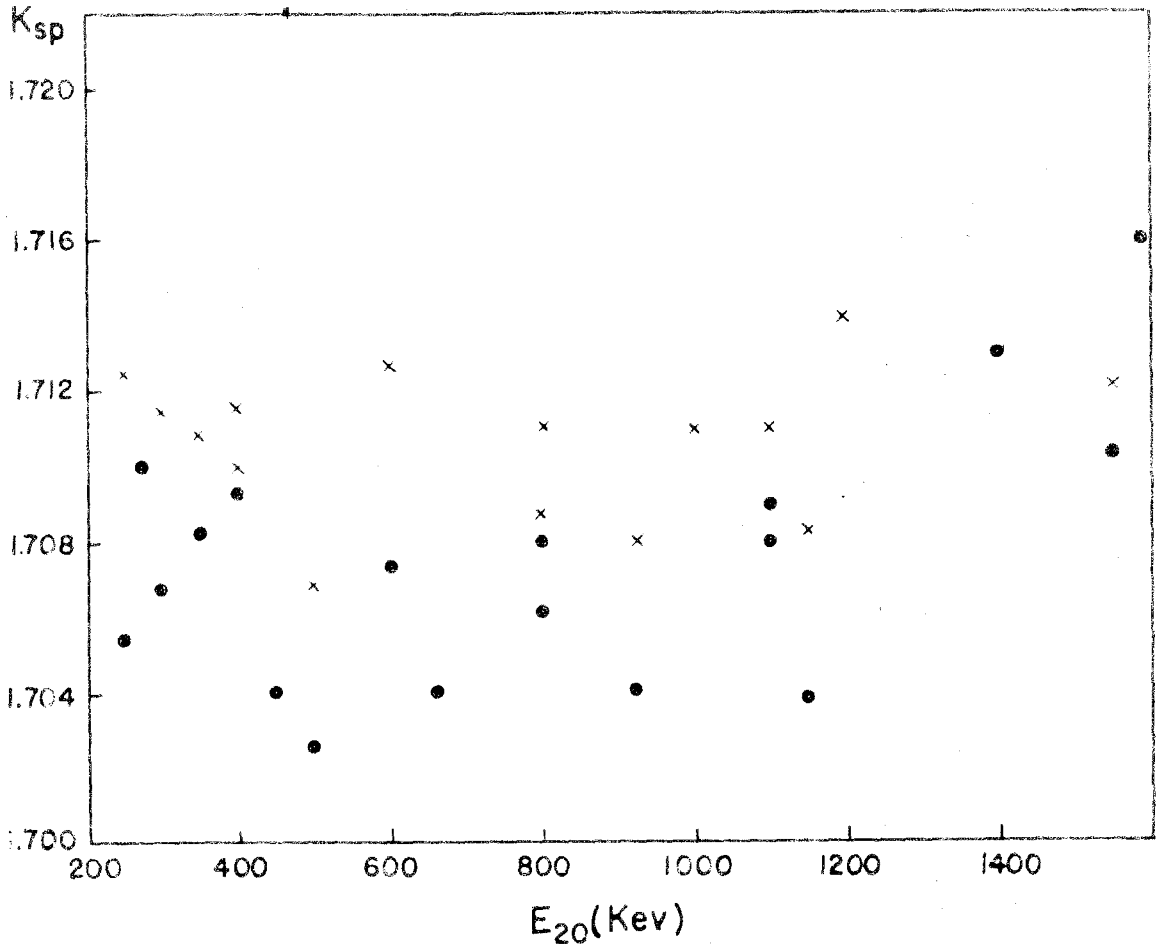

MAGNETIC ANALYZER ENERGY CALIBRATIONS

● DATA OBTAINED FROM LARGE ANGLE SCATTERING

× DATA OBTAINED FROM SCATTERING ANGLES <135°

(NOTE PRESENCE OF SUPPRESSED ZERO ON ORDINATE SCALE)

FIGURE 6

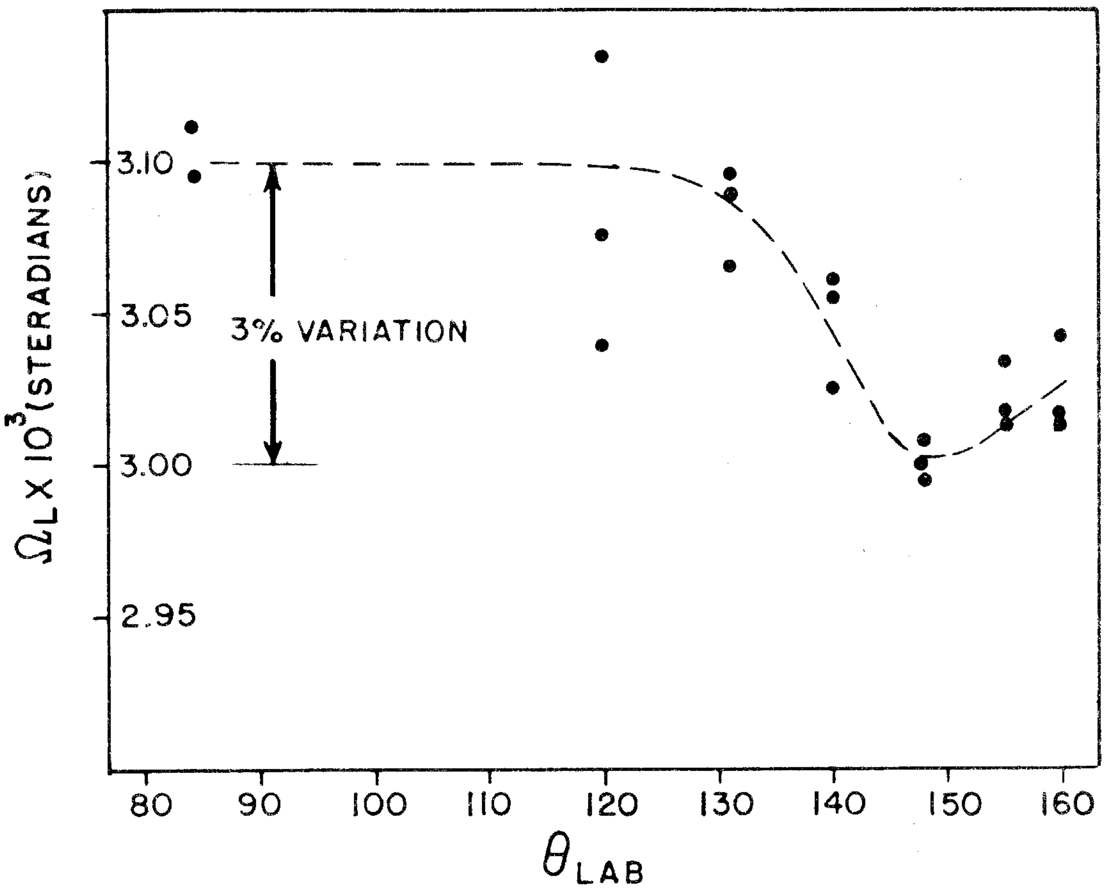

VARIATION OF EFFECTIVE ACCEPTANCE SOLID ANGLE WITH SCATTERING ANGLE

(NOTE SUPPRESSED ZERO OF ORDINATE SCALE)

FIGURE 7

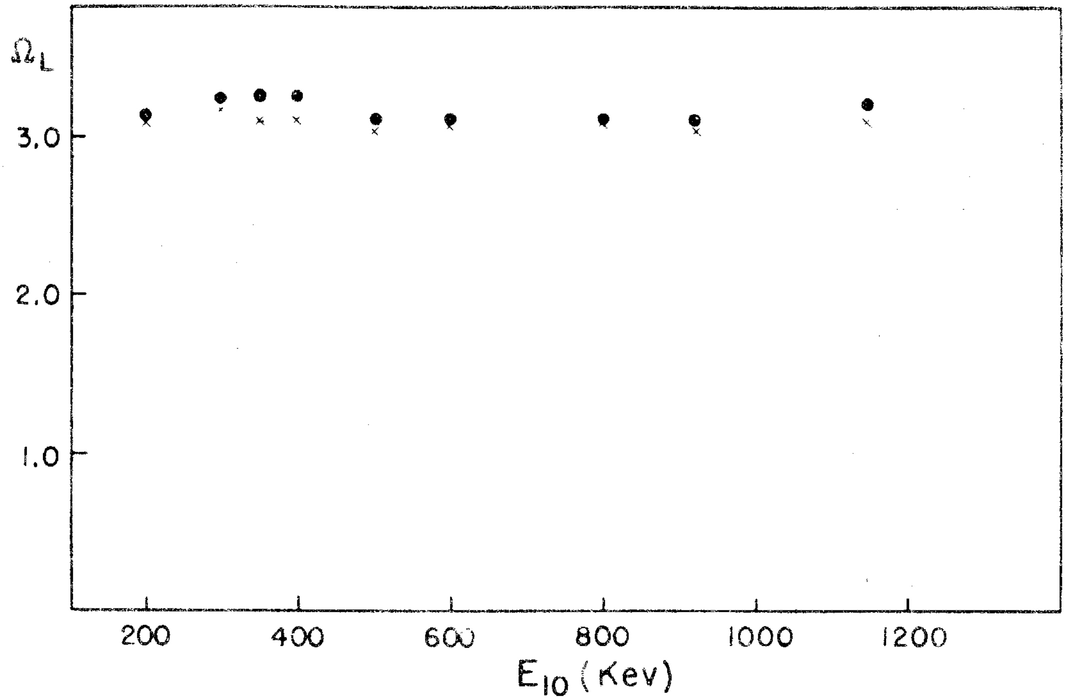

MAGNETIC SPECTROMETER EFFECTIVE ACCEPTANCE SOLID ANGLE.

- ● DATA AT $\theta_{LAB} = 120°$
- × DATA AT $\theta_{LAB} = 158° 39'$

FIGURE 8

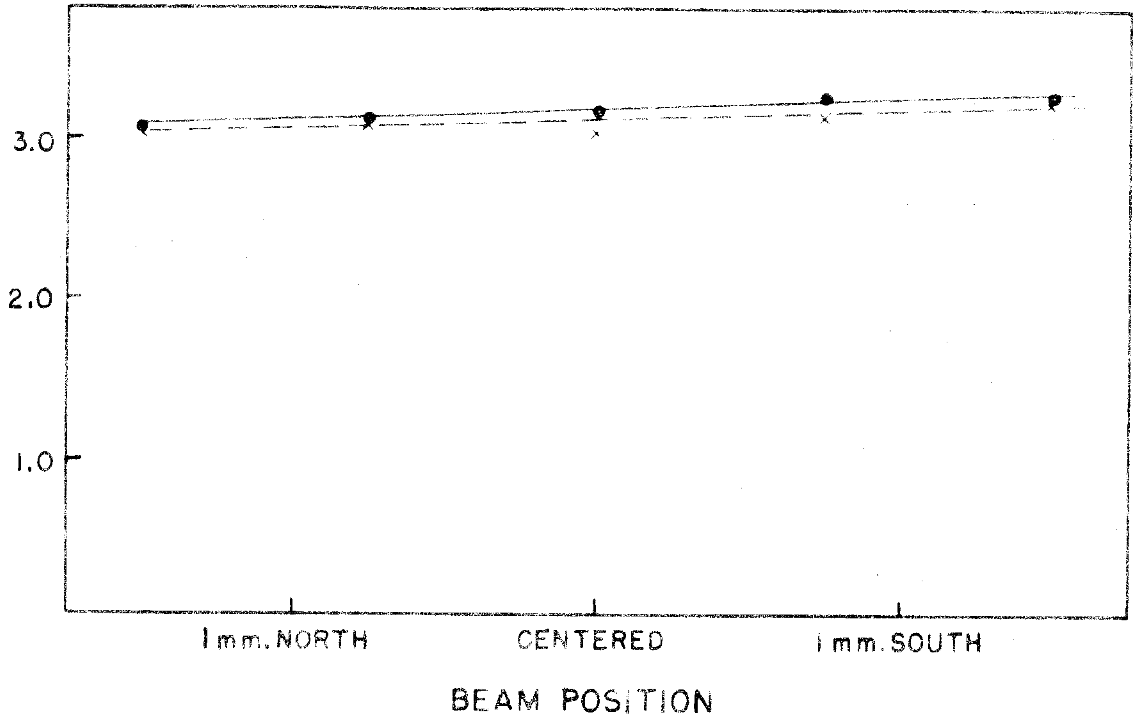

VARIATION OF THE EFFECTIVE ACCEPTANCE SOLID ANGLE WITH HORIZONTAL BEAM POSITION.

- ● DATA AT $\theta_{LAB} = 83° \; 35'$
- × DATA AT $\theta_{LAB} = 158° \; 39'$

FIGURE 9

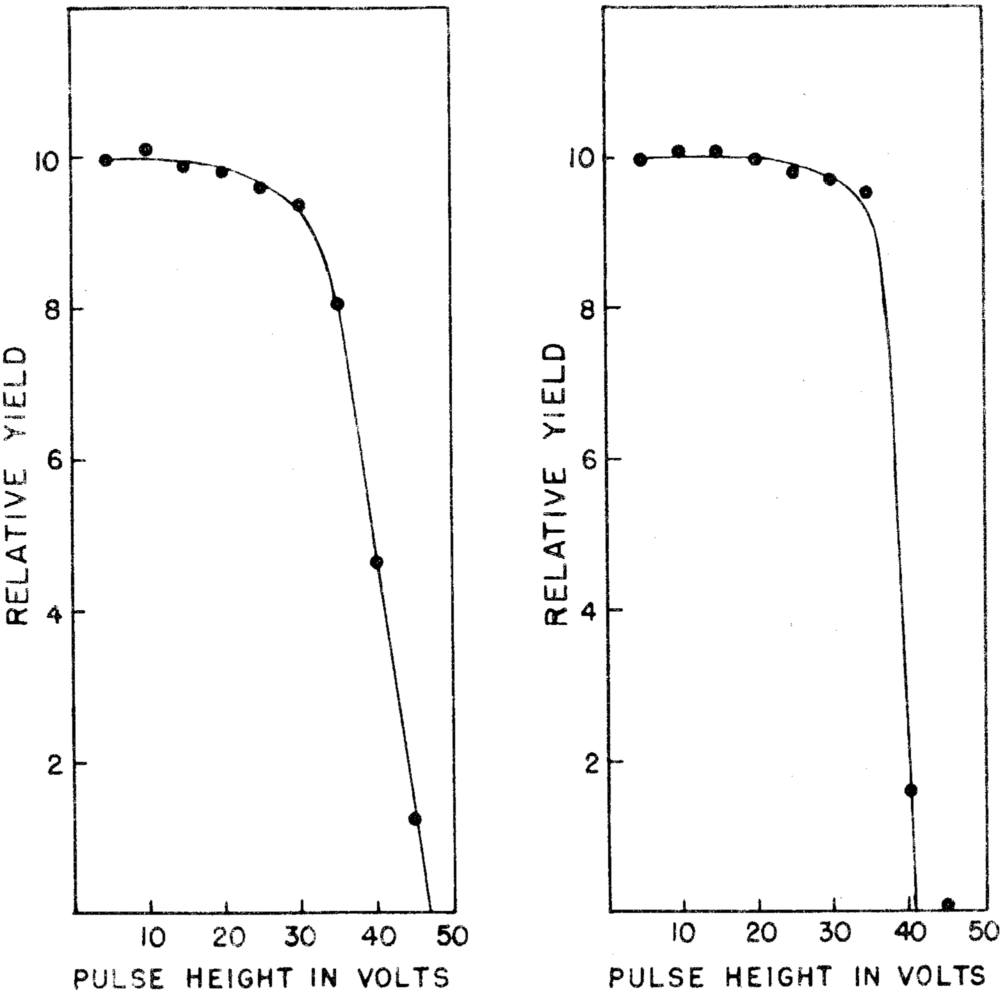

E_{20}=140 Kev

E_{20}=940 Kev

TYPICAL INTEGRAL BIAS CURVES FOR PROTONS ELASTICALLY SCATTERED FROM BERYLLIUM.

FIGURE 10

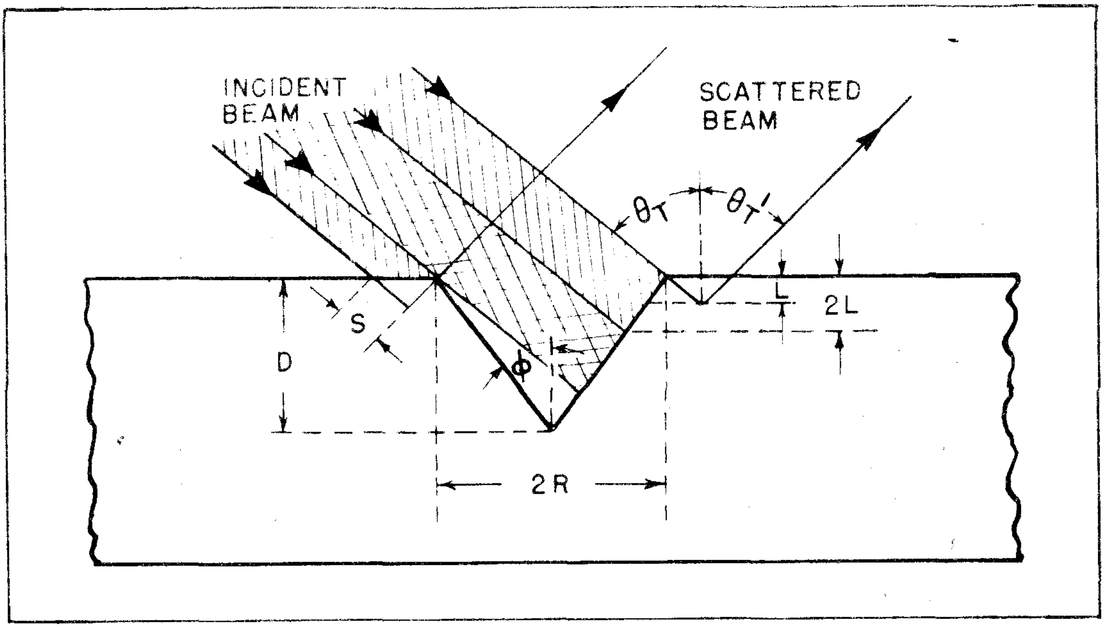

SCATTERING OF PARTICLES FROM A SCRATCHED SURFACE

FIGURE 11A

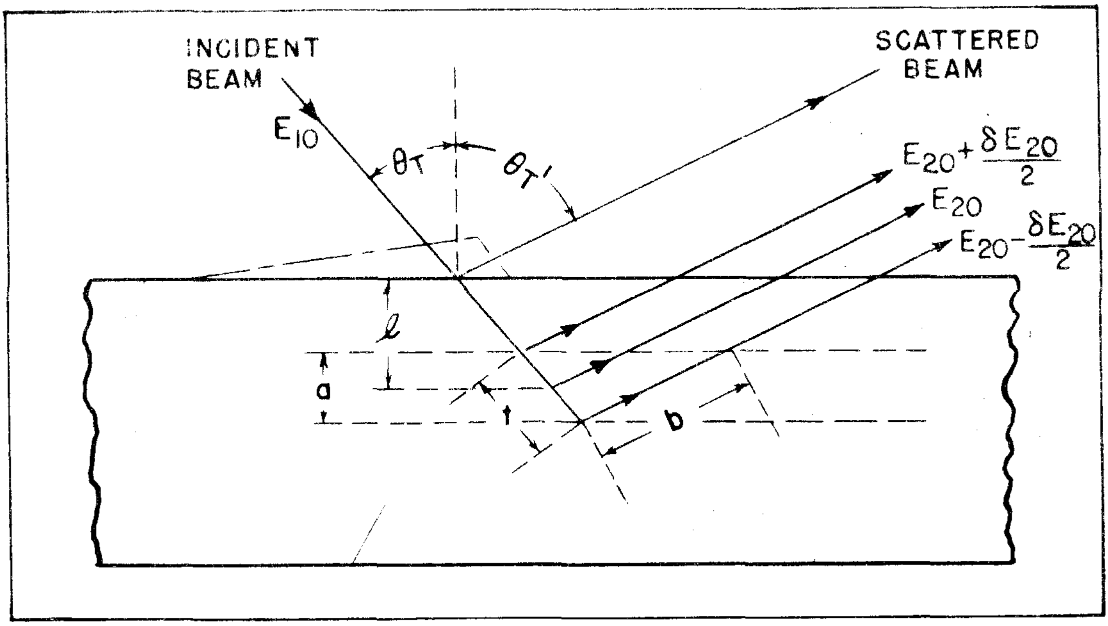

SCATTERING OF PARTICLES FROM A SMOOTH SERVICE

FIGURE 11B

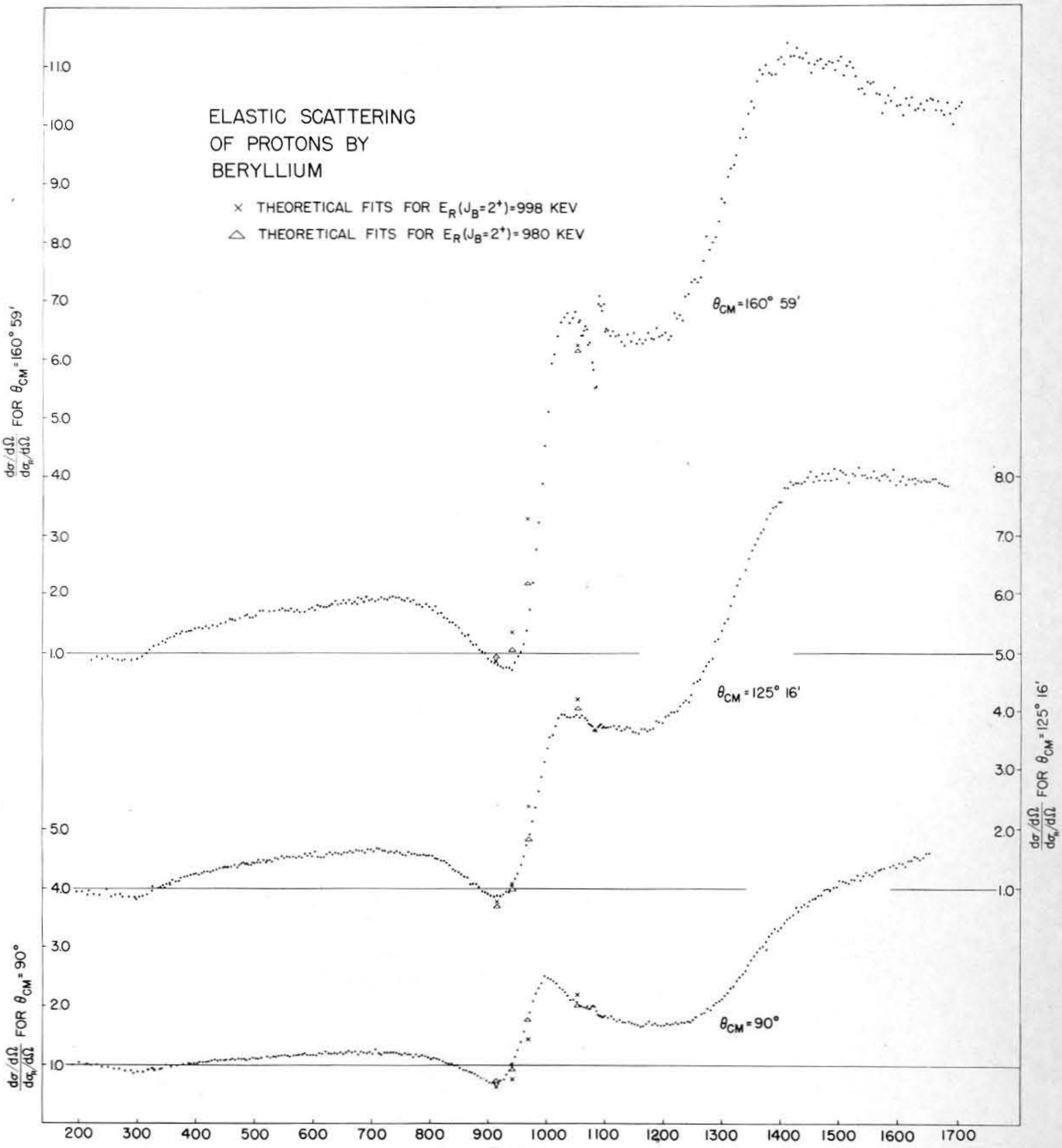
ELASTIC SCATTERING
OF PROTONS BY
BERYLLIUM
× THEORETICAL FITS FOR $E_R(J_B=2^+)=998$ KEV
△ THEORETICAL FITS FOR $E_R(J_B=2^+)=980$ KEV
$\theta_{CM}=160° 59'$
$\theta_{CM}=125° 16'$
$\theta_{CM}=90°$
$\frac{d\sigma/d\Omega}{d\sigma_R/d\Omega}$ FOR $\theta_{CM}=160° 59'$
$\frac{d\sigma/d\Omega}{d\sigma_R/d\Omega}$ FOR $\theta_{CM}=125° 16'$
$\frac{d\sigma/d\Omega}{d\sigma_R/d\Omega}$ FOR $\theta_{CM}=90°$
11.0
10.0
9.0
8.0
7.0
6.0
5.0
4.0
3.0
2.0
1.0
8.0
7.0
6.0
5.0
4.0
3.0
2.0
1.0
5.0
4.0
3.0
2.0
1.0
200
300
400
500
600
700
800
900
1000
1100
1200
1300
1400
1500
1600
1700
E_1 (KEV)

FIG. 12

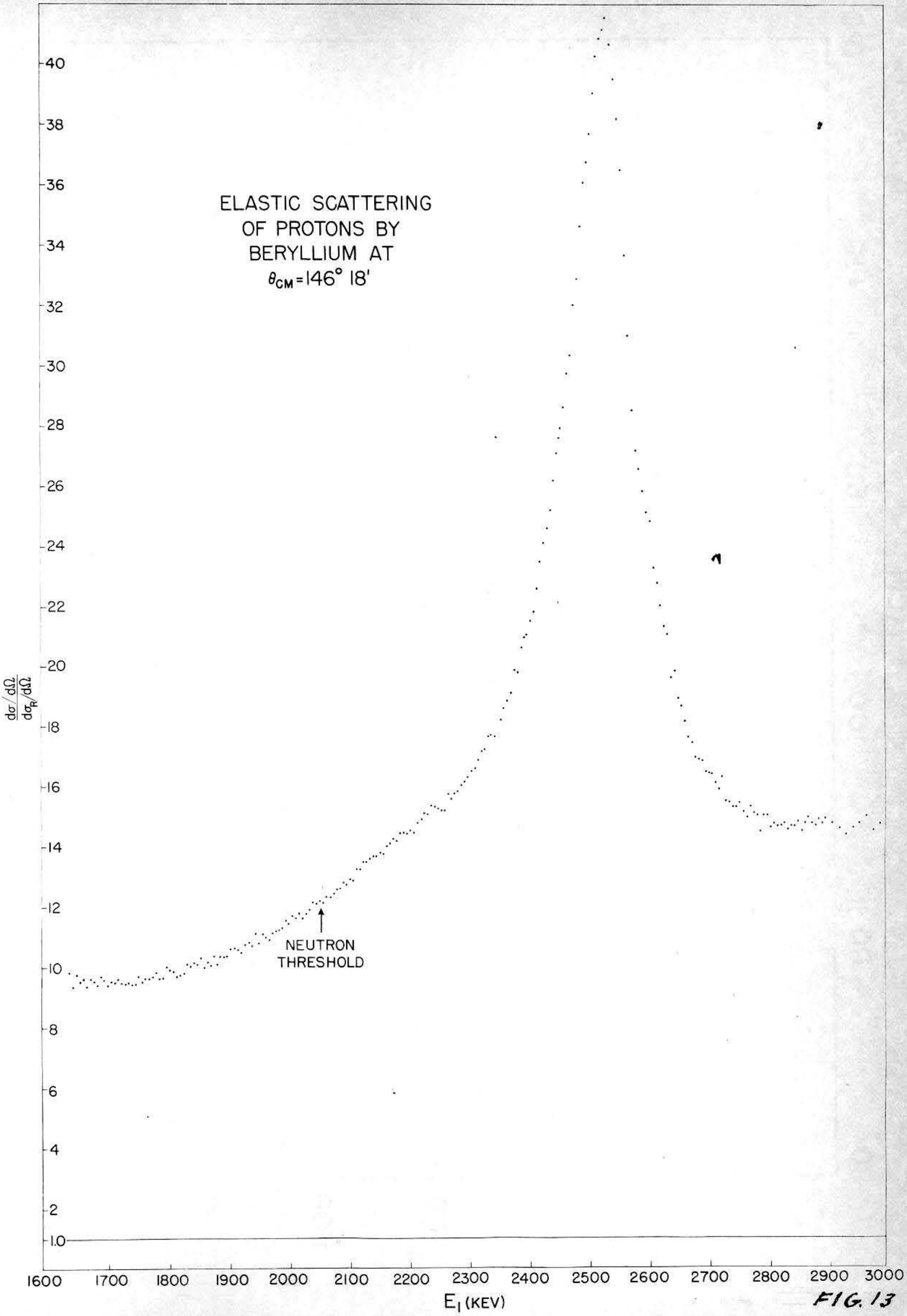
ELASTIC SCATTERING OF PROTONS BY BERYLLIUM AT θ_{CM} = 146° 18'
NEUTRON THRESHOLD
$\frac{d\sigma/d\Omega}{d\sigma_R/d\Omega}$
40
38
36
34
32
30
28
26
24
22
20
18
16
14
12
10
8
6
4
2
1.0
1600
1700
1800
1900
2000
2100
2200
2300
2400
2500
2600
2700
2800
2900
3000
E_1 (KEV)

FIG. 13

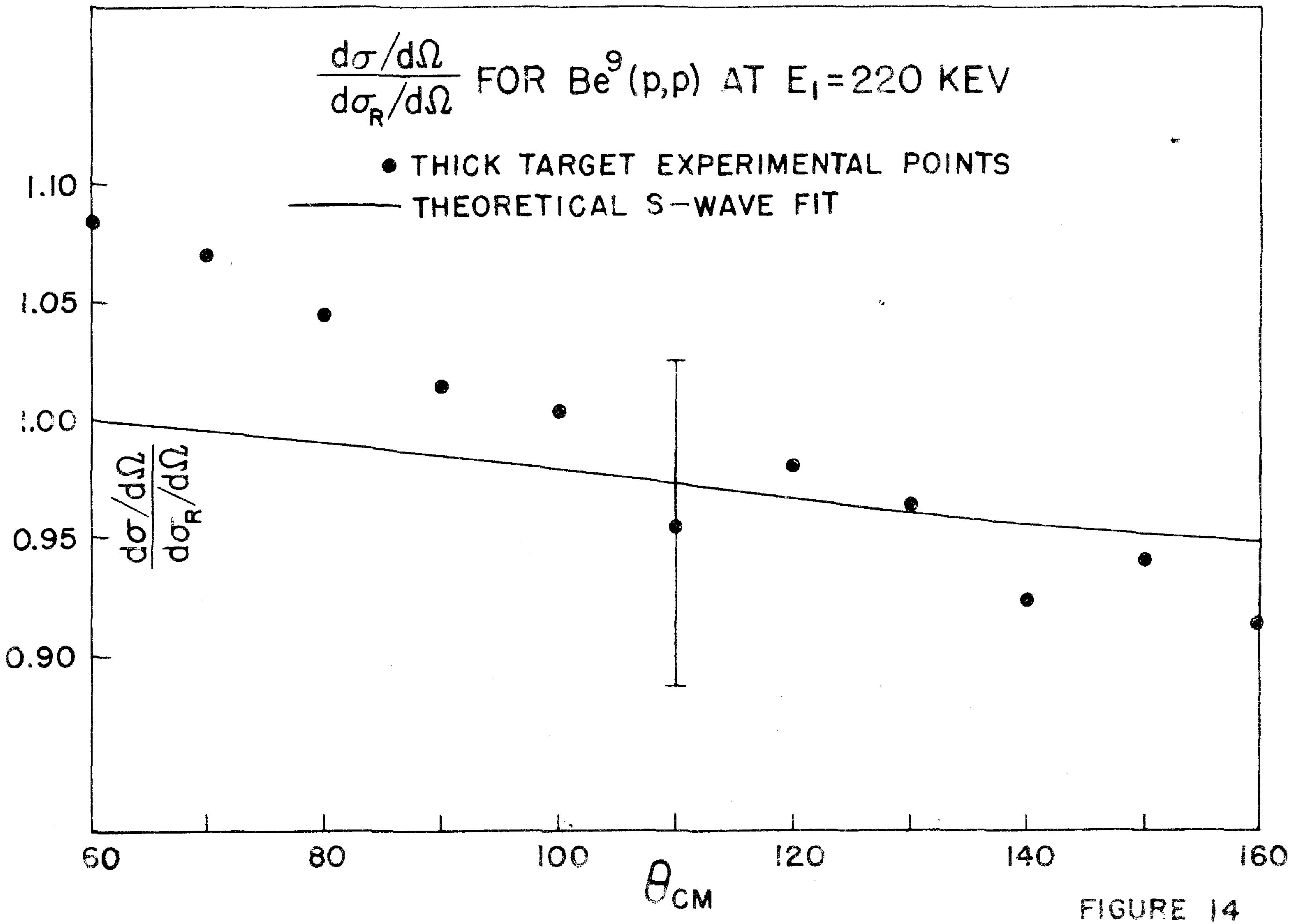
$\frac{d\sigma/d\Omega}{d\sigma_R/d\Omega}$ FOR $Be^9(p,p)$ AT $E_1=220$ KEV
● THICK TARGET EXPERIMENTAL POINTS
THEORETICAL S-WAVE FIT
1.10
1.05
1.00
0.95
0.90
$\frac{d\sigma/d\Omega}{d\sigma_R/d\Omega}$
60
80
100
120
140
160
θ_{CM}

FIGURE 14

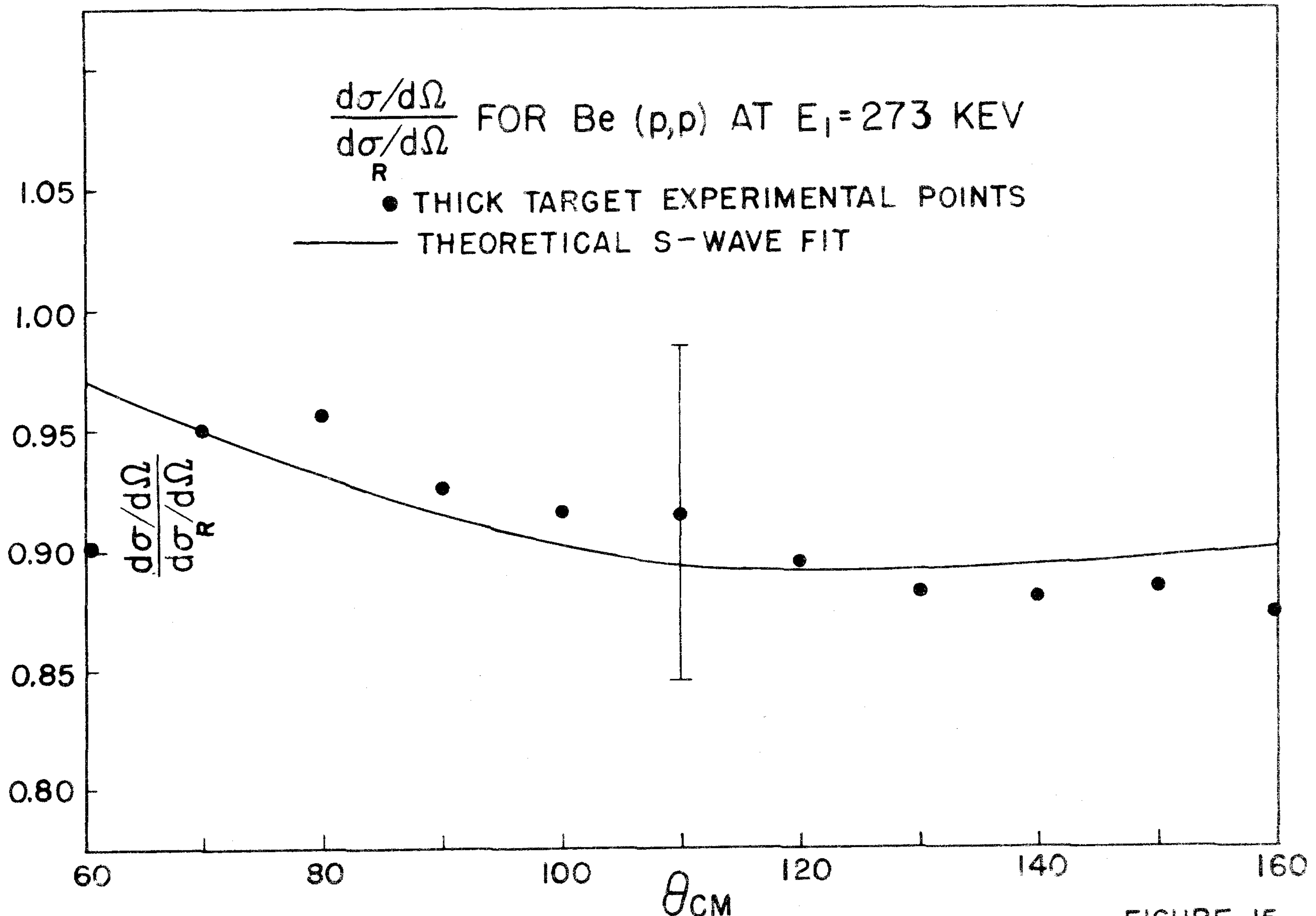
$\frac{d\sigma/d\Omega}{d\sigma/d\Omega_R}$ FOR Be (p,p) AT E_1=273 KEV
● THICK TARGET EXPERIMENTAL POINTS
THEORETICAL S-WAVE FIT
$\frac{d\sigma/d\Omega}{d\sigma/d\Omega_R}$
1.05
1.00
0.95
0.90
0.85
0.80
60
80
100
120
140
160
θ_{CM}

FIGURE 15

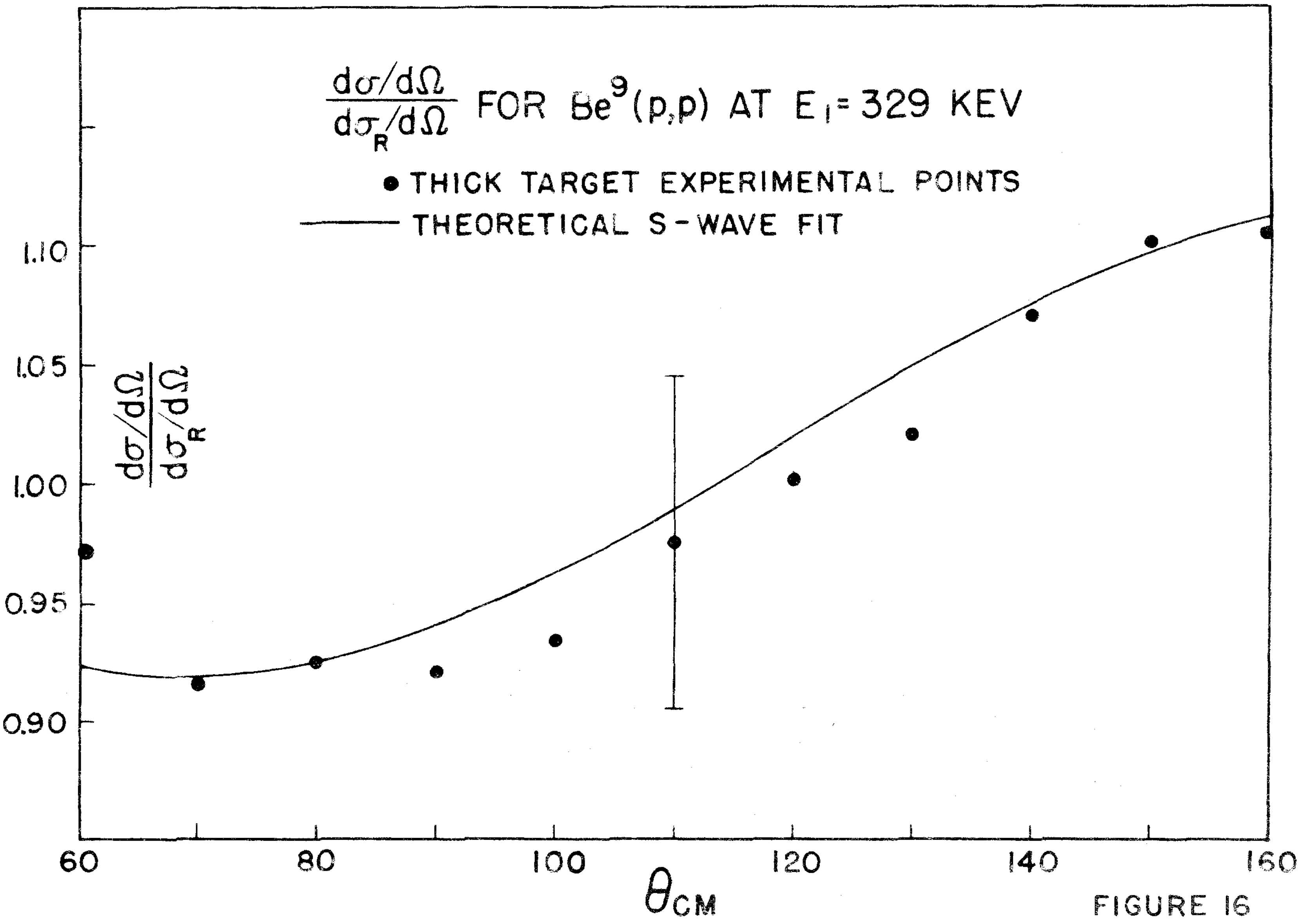
$\frac{d\sigma/d\Omega}{d\sigma_R/d\Omega}$ FOR $Be^9(p,p)$ AT $E_1 = 329$ KEV
● THICK TARGET EXPERIMENTAL POINTS
— THEORETICAL S-WAVE FIT
$\frac{d\sigma/d\Omega}{d\sigma_R/d\Omega}$
1.10
1.05
1.00
0.95
0.90
60
80
100
120
140
160
θ_{CM}

FIGURE 16

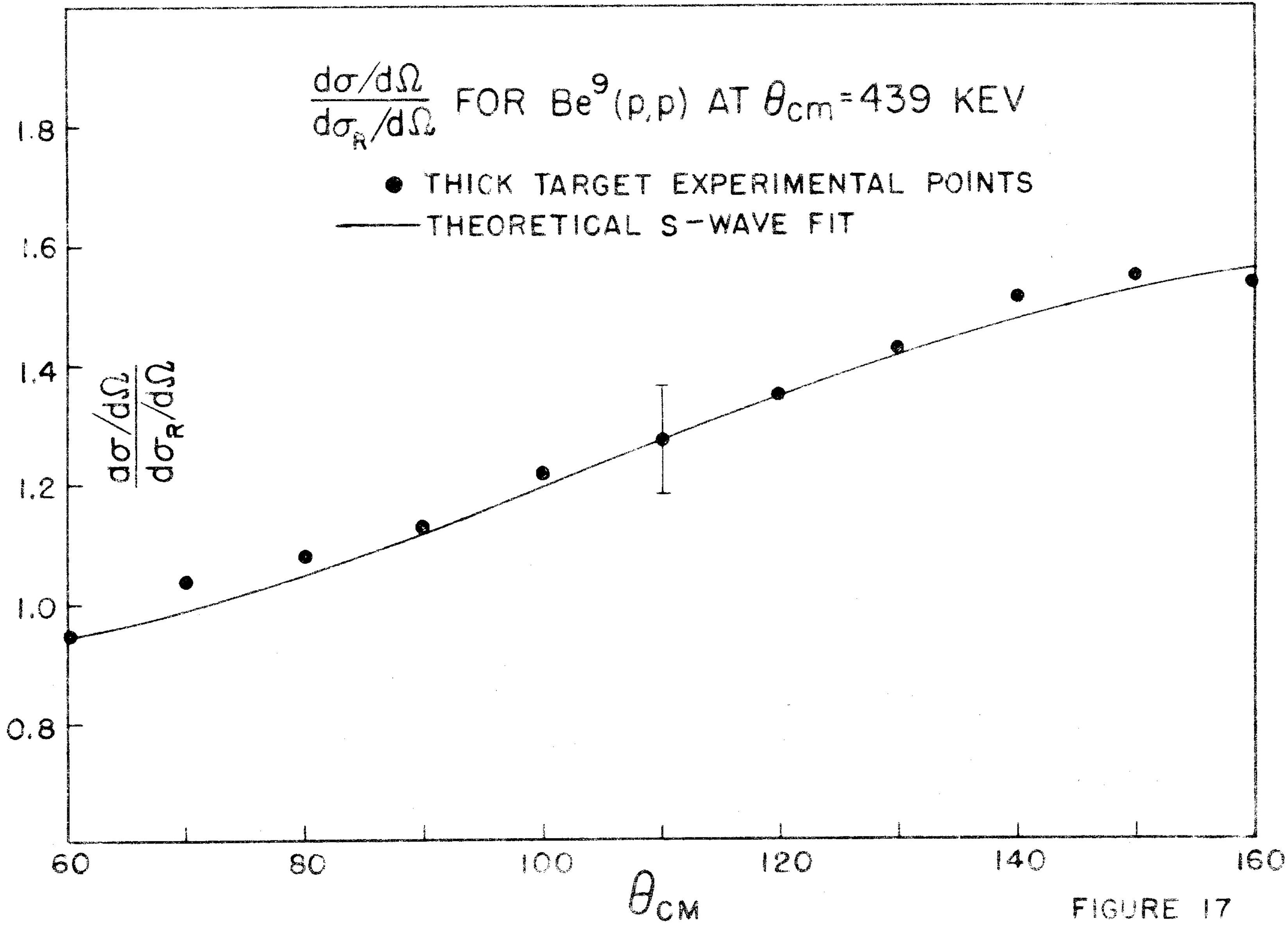
$\frac{d\sigma/d\Omega}{d\sigma_R/d\Omega}$ FOR $Be^9(p,p)$ AT $\theta_{cm}=439$ KEV
● THICK TARGET EXPERIMENTAL POINTS
—— THEORETICAL S-WAVE FIT
$\frac{d\sigma/d\Omega}{d\sigma_R/d\Omega}$
1.8
1.6
1.4
1.2
1.0
0.8
60
80
100
120
140
160
θ_{CM}

FIGURE 17

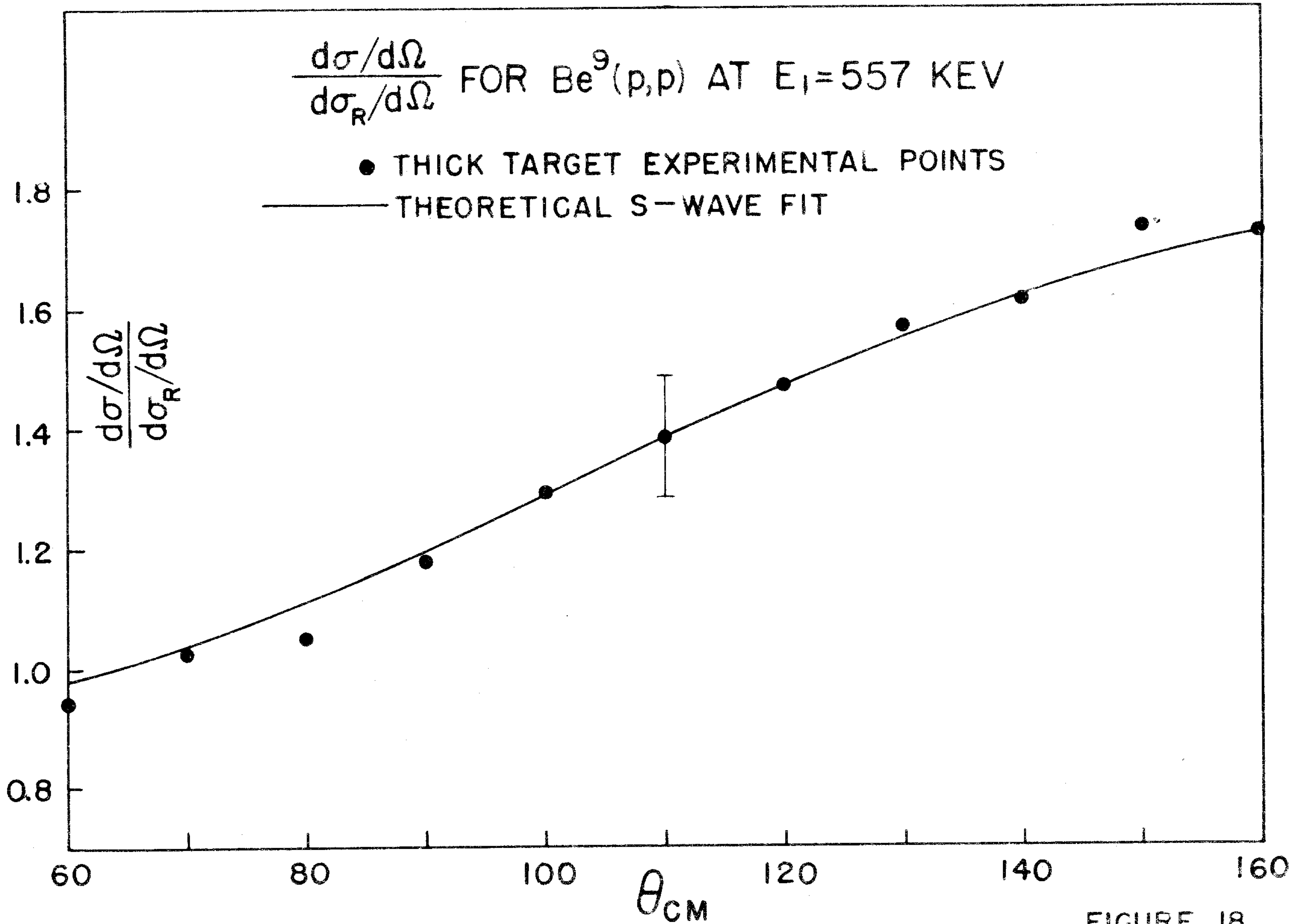
$\frac{d\sigma/d\Omega}{d\sigma_R/d\Omega}$ FOR $Be^9(p,p)$ AT $E_1 = 557$ KEV
● THICK TARGET EXPERIMENTAL POINTS
—— THEORETICAL S—WAVE FIT
$\frac{d\sigma/d\Omega}{d\sigma_R/d\Omega}$
1.8
1.6
1.4
1.2
1.0
0.8
60
80
100
120
140
160
θ_{CM}

FIGURE 18

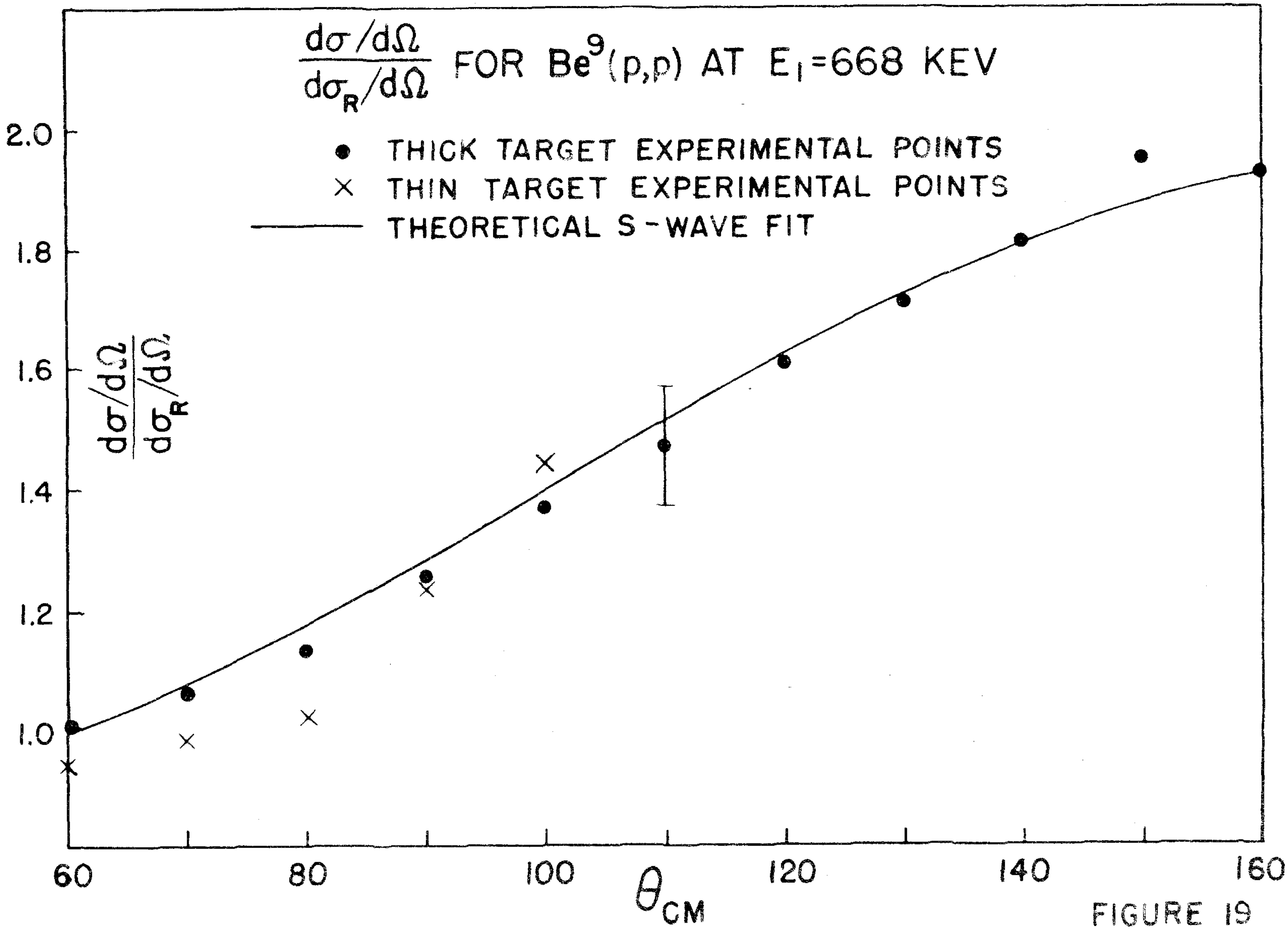
$\frac{d\sigma/d\Omega}{d\sigma_R/d\Omega}$ FOR $Be^9(p,p)$ AT E_1=668 KEV
● THICK TARGET EXPERIMENTAL POINTS
× THIN TARGET EXPERIMENTAL POINTS
THEORETICAL S-WAVE FIT
$\frac{d\sigma/d\Omega}{d\sigma_R/d\Omega}$
2.0
1.8
1.6
1.4
1.2
1.0
60
80
100
120
140
160
θ_{CM}

FIGURE 19

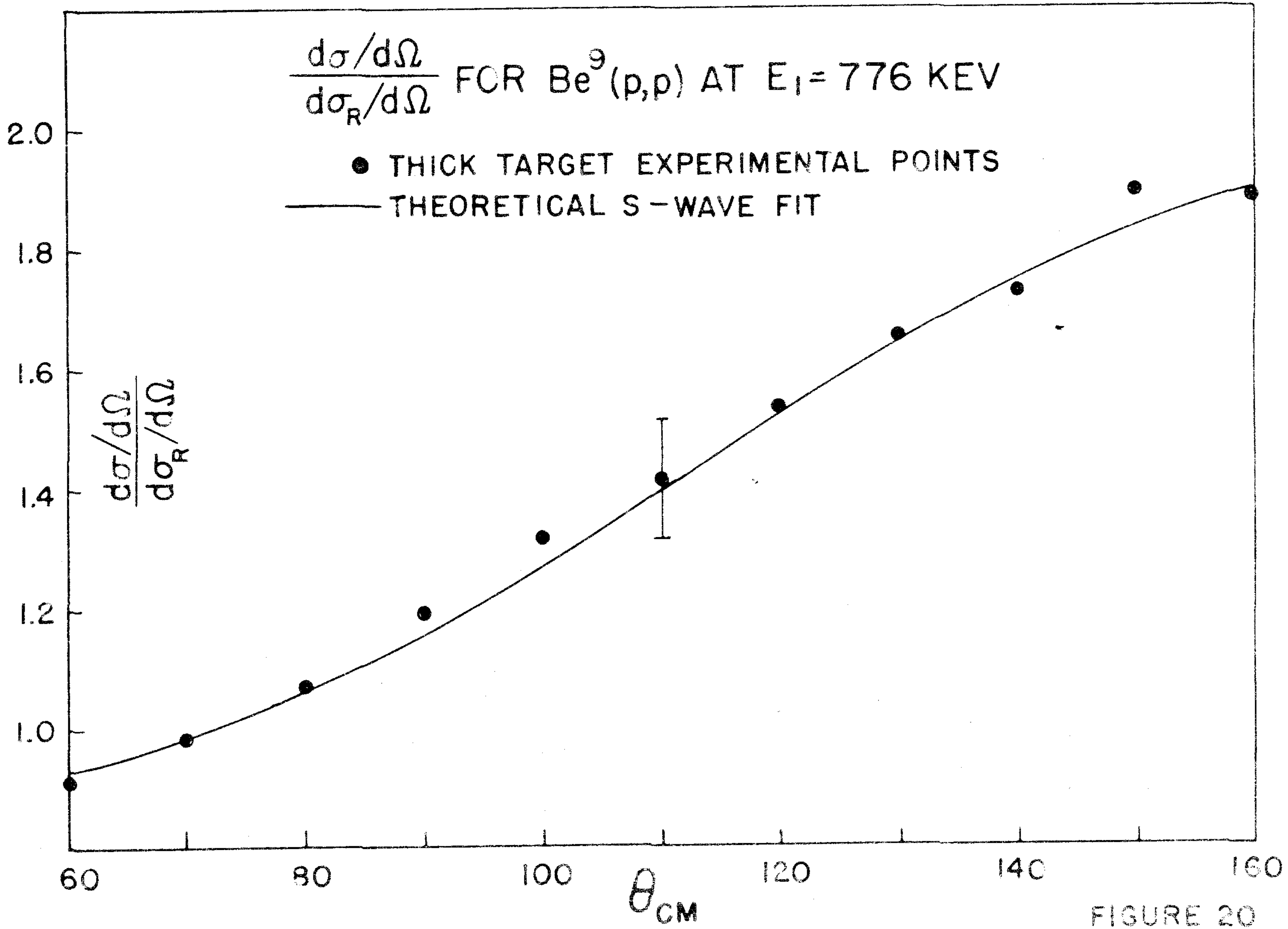
$\frac{d\sigma/d\Omega}{d\sigma_R/d\Omega}$ FOR $Be^9(p,p)$ AT $E_1 = 776$ KEV
● THICK TARGET EXPERIMENTAL POINTS
—— THEORETICAL S-WAVE FIT
$\frac{d\sigma/d\Omega}{d\sigma_R/d\Omega}$
2.0
1.8
1.6
1.4
1.2
1.0
60
80
100
120
140
160
θ_{CM}

FIGURE 20

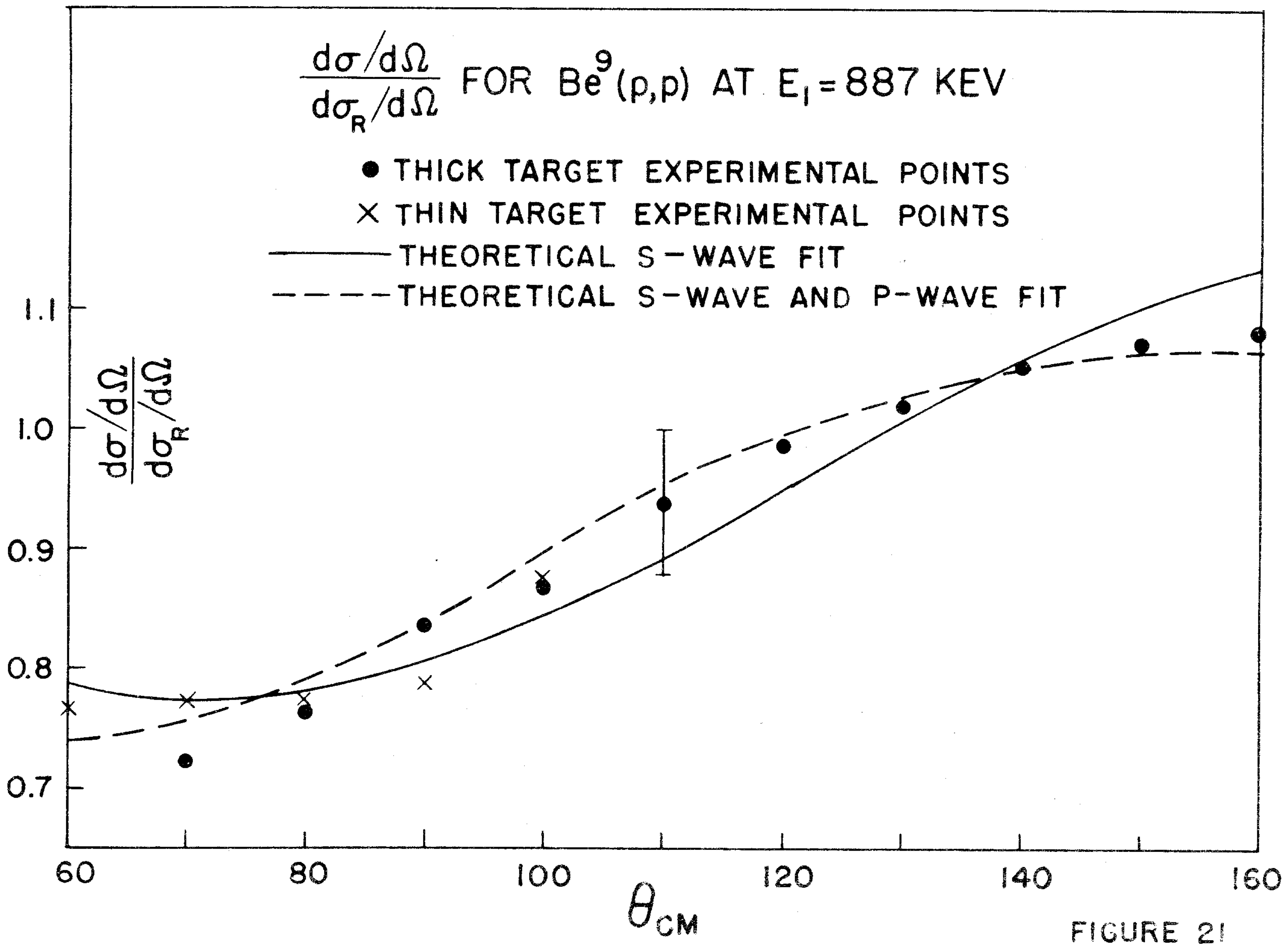
$\frac{d\sigma/d\Omega}{d\sigma_R/d\Omega}$ FOR $Be^9(p,p)$ AT $E_1 = 887$ KEV
● THICK TARGET EXPERIMENTAL POINTS
× THIN TARGET EXPERIMENTAL POINTS
——— THEORETICAL S-WAVE FIT
- - - - THEORETICAL S-WAVE AND P-WAVE FIT
$\frac{d\sigma/d\Omega}{d\sigma_R/d\Omega}$
1.1
1.0
0.9
0.8
0.7
60
80
100
120
140
160
θ_{CM}

FIGURE 21

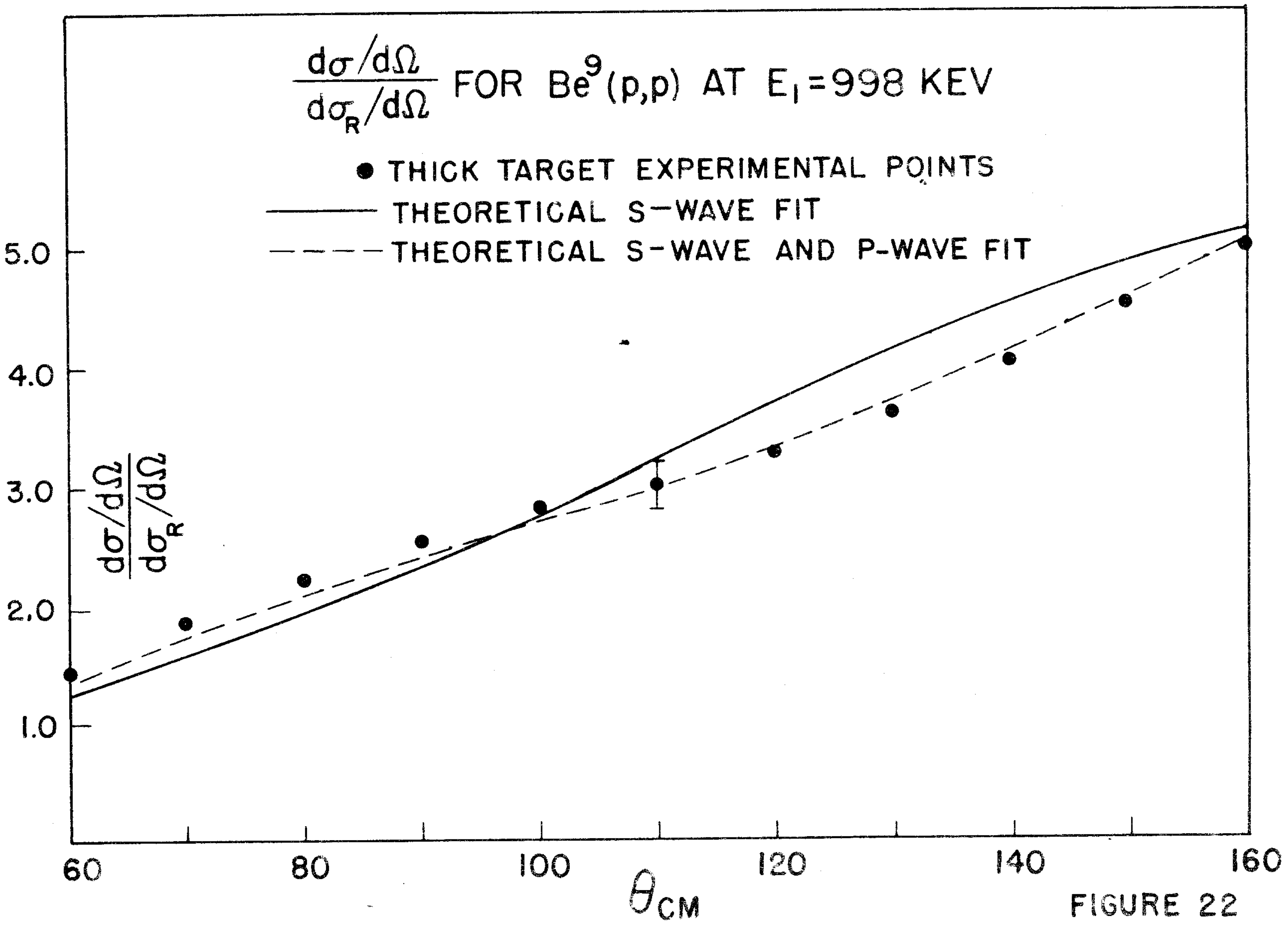
$\frac{d\sigma/d\Omega}{d\sigma_R/d\Omega}$ FOR $Be^9(p,p)$ AT $E_1 = 998$ KEV
● THICK TARGET EXPERIMENTAL POINTS
——— THEORETICAL S-WAVE FIT
- - - - THEORETICAL S-WAVE AND P-WAVE FIT
$\frac{d\sigma/d\Omega}{d\sigma_R/d\Omega}$
5.0
4.0
3.0
2.0
1.0
60
80
100
120
140
160
θ_{CM}

FIGURE 22

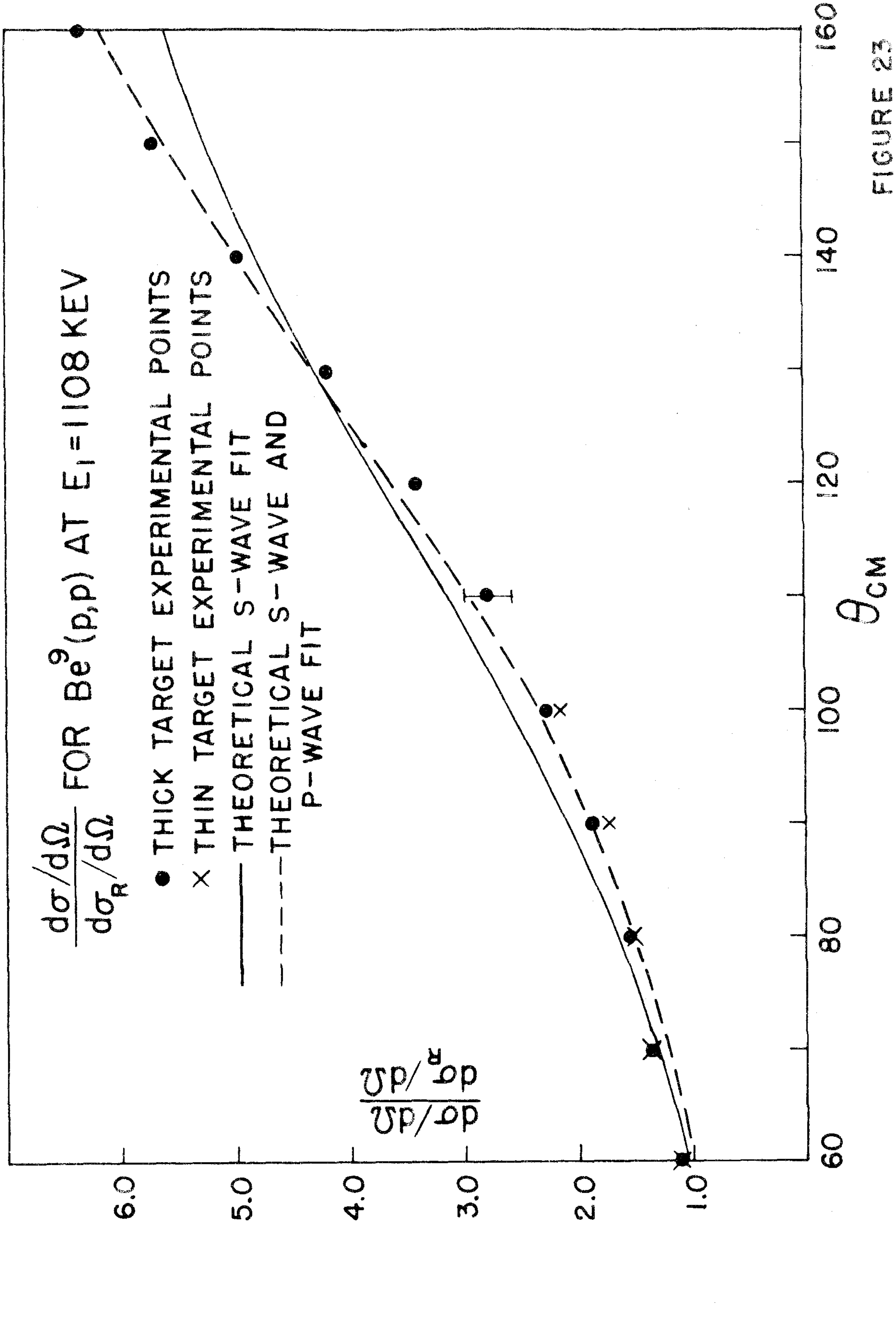
$\frac{d\sigma/d\Omega}{d\sigma_R/d\Omega}$ FOR $Be^9(p,p)$ AT $E_1 = 1108$ KEV
● THICK TARGET EXPERIMENTAL POINTS
× THIN TARGET EXPERIMENTAL POINTS
—— THEORETICAL S-WAVE FIT
- - - THEORETICAL S-WAVE AND P-WAVE FIT
$\frac{d\sigma/d\Omega}{d\sigma_R/d\Omega}$
6.0
5.0
4.0
3.0
2.0
1.0
60
80
100
120
140
160
θ_{CM}

FIGURE 23

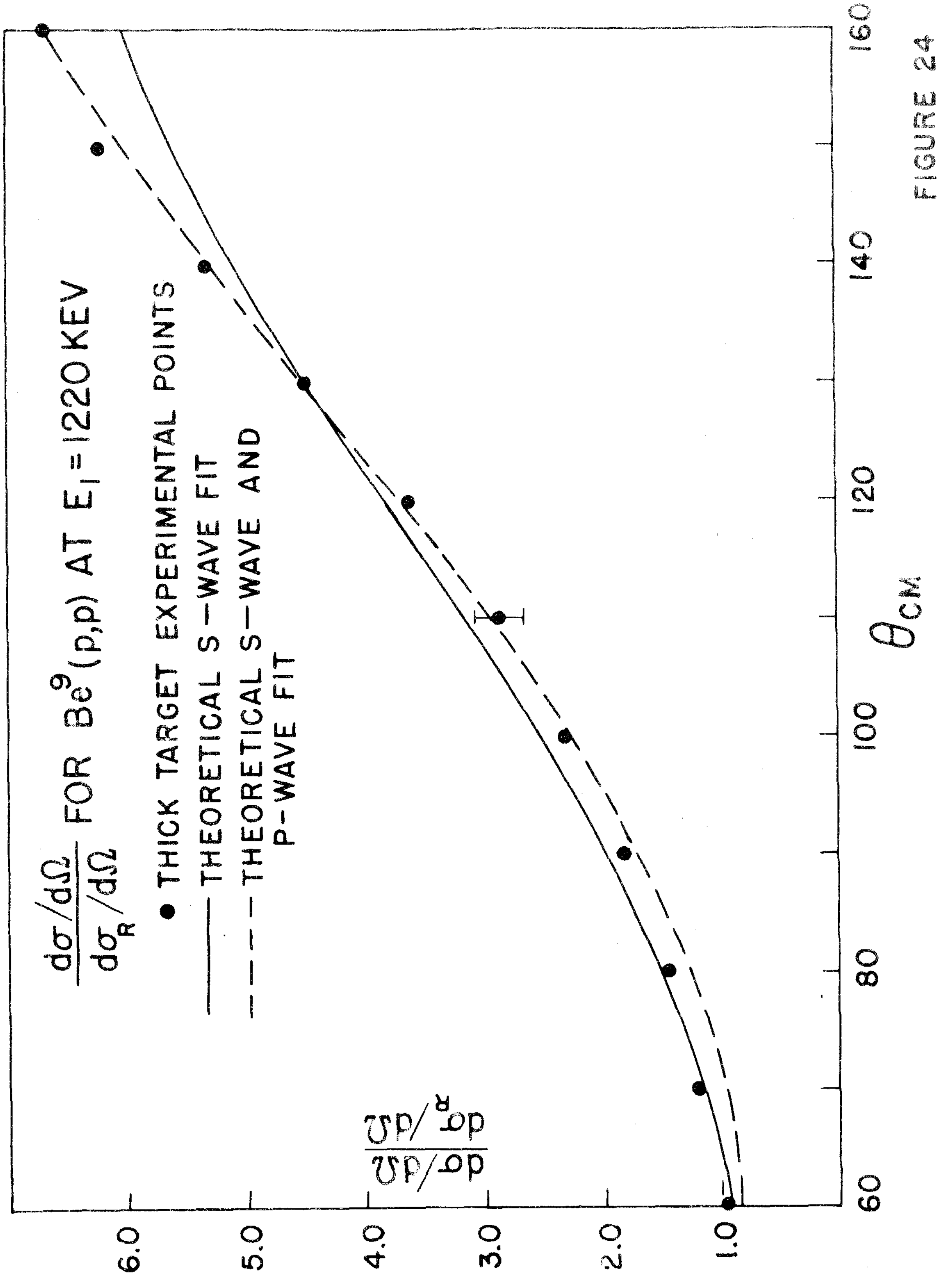
$\frac{d\sigma/d\Omega}{d\sigma_R/d\Omega}$ FOR $Be^9(p,p)$ AT $E_1 = 1220$ KEV
● THICK TARGET EXPERIMENTAL POINTS
—— THEORETICAL S—WAVE FIT
– – – THEORETICAL S—WAVE AND P—WAVE FIT
$\frac{d\sigma/d\Omega}{d\sigma_R/d\Omega}$
1.0
2.0
3.0
4.0
5.0
6.0
60
80
100
120
140
160
θ_{CM}

FIGURE 24

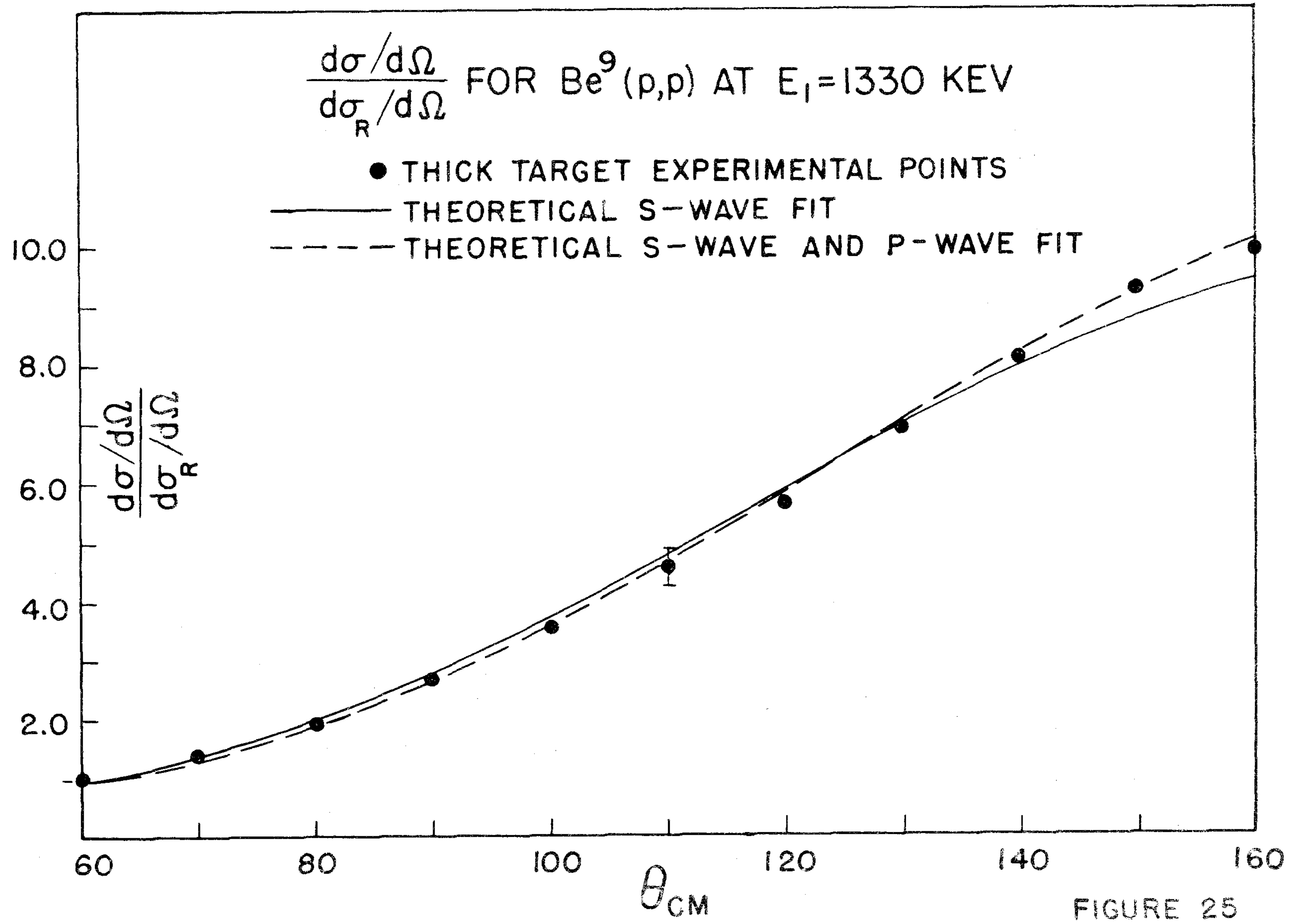
$\frac{d\sigma/d\Omega}{d\sigma_R/d\Omega}$ FOR $Be^9(p,p)$ AT E_1=1330 KEV
● THICK TARGET EXPERIMENTAL POINTS
——— THEORETICAL S-WAVE FIT
– – – – THEORETICAL S-WAVE AND P-WAVE FIT
$\frac{d\sigma/d\Omega}{d\sigma_R/d\Omega}$
10.0
8.0
6.0
4.0
2.0
60
80
100
120
140
160
θ_{CM}

FIGURE 25

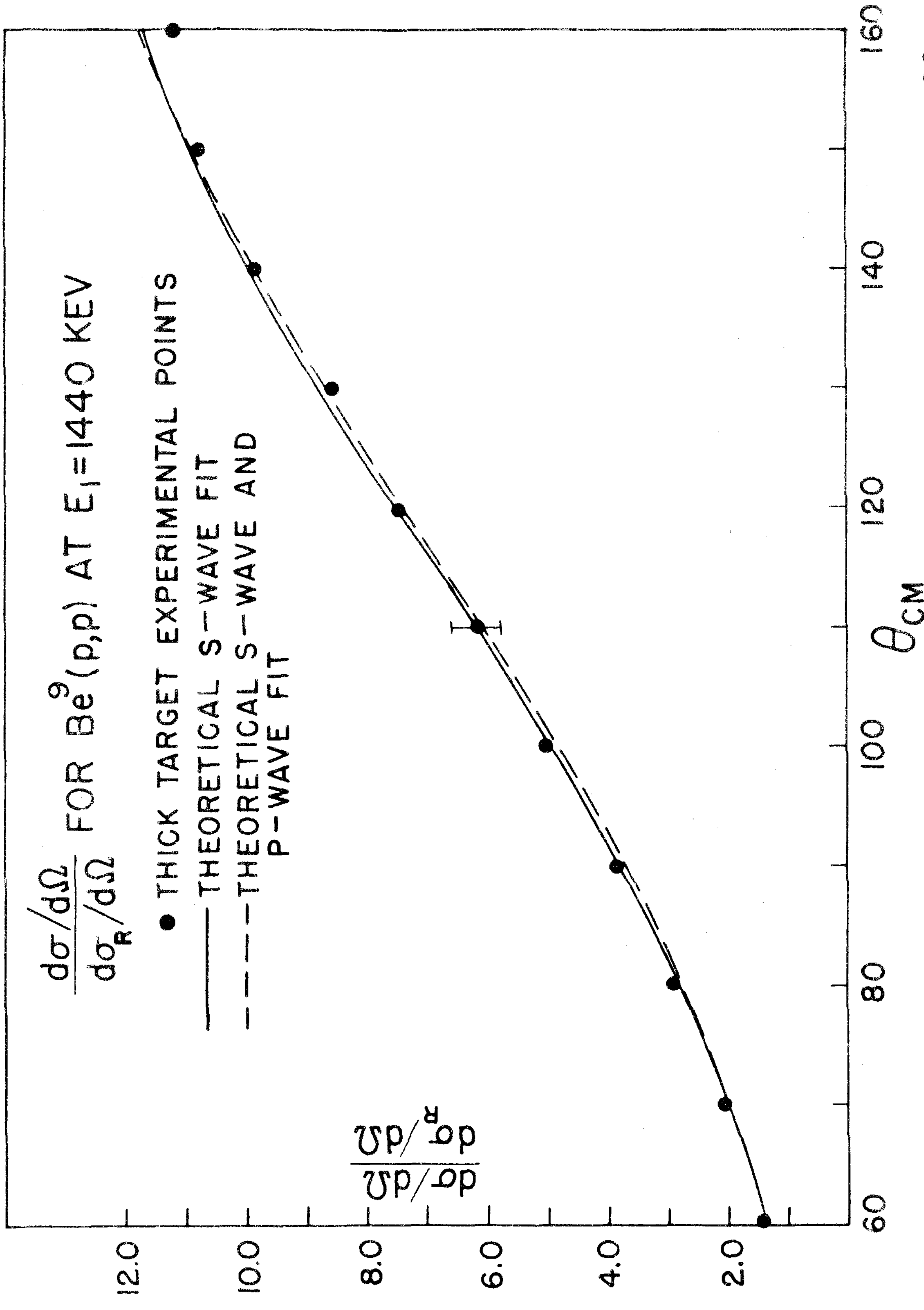

$\frac{d\sigma/d\Omega}{d\sigma_R/d\Omega}$ FOR $Be^9(p,p)$ AT $E_1=1440$ KEV

FIGURE 26

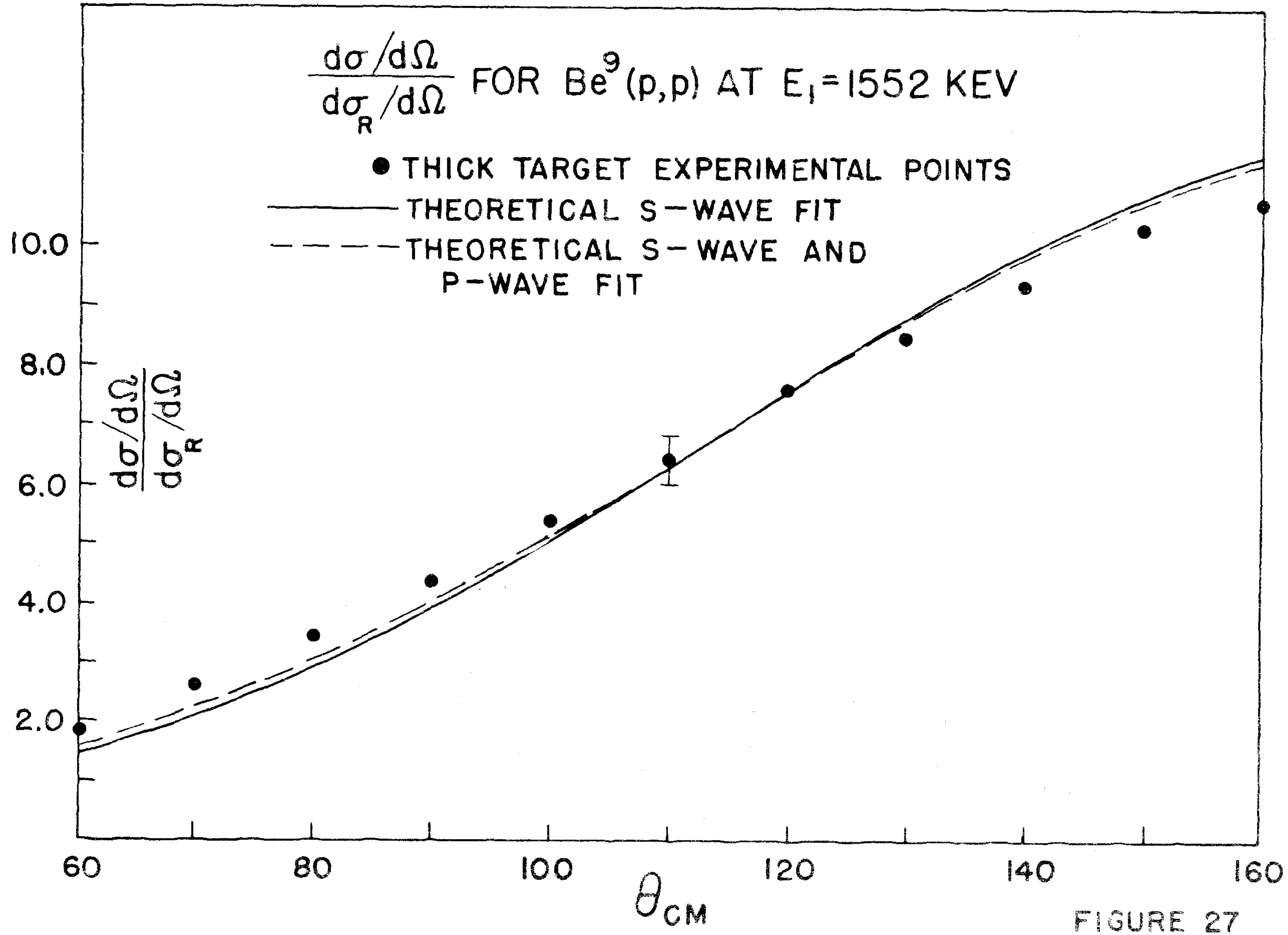
$\frac{d\sigma/d\Omega}{d\sigma_R/d\Omega}$ FOR $Be^9(p,p)$ AT E_1=1552 KEV
● THICK TARGET EXPERIMENTAL POINTS
—— THEORETICAL S-WAVE FIT
– – – THEORETICAL S-WAVE AND P-WAVE FIT
$\frac{d\sigma/d\Omega}{d\sigma_R/d\Omega}$
10.0
8.0
6.0
4.0
2.0
60
80
100
120
140
160
θ_{CM}

FIGURE 27

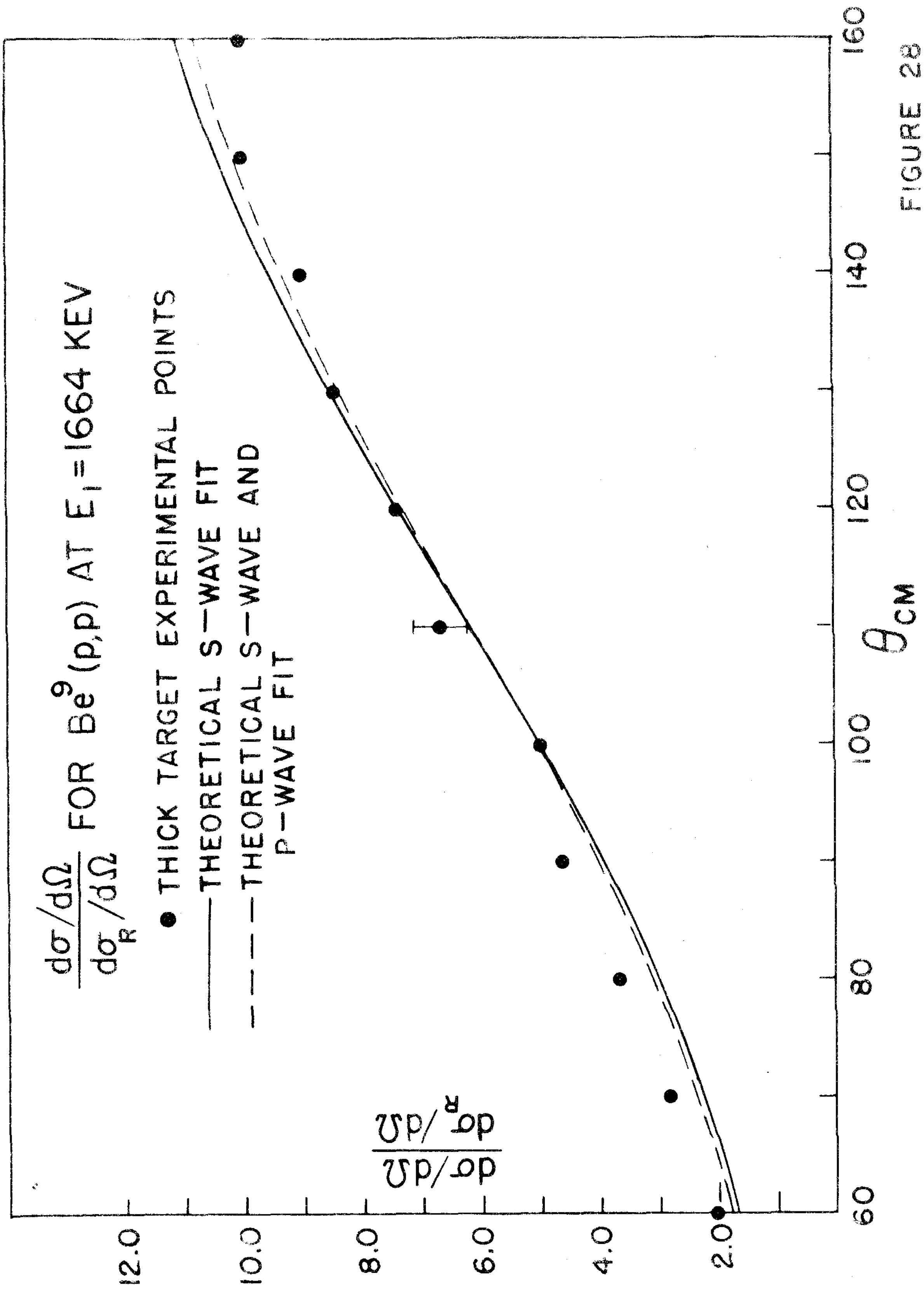
$\frac{d\sigma/d\Omega}{d\sigma_R/d\Omega}$ FOR $Be^9(p,p)$ AT $E_1 = 1664$ KEV
● THICK TARGET EXPERIMENTAL POINTS
—— THEORETICAL S—WAVE FIT
– – – THEORETICAL S—WAVE AND P—WAVE FIT
$\frac{d\sigma/d\Omega}{d\sigma_R/d\Omega}$
12.0
10.0
8.0
6.0
4.0
2.0
60
80
100
120
140
160
θ_{CM}

FIGURE 28

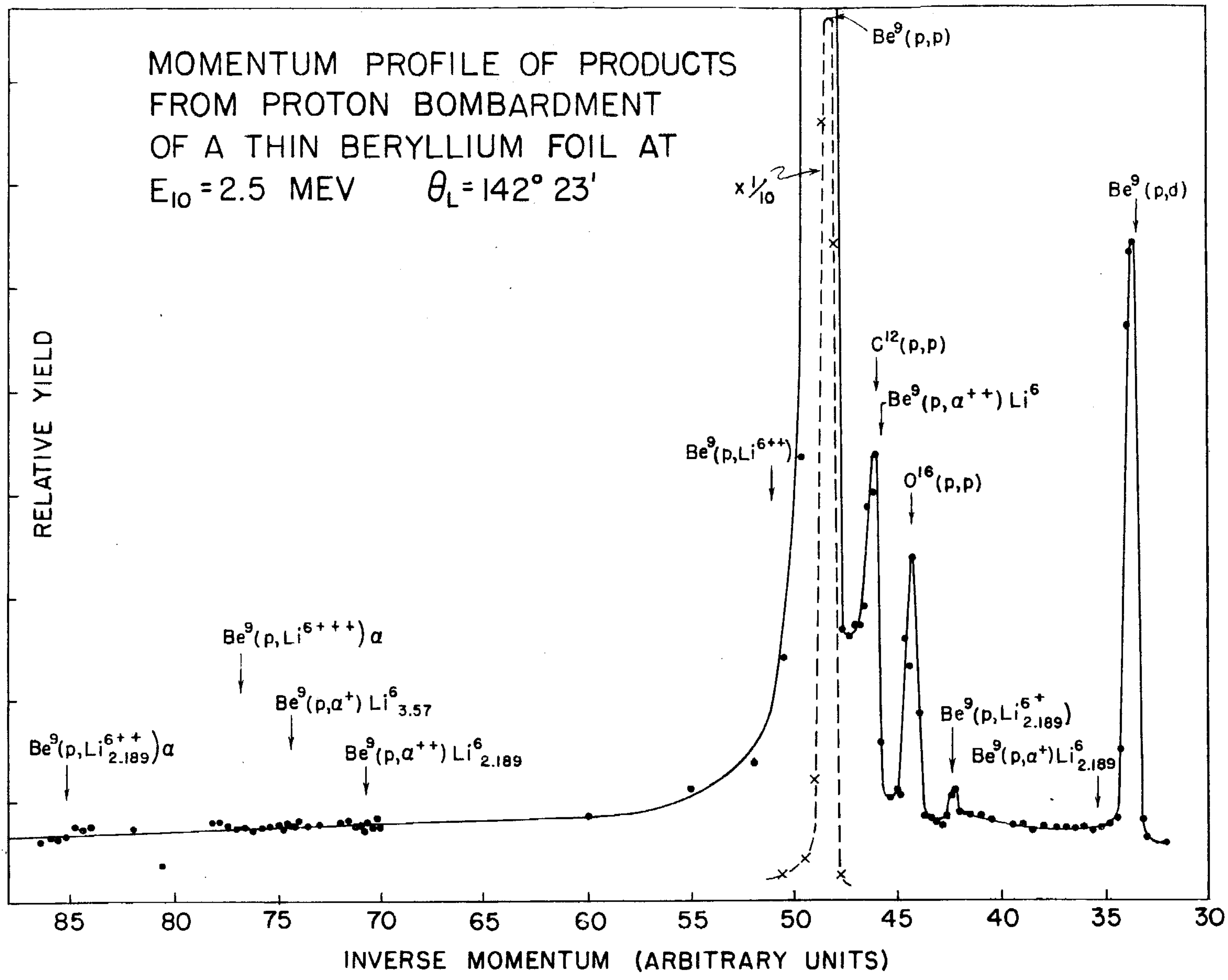
MOMENTUM PROFILE OF PRODUCTS FROM PROTON BOMBARDMENT OF A THIN BERYLLIUM FOIL AT
E_{10} = 2.5 MEV θ_L = 142° 23'
RELATIVE YIELD
8
6
4
2
INVERSE MOMENTUM (ARBITRARY UNITS)
85
80
75
70
65
60
55
50
45
40
35
30
× 1/10
$Be^9(p,p)$
$Be^9(p,d)$
$C^{12}(p,p)$
$Be^9(p,\alpha^{++})Li^6$
$O^{16}(p,p)$
$Be^9(p,Li^{6++})$
$Be^9(p,Li^{6+++})\alpha$
$Be^9(p,\alpha^+)Li^6_{3.57}$
$Be^9(p,\alpha^{++})Li^6_{2.189}$
$Be^9(p,Li^{6++}_{2.189})\alpha$
$Be^9(p,Li^{6+}_{2.189})$
$Be^9(p,\alpha^+)Li^6_{2.189}$

FIGURE 29

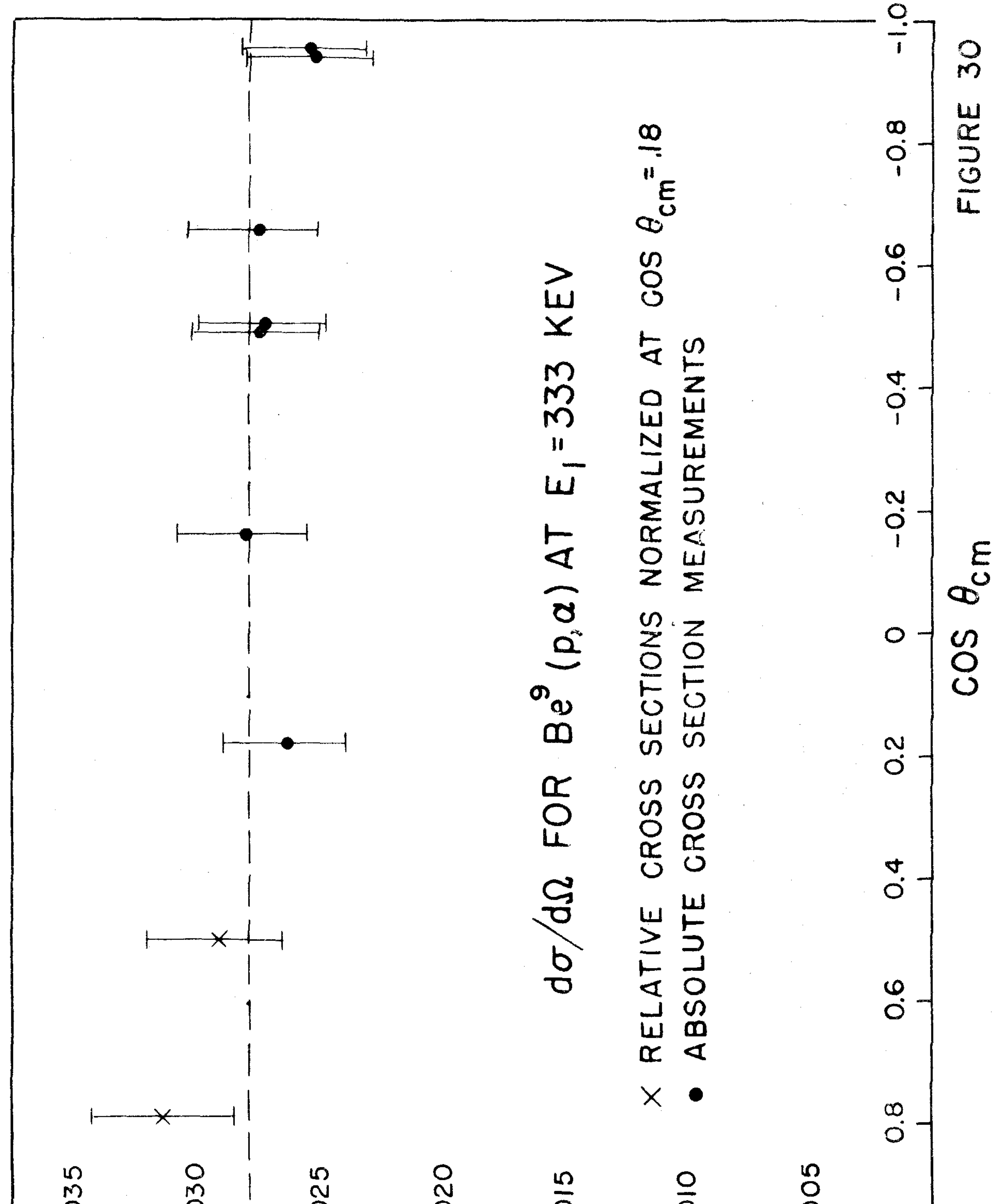
dσ/dΩ FOR Be^9(p,α) AT E$_1$=333 KEV
× RELATIVE CROSS SECTIONS NORMALIZED AT COS θ$_{cm}$=.18
● ABSOLUTE CROSS SECTION MEASUREMENTS
dσ/dΩ (BARNS/STERADIAN)
.035
.030
.025
.020
.015
.010
.005
COS θ$_{cm}$
1.0
0.8
0.6
0.4
0.2
0
-0.2
-0.4
-0.6
-0.8
-1.0

FIGURE 30

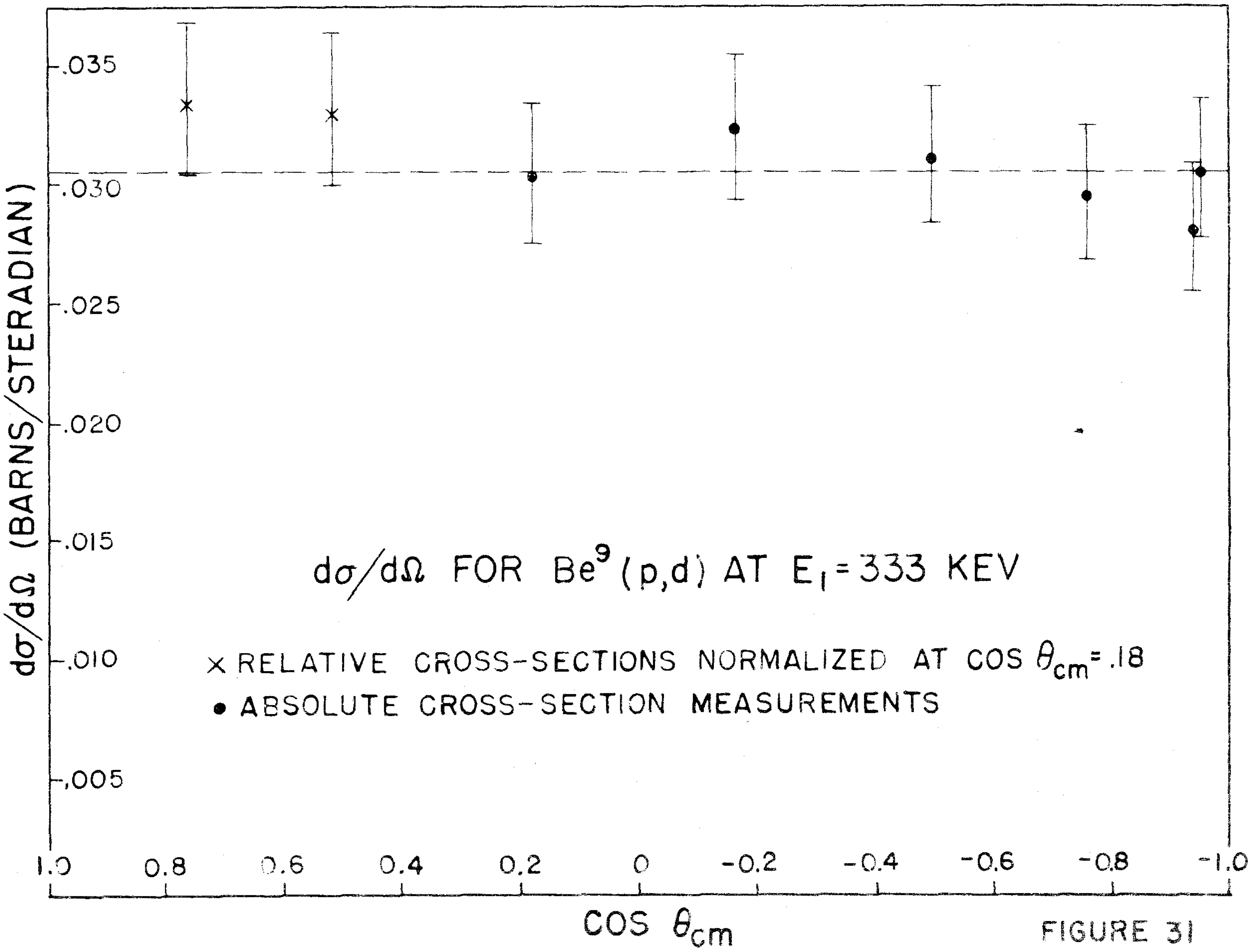
dσ/dΩ FOR Be^9(p,d) AT E$_1$=333 KEV
× RELATIVE CROSS-SECTIONS NORMALIZED AT COS θ_{cm}=.18
● ABSOLUTE CROSS-SECTION MEASUREMENTS
dσ/dΩ (BARNS/STERADIAN)
.035
.030
.025
.020
.015
.010
.005
1.0
0.8
0.6
0.4
0.2
0
-0.2
-0.4
-0.6
-0.8
-1.0
COS θ_{cm}

FIGURE 31

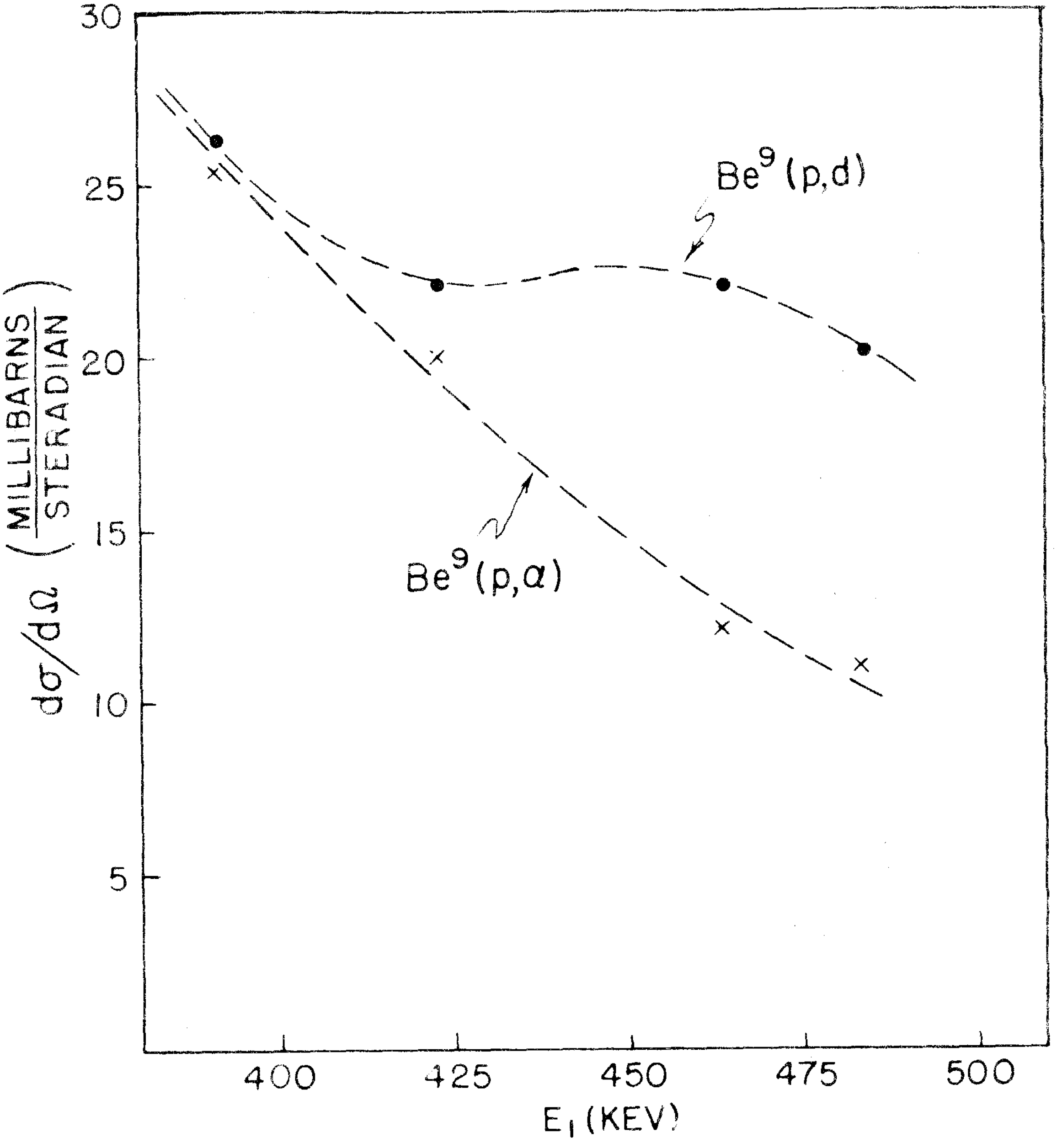

EXCITATION CURVES FOR $Be^9(p,d)$ AND $Be^9(p,\alpha)$ AT $\theta_L = 138°$

FIGURE 32

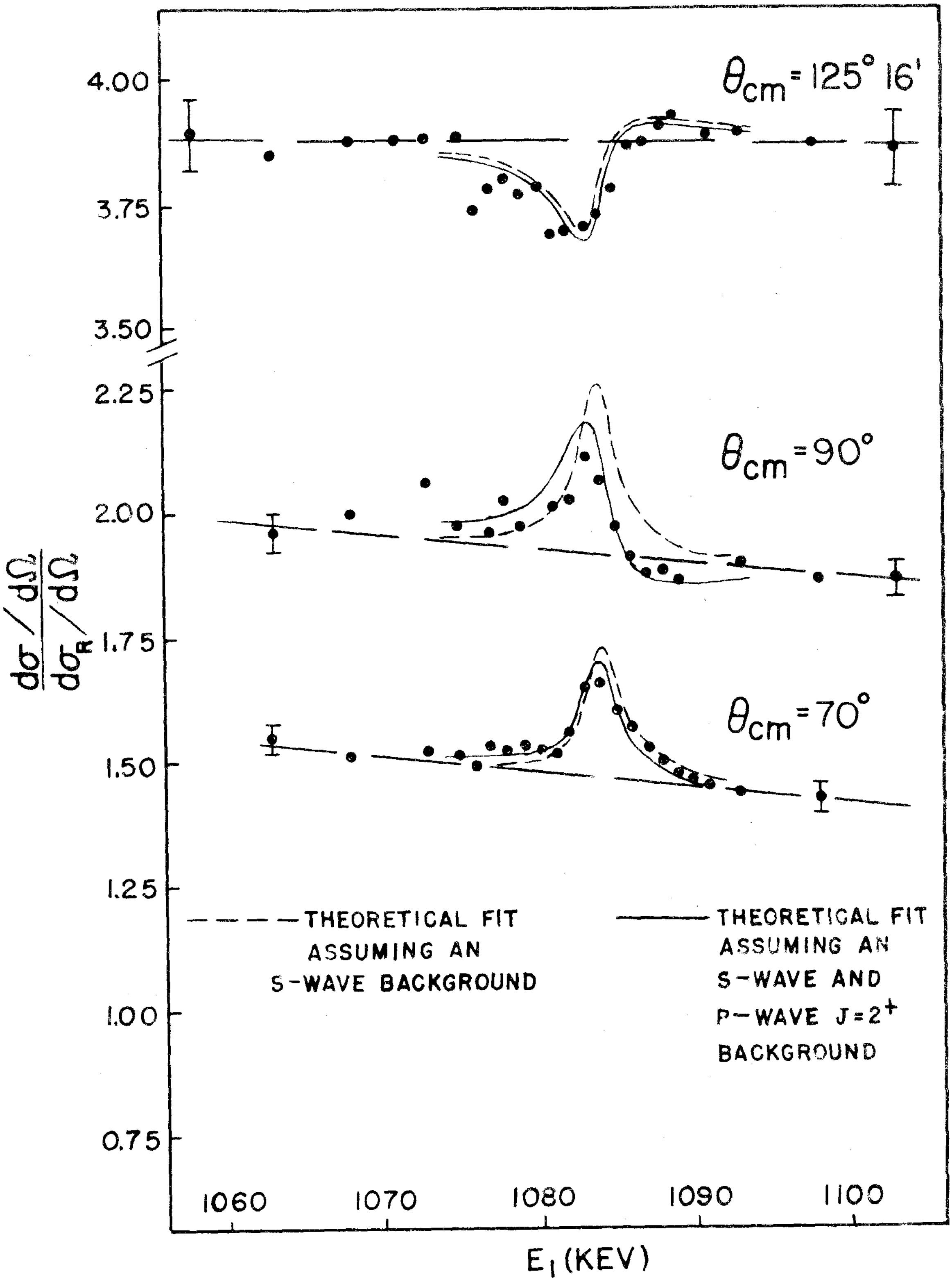

$\frac{d\sigma/d\Omega}{d\sigma_R/d\Omega}$ FOR $Be^9(p,p)$

(NOTE SUPPRESSED ZERO OF ORDINATE SCALE)

FIGURE 33

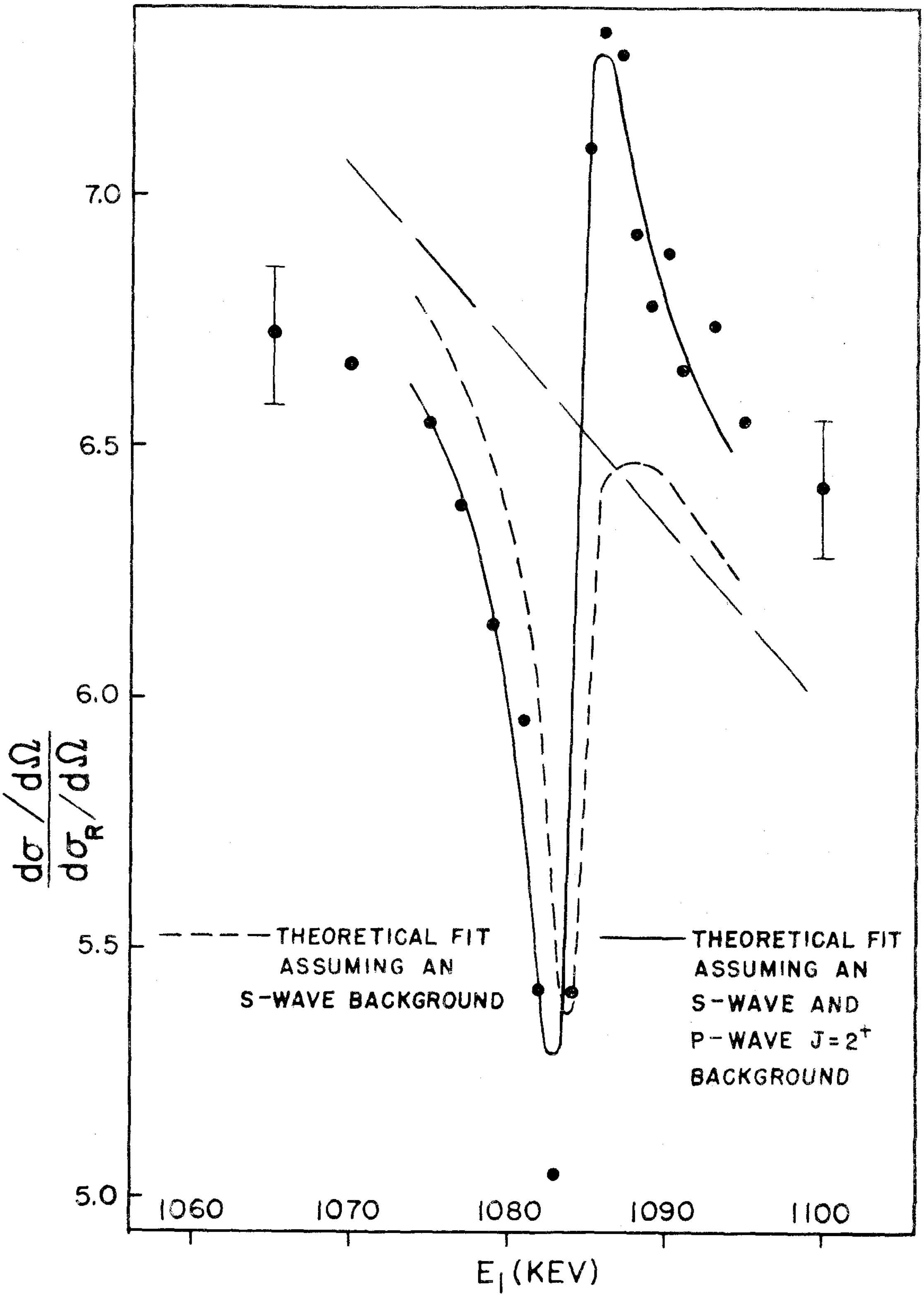

$\frac{d\sigma/d\Omega}{d\sigma_R/d\Omega}$ FOR $Be^9(p,p)$ AT $\theta_{cm} = 160° 59'$

(NOTE SUPPRESSED ZERO OF ORDINATE SCALE)

FIGURE 34

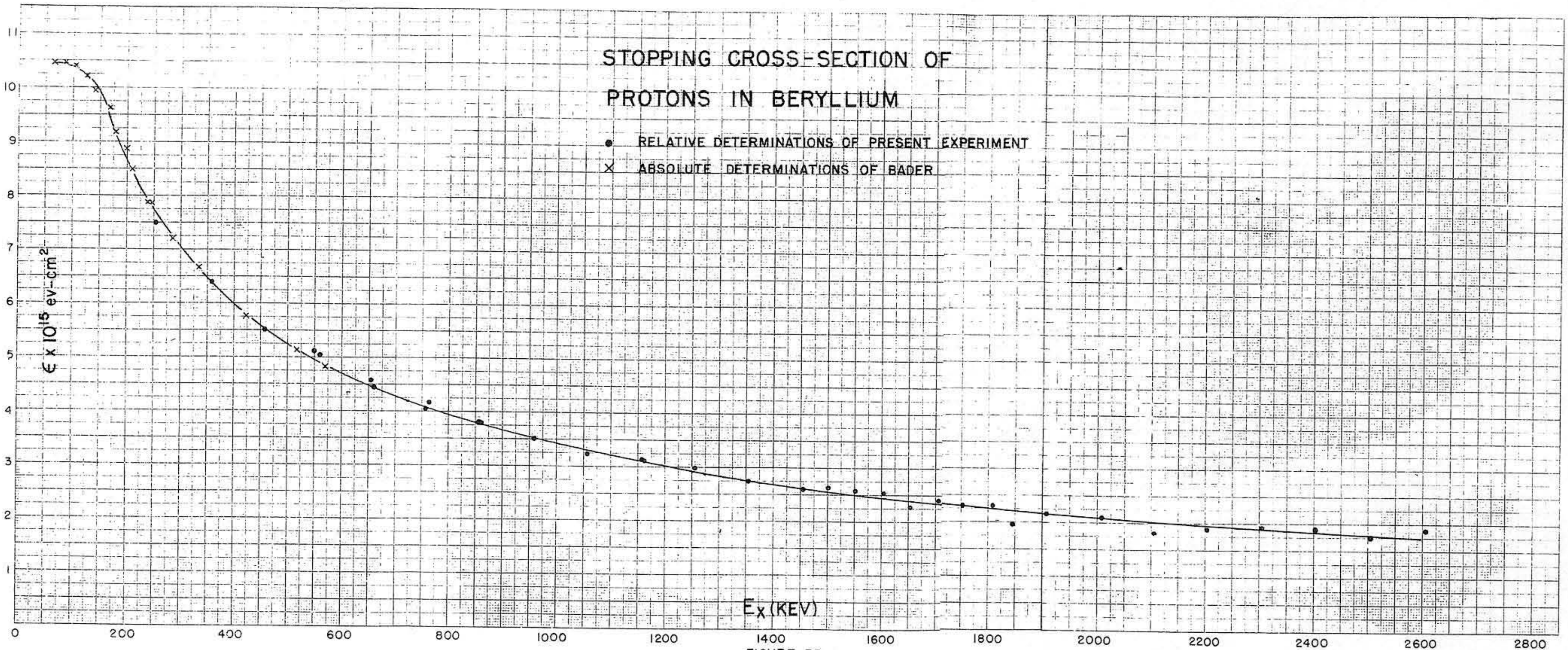
STOPPING CROSS-SECTION OF
PROTONS IN BERYLLIUM
● RELATIVE DETERMINATIONS OF PRESENT EXPERIMENT
× ABSOLUTE DETERMINATIONS OF BADER
$\epsilon \times 10^{15}$ ev-cm^2
11
10
9
8
7
6
5
4
3
2
1
0
200
400
600
800
1000
1200
1400
1600
1800
2000
2200
2400
2600
2800
E_x (KEV)

FIGURE 35

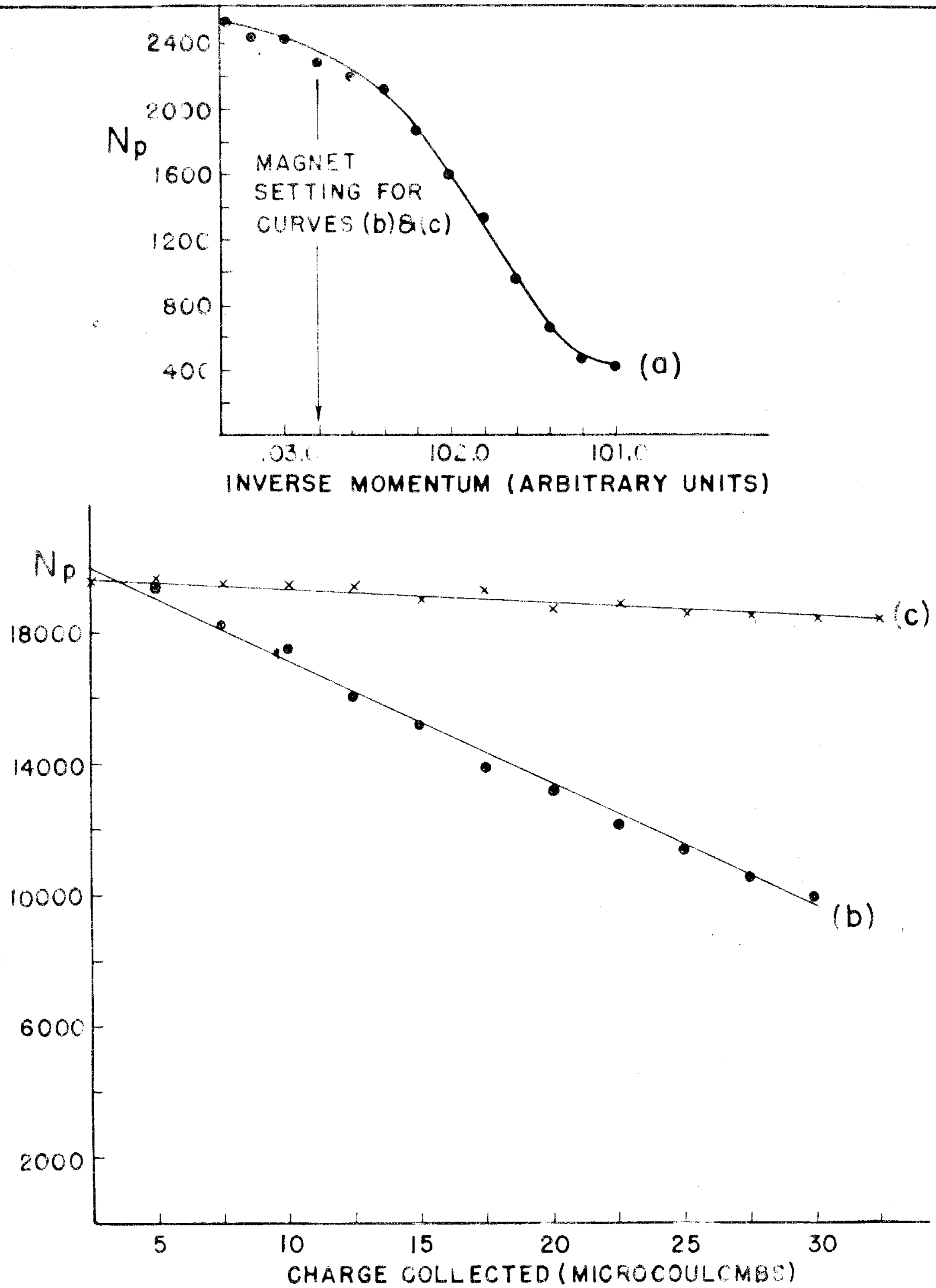

SURFACE CONTAMINATION OF BERYLLIUM TARGET AT 200 KEV BOMBARDING ENERGY

CURVE (a) DEPTH IN TARGET AT WHICH CURVES (b) & (c) WERE RUN.

CURVE (b) NUMBER OF PROTONS PER RUN FOR UNHEATED TARGET.

CURVE (c) NUMBER OF PROTONS PER RUN FOR TARGET AT 150° C.

FIGURE 36

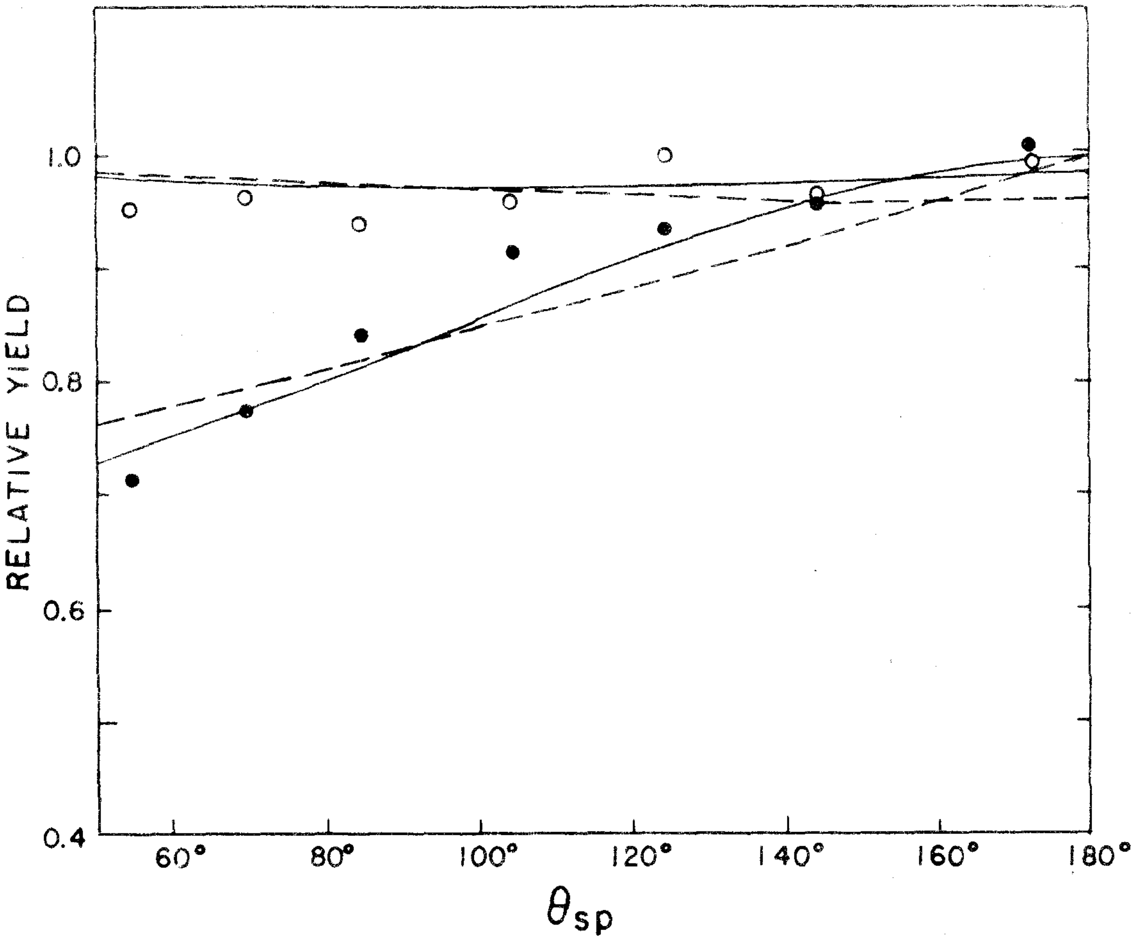

YIELD FROM SCRATCHED COPPER TARGETS RELATIVE TO THAT FROM A SMOOTH SURFACE

● RELATIVE YIELD FOR A VERTICALLY SCRATCHED SURFACE

○ RELATIVE YIELD FOR A HORIZONTALLY SCRATCHED SURFACE

------ THEORETICAL CURVES FOR A UNIFORM DISTRIBUTION OF ϕ, THE HALF INTERIOR ANGLE OF A SCRATCH

——— THEORETICAL CURVES FOR A GAUSSIAN DISTRIBUTION OF ϕ ABOUT A MEAN ANGLE $\pi/4$ WITH VARIANCE $\pi/8$

FIGURE 37

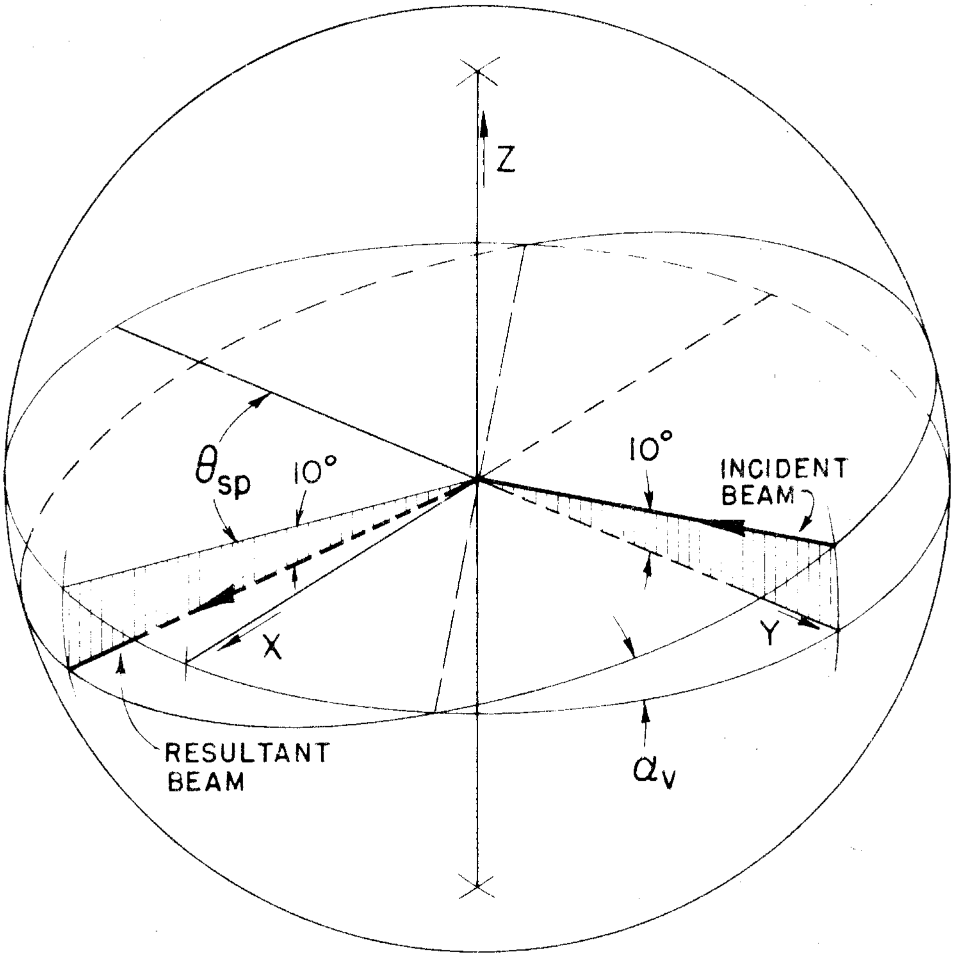

GEOMETRY OF THE SCATTERING PROCESS ILLUSTRATING THE RELATIONSHIP OF THE HORIZONTAL PLANE AND THE BEAM PLANE

FIGURE 38

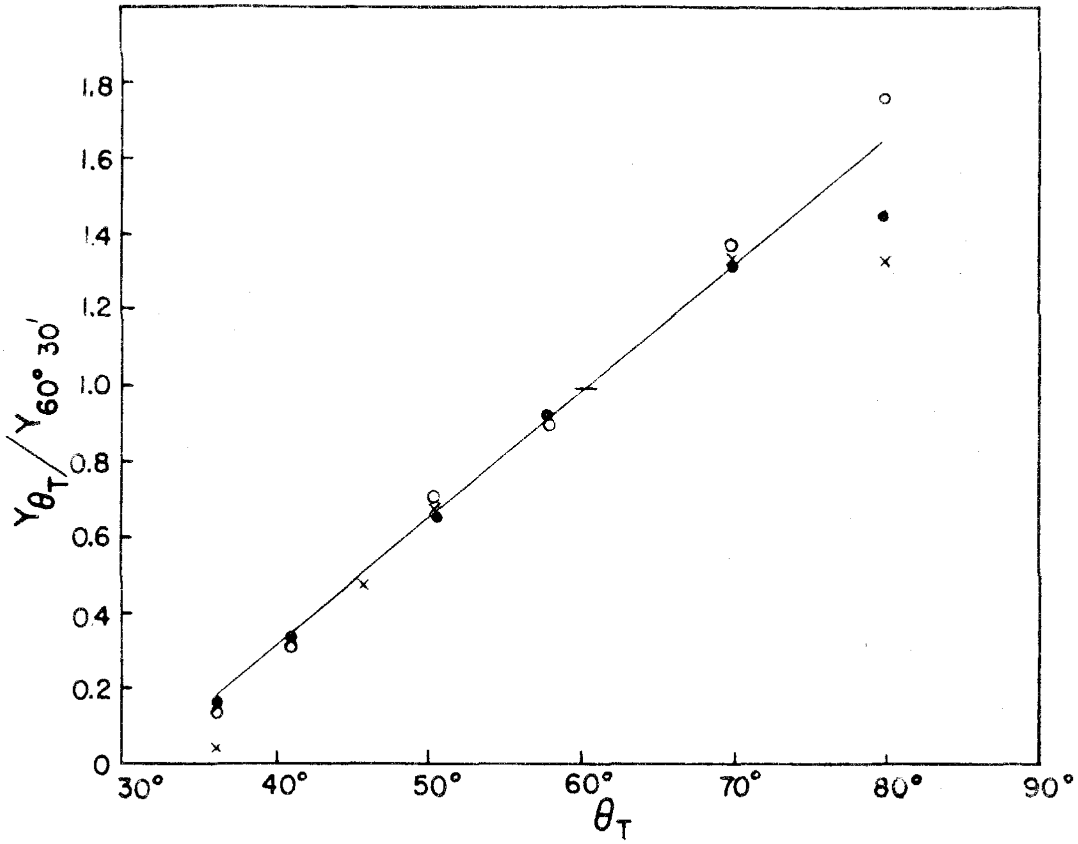

VARIATION OF YIELD WITH TARGET ANGLE FOR SCRATCHED AND SMOOTH COPPER TARGETS
$E_1 = 675$ KEV $\theta_{LAB} = 59°$

● VERTICAL SCRATCHES

○ HORIZONTAL SCRATCHES

× SMOOTH SURFACE

——— THEORETICAL CURVE FOR A SMOOTH SURFACE

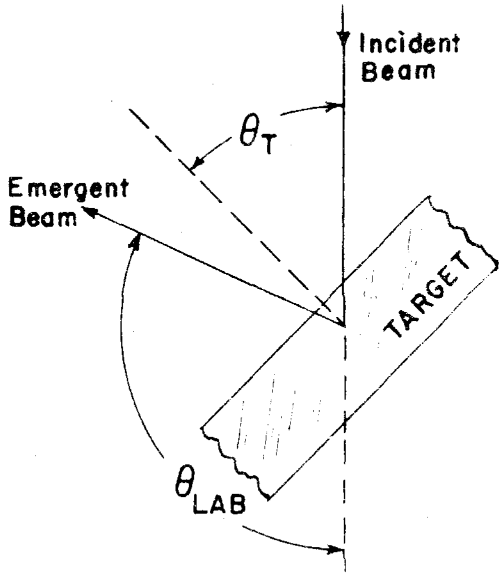

FIGURE 39

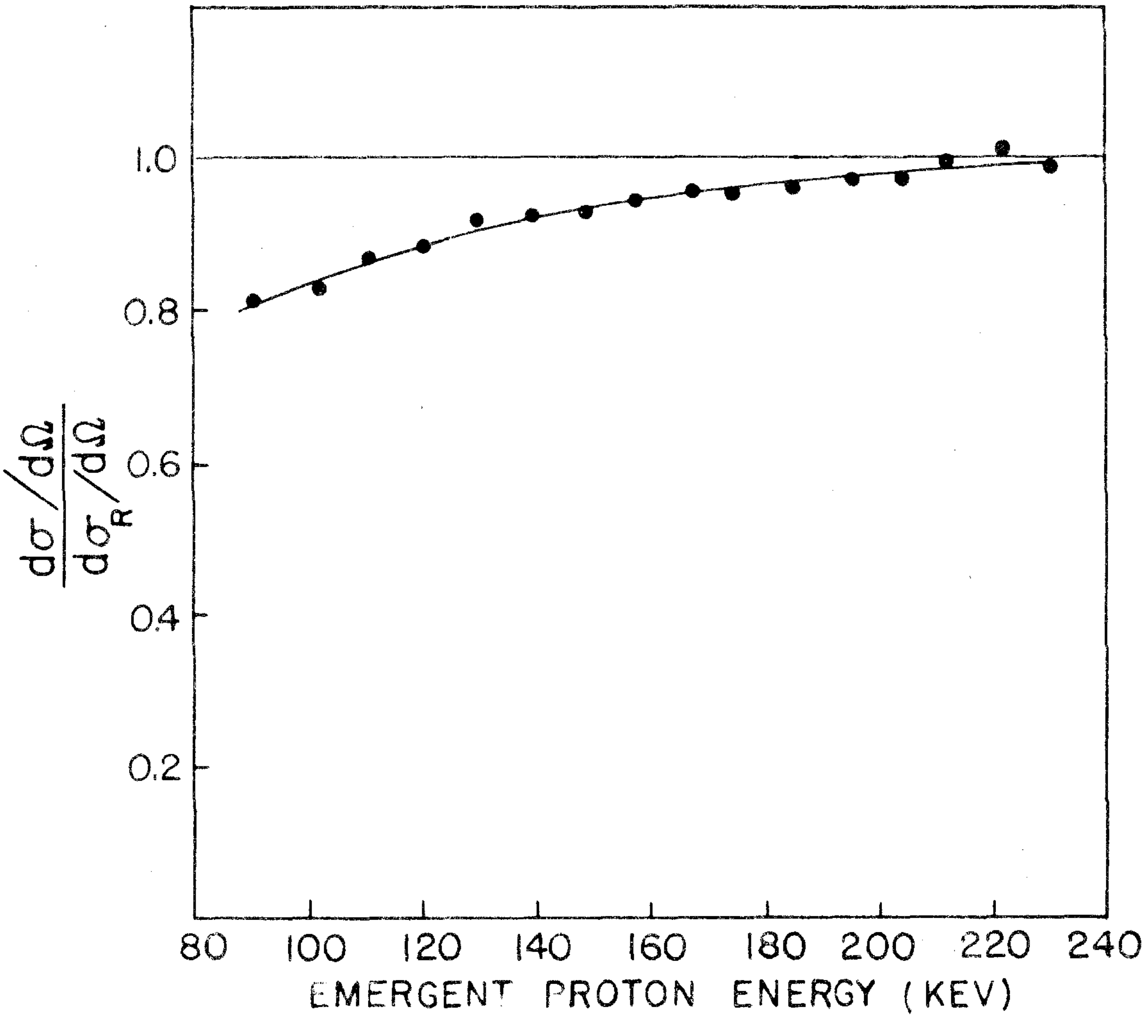

CHARGE NEUTRALIZATION OF PROTONS AS DETERMINED FROM THE LOW ENERGY ELASTIC SCATTERING OF PROTONS BY COPPER

FIGURE 40

	1,1	1,0	1,-1	2,2	2,1	2,0	2,-1	2,-2
1,1	$+f_c+f^1_{11ss}Y^0_0+\sqrt{\tfrac{1}{10}}f^1_{11sd}Y^0_2$ $+\sqrt{\tfrac{1}{10}}f^1_{11ds}Y^0_0+\tfrac{1}{10}f^1_{11dd}Y^0_2$ $+\tfrac{1}{2}f^2_{11dd}Y^0_2+\tfrac{1}{2}f^2_{11pp}Y^0_1$	$-\sqrt{\tfrac{3}{10}}f^1_{11sd}Y^1_2-\tfrac{\sqrt{3}}{10}f^1_{11dd}Y^1_2$ $-\tfrac{1}{2\sqrt{3}}f^2_{11dd}Y^1_2$ $+\tfrac{1}{2}f^2_{11pp}Y^1_1$	$+\sqrt{\tfrac{3}{5}}f^1_{11sd}Y^2_2$ $+\sqrt{\tfrac{3}{50}}f^1_{11dd}Y^2_2$ $-\sqrt{\tfrac{1}{6}}f^2_{11dd}Y^2_2$	$+\sqrt{\tfrac{1}{5}}f^1_{12sd}Y^{-1}_2+\sqrt{\tfrac{1}{50}}f^1_{12dd}Y^{-1}_2$ $-\sqrt{\tfrac{3}{14}}f^2_{12dd}Y^{-1}_2$	$-\sqrt{\tfrac{3}{10}}f^1_{12sd}Y^0_2-\tfrac{\sqrt{3}}{10}f^1_{12dd}Y^0_2$ $-\sqrt{\tfrac{1}{2}}f^2_{12ds}Y^0_0+\sqrt{\tfrac{1}{28}}f^2_{12dd}Y^0_2$	$+\sqrt{\tfrac{3}{10}}f^1_{12sd}Y^1_2+\tfrac{\sqrt{3}}{10}f^1_{12dd}Y^1_2$ $+\sqrt{\tfrac{1}{28}}f^2_{12dd}Y^1_2$	$-\sqrt{\tfrac{1}{5}}f^1_{12sd}Y^2_2-\sqrt{\tfrac{1}{50}}f^1_{12dd}Y^2_2$ $-\sqrt{\tfrac{3}{14}}f^2_{12dd}Y^2_2$	
1,0	$+\sqrt{\tfrac{3}{10}}f^1_{11sd}Y^{-1}_2$ $-\sqrt{\tfrac{3}{25}}f^1_{11dd}Y^{-1}_2$ $+\tfrac{1}{3}f^2_{11pp}Y^{-1}_1$ $-\tfrac{1}{3}f^0_{11pp}Y^{-1}_1$	$+f_c+f^1_{11ss}Y^0_0$ $-\sqrt{\tfrac{3}{5}}f^1_{11sd}Y^0_2-\sqrt{\tfrac{2}{5}}f^1_{11ds}Y^0_0$ $+\tfrac{2}{5}f^1_{11dd}Y^0_2+\tfrac{2}{3}f^2_{11pp}Y^0_1$ $+\tfrac{1}{3}f^0_{11pp}Y^0_1$	$+\sqrt{\tfrac{3}{10}}f^1_{11sd}Y^1_2$ $-\sqrt{\tfrac{3}{25}}f^1_{11dd}Y^1_2$ $+\tfrac{1}{3}f^2_{11pp}Y^1_1$ $-\tfrac{1}{3}f^0_{11pp}Y^1_1$	$-\sqrt{\tfrac{2}{5}}f^1_{12sd}Y^{-2}_2$ $+\tfrac{2}{5}f^1_{12dd}Y^{-2}_2$	$+\sqrt{\tfrac{1}{10}}f^1_{12sd}Y^{-1}_2$ $-\sqrt{\tfrac{1}{25}}f^1_{12dd}Y^{-1}_2$		$-\sqrt{\tfrac{1}{10}}f^1_{12sd}Y^1_2+\sqrt{\tfrac{1}{25}}f^1_{12dd}Y^1_2$	$+\sqrt{\tfrac{2}{5}}f^1_{12sd}Y^2_2$ $-\tfrac{2}{5}f^1_{12dd}Y^2_2$
1,-1	SAME AS ROW 1,1 COLUMN 1,-1	SAME AS ROW 1,1 COLUMN 1,0	SAME AS ROW 1,1 COLUMN 1,1	SAME AS ROW 1,1 COLUMN 2,-2	SAME AS ROW 1,1 COLUMN 2,-1	SAME AS ROW 1,1 COLUMN 2,0	SAME AS ROW 1,1 COLUMN 2,1	SAME AS ROW 1,1 COLUMN 2,2
2,2	$-\sqrt{\tfrac{1}{3}}f^2_{21sd}Y^1_2$ $-\sqrt{\tfrac{2}{21}}f^2_{21dd}Y^1_2$	$+\sqrt{\tfrac{2}{3}}f^2_{21sd}Y^2_2$ $+\sqrt{\tfrac{4}{21}}f^2_{21dd}Y^2_2$		$+f_c+f^2_{22ss}Y^0_0$ $+\sqrt{\tfrac{2}{7}}f^2_{22sd}Y^0_2$ $+\sqrt{\tfrac{2}{7}}f^2_{22ds}Y^0_0+\tfrac{2}{7}f^2_{22dd}Y^0_2$	$-\sqrt{\tfrac{3}{7}}f^2_{22sd}Y^1_2-\tfrac{\sqrt{6}}{7}f^2_{22dd}Y^1_2$	$+\sqrt{\tfrac{2}{7}}f^2_{22sd}Y^2_2$ $+\tfrac{2}{7}f^2_{22dd}Y^2_2$		
2,1	$-\sqrt{\tfrac{1}{2}}f^2_{21sd}Y^0_2+\sqrt{\tfrac{1}{28}}f^2_{21dd}Y^0_2$ $-\sqrt{\tfrac{3}{10}}f^1_{21ds}Y^0_0-\tfrac{\sqrt{3}}{10}f^1_{21dd}Y^0_2$	$+\sqrt{\tfrac{1}{6}}f^2_{21sd}Y^1_2-\tfrac{1}{\sqrt{84}}f^2_{21dd}Y^1_2$ $+\tfrac{3}{10}f^1_{21dd}Y^1_2$	$+\sqrt{\tfrac{1}{3}}f^2_{21sd}Y^2_2-\sqrt{\tfrac{1}{42}}f^2_{21dd}Y^2_2$ $-\tfrac{3}{5\sqrt{2}}f^1_{21dd}Y^2_2$	$+\sqrt{\tfrac{3}{7}}f_{22sd}Y^{-1}_2$ $-\tfrac{\sqrt{6}}{14}f_{22dd}Y^{-1}_2$ $-\tfrac{\sqrt{6}}{10}f^1_{22dd}Y^{-1}_2$	$+f_c+f^2_{22ss}Y^0_0-\sqrt{\tfrac{1}{14}}f^2_{22sd}Y^0_2$ $-\sqrt{\tfrac{1}{14}}f^2_{22ds}Y^0_0+\tfrac{1}{14}f^2_{22dd}Y^0_2$ $+\tfrac{3}{10}f^1_{22dd}Y^0_2$	$-\sqrt{\tfrac{1}{14}}f^2_{22sd}Y^1_2$ $+\tfrac{1}{14}f^2_{22dd}Y^1_2$ $-\tfrac{3}{10}f^1_{22dd}Y^1_2$	$+\sqrt{\tfrac{3}{7}}f^2_{22sd}Y^2_2$ $-\tfrac{\sqrt{6}}{14}f^2_{22dd}Y^2_2$ $+\tfrac{\sqrt{6}}{10}f^1_{22dd}Y^2_2$	
2,0	$-\sqrt{\tfrac{1}{2}}f^2_{21sd}Y^{-1}_2$ $+\sqrt{\tfrac{1}{7}}f^2_{21dd}Y^1_2$		$+\sqrt{\tfrac{1}{2}}f^2_{21sd}Y^1_2$ $-\sqrt{\tfrac{1}{7}}f^2_{21dd}Y^1_2$	$+\sqrt{\tfrac{2}{7}}f^2_{22sd}Y^{-2}_2$ $-\tfrac{2}{7}f^2_{22dd}Y^{-2}_2$	$+\sqrt{\tfrac{1}{14}}f^2_{22sd}Y^{-1}_2$ $-\tfrac{2}{14}f^2_{22dd}Y^{-1}_2$	$+f_c+f^2_{22ss}Y^0_0-\sqrt{\tfrac{2}{7}}f^2_{22sd}Y^0_2$ $-\sqrt{\tfrac{2}{7}}f^2_{22ds}Y^0_0+\tfrac{2}{7}f^2_{22dd}Y^0_2$	$+\sqrt{\tfrac{1}{14}}f^2_{22sd}Y^1_2$ $-\tfrac{2}{14}f^2_{22dd}Y^1_2$	$+\sqrt{\tfrac{2}{7}}f^2_{22sd}Y^2_2$ $-\tfrac{2}{7}f^2_{22dd}Y^2$
2,-1	SAME AS ROW 2,1 COLUMN 1,-1	SAME AS ROW 2,1 COLUMN 1,0	SAME AS ROW 2,1 COLUMN 1,1	SAME AS ROW 2,1 COLUMN 2,-2	SAME AS ROW 2,1 COLUMN 2,-1	SAME AS ROW 2,1 COLUMN 2,0	SAME AS ROW 2,1 COLUMN 2,1	SAME AS ROW 2,1 COLUMN 2,2
2,-2	SAME AS ROW 2,2 COLUMN 1,-1	SAME AS ROW 2,2 COLUMN 1,0	SAME AS ROW 2,2 COLUMN 1,1	SAME AS ROW 2,2 COLUMN 2,-2	SAME AS ROW 2,2 COLUMN 2,-1	SAME AS ROW 2,2 COLUMN 2,0	SAME AS ROW 2,2 COLUMN 2,1	SAME AS ROW 2,2 COLUMN 2,2

AMPLITUDE MATRIX

FIGURE 41

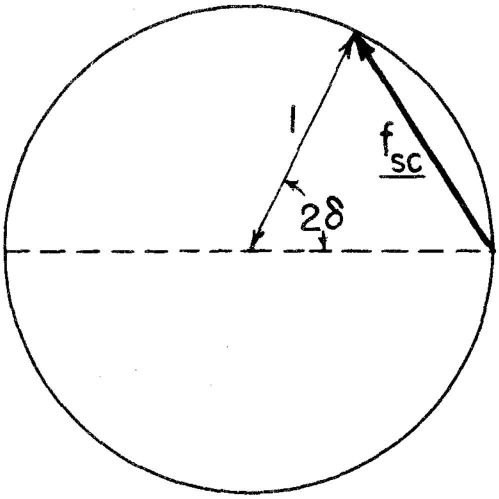

(a) PURE RESONANT SCATTERING WITHOUT REACTIONS

FIGURE 42A

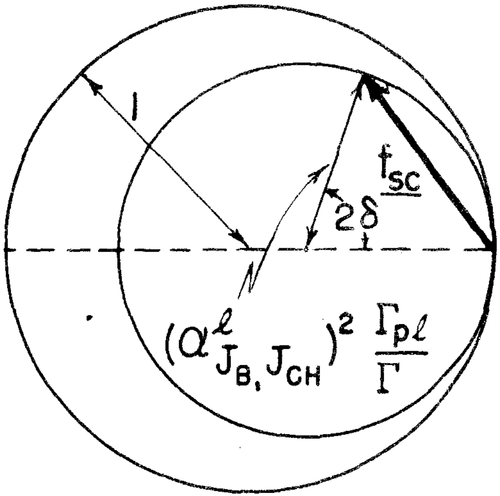

(b) PURE RESONANT SCATTERING WITH RESONANT REACTIONS

FIGURE 42B

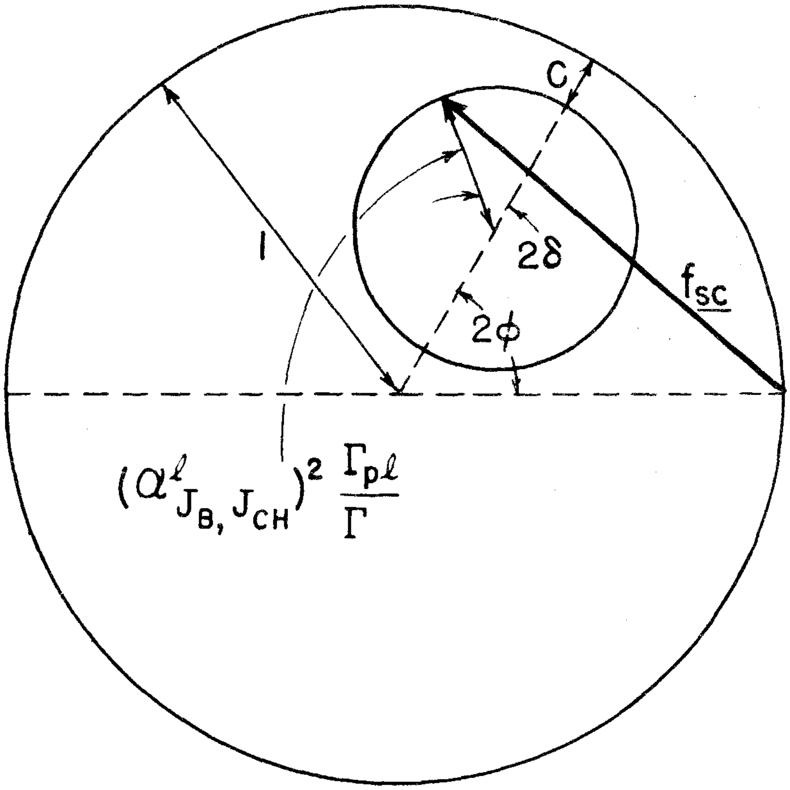

(c) PURE RESONANT SCATTERING WITH POTENTIAL SCATTERING AND RESONANT AND NON-RESONANT REACTIONS

FIGURE 42C

SCATTERING AMPLITUDE DIAGRAMS

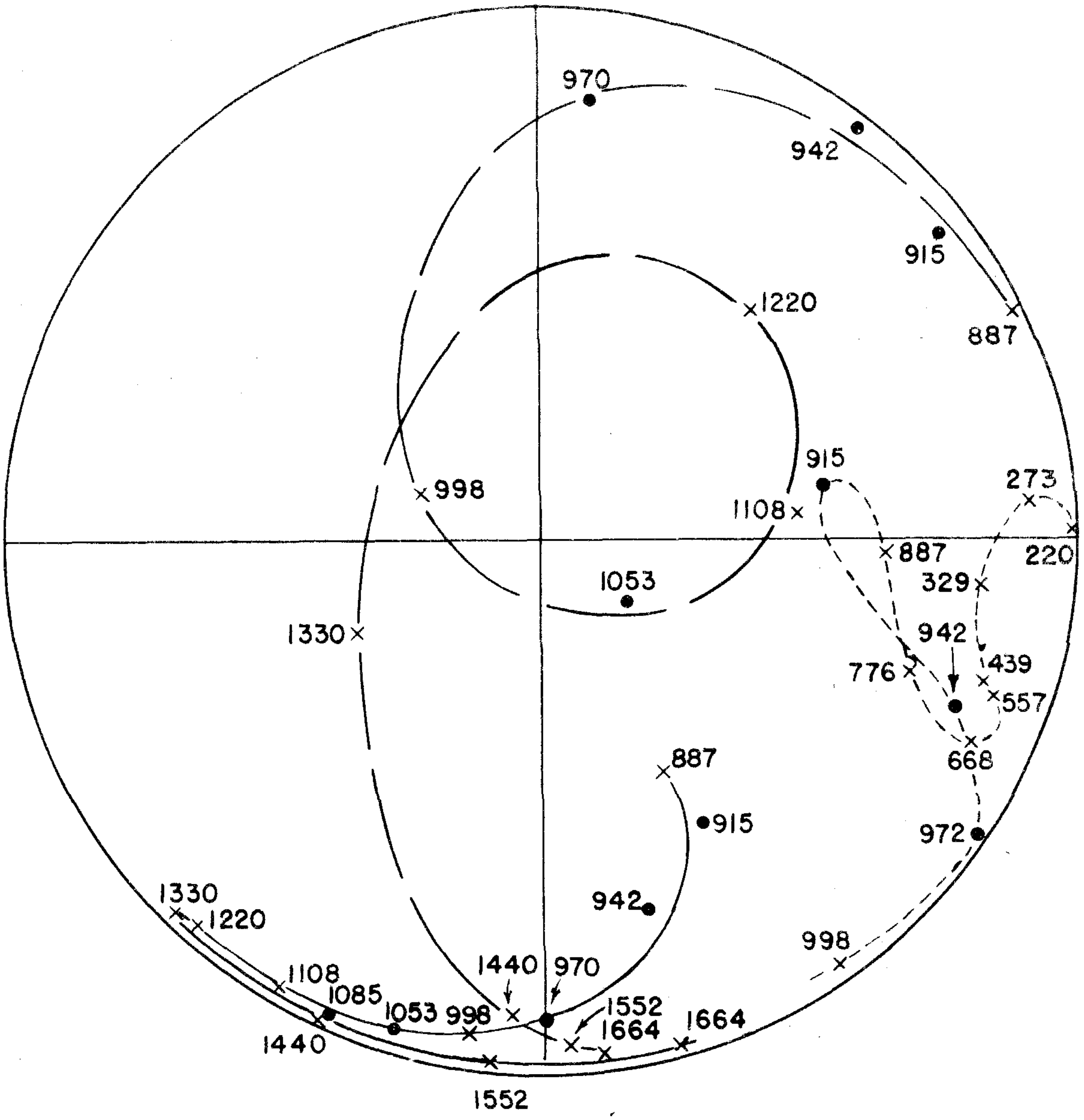

SCATTERING AMPLITUDE DIAGRAM OF S-WAVE PHASE SHIFTS OBTAINED FROM THEORETICAL FITTING OF EXPERIMENTAL DATA.

— — f_2 VS g_2 AS A FUNCTION OF ENERGY

—— f_1 VS g_1 AS A FUNCTION OF ENERGY

- - - - X VS Y AS A FUNCTION OF ENERGY

× PARAMETERS OBTAINED FROM ANGULAR DISTRIBUTIONS

● PARAMETERS OBTAINED FROM EXCITATION CURVES

FIGURE 43

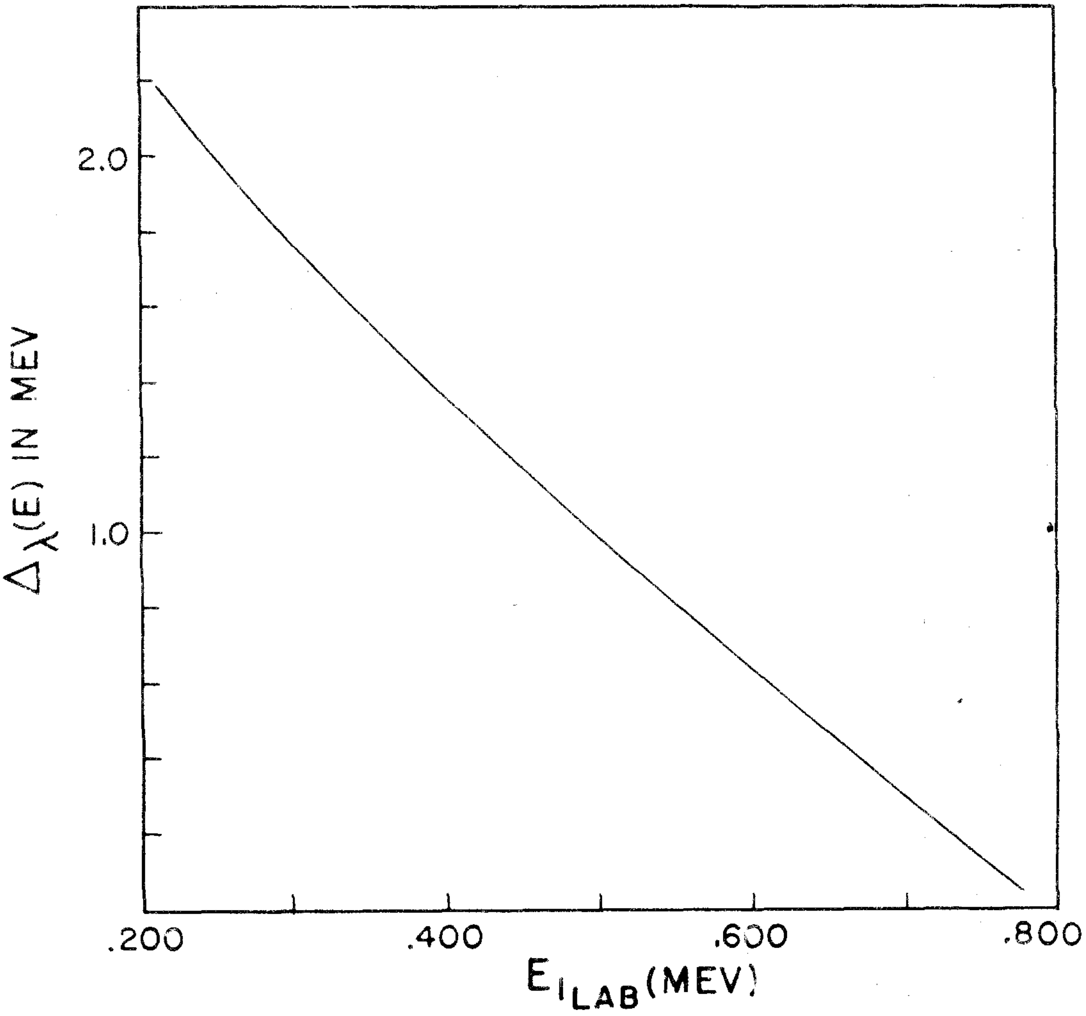

LEVEL SHIFT $\Delta_\lambda(E)$ AS A FUNCTION OF ENERGY FOR AN S-WAVE STATE WITH REDUCED WIDTHS $\theta_p^2/3 = .56$ $\theta_d^2/3 = .38$ $\theta_\alpha^2/3 = .04$

FIGURE 44

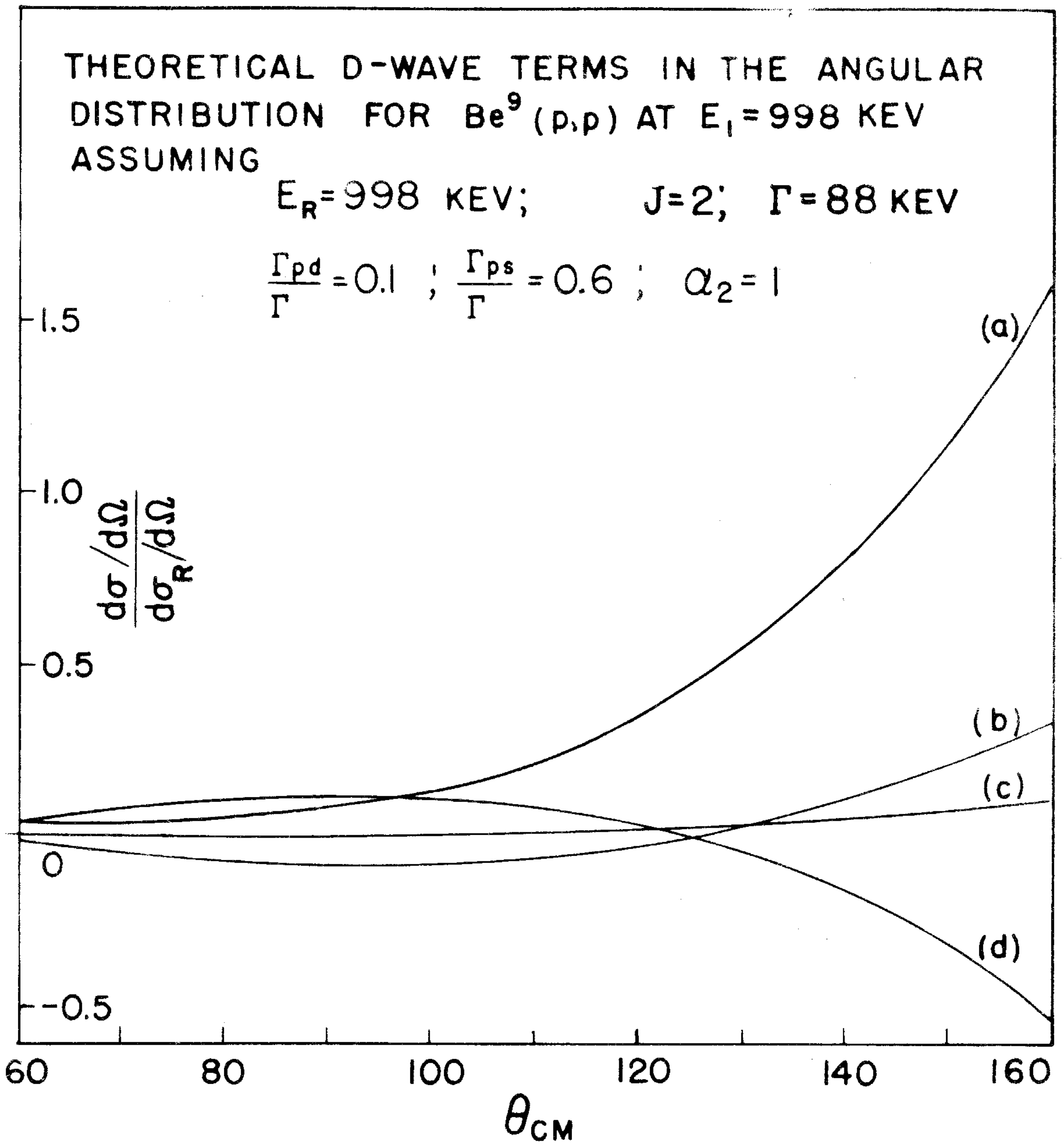

(a) D WAVE IN, S WAVE OUT, AND S WAVE IN, D WAVE OUT, INTERFERENCE AND NUCLEAR SQUARE TERMS.

(b) PURE D WAVE-COULOMB INTERFERENCE TERMS.

(c) PURE D WAVE NUCLEAR SQUARE TERM, AND PURE D WAVE-D WAVE IN, S WAVE OUT INTERFERENCE TERMS.

(d) PURE D WAVE — PURE S WAVE INTERFERENCE TERMS FOR $f_2 = 0$, $g_2 = 1$

FIGURE 45